Imaging and Suppressing Near-Receiver Scattered Seismic Waves

Proefschrift

ter verkrijging van de graad van doctor
aan de Technische Universiteit Delft,
op gezag van de Rector Magnificus prof. dr. ir. J.T. Fokkema,
voorzitter van het College voor Promoties,
in het openbaar te verdedigen op dinsdag 31 mei 2005 om 15.30 uur
door

Xander Hendrik CAMPMAN

mijnbouwkundig ingenieur
geboren te Eindhoven.

Dit proefschrift is goedgekeurd door de promotor:
Prof. dr. ir. A.J. Hermans

Toegevoegd promotor:
Dr. ir. G. C. Herman

Samenstelling Promotiecommissie:

Rector Magnificus, voorzitter	
Prof. dr. ir. A.J. Hermans	Technische Universiteit Delft, promotor,
Dr. ir. G.C. Herman	Shell International & Technische Universiteit Delft, toegevoegd promotor,
Prof. dr. ir. A. Gisolf	Technische Universiteit Delft,
Prof. dr. ir. A.W. Heemink	Technische Universiteit Delft,
Prof. dr. J. A. Scales	Colorado School of Mines,
Prof. dr. ir. C.P.A. Wapenaar	Technische Universiteit Delft,
Dr. E. Muyzert	Schlumberger Cambridge Research.

Dit onderzoek is financieel ondersteund door STW

ISBN 90-8559-053-1

Typesetting system: LaTeX 2_ε
Printed in The Netherlands by: Optima Grafische Communicatie

You have entered, following your own whim,
into the sphere of the inevitable—be at peace and be patient,
Venedikt Erofeev in *Moscow to the end of the line,*
(Trans.) Northwestern University Press, 1997.

Contents

1 Introduction **1**

1.1 Seismic Exploration 1

1.2 What about the Near Subsurface? 2

1.3 What to do about Near-Surface Effects? 3

1.3.1 Acquisition 3

1.3.2 Near-Surface Corrections Methods 4

1.3.3 Surface-Wave Suppression 6

1.4 A Closer Look at Near-Receiver Scattering 8

1.4.1 Additive vs Multiplicative Noise 8

1.4.2 Near-Receiver Scattering vs Short-Wavelength Statics 9

1.5 Our Method 11

1.6 Outline of This Thesis 13

2 Formulation of the Forward and Inverse Scattering Problem **15**

2.1 Propagation and Scattering in the Near-Surface Region 15

2.1.1 Elastodynamic Equations 16

2.1.2 Integral Representation for the Wave Field 17

2.1.3 An Approximate Integral Representation for Near-Receiver Scattering . 18

2.1.4 Green's Function 19

2.1.5 Parameterization 22

2.2 Formulation of the Inverse Scattering Problem 23

2.2.1 Preconditioning 24

2.2.2 Inversion 25

2.3 Suppressing Near-Receiver Scattered Waves 26

3 Application to Synthetic and Laboratory Data **29**

3.1 Test on Synthetic Data 30

3.1.1 Objective 30

3.1.2 Results 31

3.1.3 Waveform and Continuity 34

3.1.4 Sensitivity with Respect to the Velocity of the Embedding 37

3.1.5 Conclusion from Tests on Synthetic Data 39

3.2 Tests on Laboratory Data 40

3.2.1 Exciting and Measuring Surface Waves 40

3.2.2 Description of Experiment I 41

3.2.3 Results from Experiment I 45

3.2.4 Description of Experiment II 48

3.2.5 Results from Experiment II 48

4 Field-Data Examples **55**
4.1 Michigan Experiment — Schlumberger Data 56
4.1.1 Geometry 56
4.1.2 Near-Receiver Scattering 56
4.1.3 Wave-Field Separation 59
4.1.4 Imaging and Suppressing Near-Surface Scattering 60
4.1.5 Continuity and Coherency 65
4.1.6 Surface Consistency 67
4.2 Saudi Aramco Data 70
4.2.1 Geometry 70
4.2.2 Topography 70
4.2.3 Wave-Field Separation 73
4.2.4 Result 75

5 Conclusions and Discussion **77**

Bibliography **81**

A Fourier Transformations **87**
A.1 Temporal Fourier Transformation 87
A.2 Spatial Fourier Transformation 87
A.3 Convolution Theorem 88

B Derivation of Equation (2.7) **89**
B.1 Reciprocity 89
B.2 Green's State 89
B.3 Integral Representation 90

C Iterative Minimization **93**
C.1 Conjugate Gradient Method 93
C.2 Regularized Conjugate Gradients 94

D Computational aspects **97**
D.1 Operators 97
D.2 Green's Function in the Wavenumber-Frequency Domain. 98

E Filtering **101**
E.1 Wavenumber-Frequency Domain Filtering 101
E.2 Alpha-Trimmed Mean Filtering 102

Samenvatting **105**

Summary **107**

1

Introduction

The latest projected global oil demand from the International Energy Agency (2004a) shows that, in the short term, the global demand will increase by a few percents. In the long term (around 2030), however, oil demand will roughly have doubled compared to today, while gas is expected to play a much more important role than it does now (International Energy Agency, 2004b).

Oil companies make investments to develop and produce future energy supplies in order to meet this global demand for hydrocarbons. In this way, they guarantee a continuous supply by replacing the oil they produce with probable or proven reserves — reserves that can be produced within a few year's development.

On the other hand, they make these investments because the number of new proven reserves to balance depleted reserves is a measure of the potential of maintaining to be profitable in the long term. Consequently, continuity also directly influences the sentiment about the market value of a company (Wendlandt and Bream, 2003, e.g.).

It is therefore of vital importance for both oil consumers and oil companies that new reservoirs are found.

1.1 Seismic Exploration

Seismic methods are used for both exploration and detailed investigation of known reservoirs. In these methods seismic data are acquired and processed into a map –or image – of the first few kilometers of the Earth's subsurface, to identify potential oil or gas-bearing structures. A seismic experiment on land consists of setting off a source at the Earth's surface, sending down seismic energy to illuminate a target area in the subsurface. Reflected or scattered waves are then recorded with geophones, spread out along a line or grid on the Earth's surface.

One often assumes that sedimentation processes have produced a vertically layered Earth, i.e. a medium the properties of which change with increasing depth only. These changes in medium properties reflect the seismic waves back to the surface. Due to tectonic processes, however, the Earth's horizontal layering is complicated by folding and faulting. Due to various physical and geological processes, the younger top layers near the Earth's surface can be het-

erogeneous. This more complex structure causes the generation of many types of elastic waves other than purely up and down going body waves.

Some of these waves give valuable additional information about the subsurface structure, but others are considered unwanted as they obscure the body-wave reflections from the deeper subsurface. An example of such unwanted signal is the strong surface wave generated by the source. Because it is confined in the upper part the subsurface, it does not bear information of the deeper target area and is therefore considered as noise.

Once acquired, the data are processed to get a reliable image of the target area. The aim of processing is to increase signal-to-noise, to suppress unwanted signal and to increase the spatial and depth resolution (Yilmaz, 2001, for a complete overview of existing processing methods).

1.2 What about the Near Subsurface?

As more reservoirs are produced, it becomes increasingly difficult to replace them with new discoveries. To keep up with the demand for new discoveries, oil companies explore in progressively complex areas. In some cases, one of the consequences of shifting these operations to more complex areas, is the poorer quality of acquired data.

An important cause of poor data quality is the near-surface region (Levander, 1990; Cox, 1999, and the references therein). Notably seismically difficult areas are those with shallow carbonates (Taner, 1997; Regone, 1997), mountainous areas or areas with rugged topography (Regone, 1998), glacial tills (Berni and Roever, 1989) and, in general, deserts where dunes, karsts and wadis (Van der Veen and Herman, 2001) cause the wavefront of upcoming waves to be distorted.

Lateral velocity variations in the near subsurface and variations in layer thickness or topography cause variations in the arrival times and amplitudes of the upcoming wave front. When the dimensions of anomalies are comparable to the dominant wavelength, they can excite secondary (or scattered) waves. Moreover, spatially limited structures, like dunes, caves or underground channels, may cause resonances (Levander, 1990; Combee, 1994). In addition to a time shift in the upcoming reflection, scattering and resonances cause time-varying phase and amplitude distortions.

The presence of the surface and near-surface layers allows for the generation of guided wave types. For example, near-surface layers such as shallow carbonates, trap most of the source energy guiding it in horizontal directions, while only little energy is transmitted to the deeper subsurface. These strong surface waves attenuate less due to spreading compared to body waves. For this reason, they often dominate seismic records, masking reflections from the target area. The guided surface wave is usually called ground roll. Guided waves can be scattered by surface topography or near-surface anomalies producing strong secondary surface waves, which are difficult to remove with conventional filtering methods.

1.3 What to do about Near-Surface Effects?

The near subsurface can cause two main problems: variations in travel times and amplitudes of upcoming reflections, and a strong (scattered) surface wave obscuring upcoming reflections. We briefly review two strategies to attack these problems associated with near-surface layers. The first option is to suppress artifacts during the acquisition stage while the second one is to suppress them during the processing stage.

1.3.1 Acquisition

In conventional exploration seismic surveys, one uses geophone arrays rather than single geophones. An array consists of a number of geophones spread out along a line or in a small pattern. The distance between the geophones is the geophone spacing, while the distance between the centers of two adjacent arrays is referred to as the group interval. The output of such an array is one trace that is attributed to the center of an array (also called a station). The outputs of the geophones in an array are summed (stacked) and then transmitted to the recording truck where this summed trace is stored on tape.

Because upcoming reflection events are expected to arrive almost at the same time (with the same phase) at each receiver in an array, summing the response of receivers within an array is expected to enhance the signal by way of constructive interference of wave forms that align horizontally, while this operation attenuates random noise by a factor of the square root of the number of elements (Telford et al., 1990; Cooper, 2004, e.g.).

In general, each receiver has a slightly different response that can be attributed to its coupling in the ground, due to the fact that the top soil can vary at the surface (like dry sand, wet sand, loose sand). By summing the responses from several geophones, trace-to-trace amplitude variation due to ground coupling can be averaged.

Another way to reduce near-surface effects using arrays is that with a properly chosen geophone layout, horizontally traveling surface waves can be suppressed through destructive interference when the signals from the geophones in the array are stacked (Morse and Hildebrandt, 1988). This property is based on the fact that a regular pattern in the spatial domain, corresponds to a low-pass filter in the wavenumber domain.

When the near subsurface varies significantly on the scale of an array, however, perturbations affect the response of the wavenumber filter. The effect of perturbations on array forming have been investigated by Berni and Roever (1989); Blaquière and Ongkiehong (2000) and Panea et al. (2003), for example. The perturbations that occur on an intra-array scale can be statics, a move-out term or they can be due to misplacement of receivers within an array or due to ground coupling. Each can reduce the fidelity of the output trace of the array. Because the events are less continuous, these intra-array perturbations attenuate the high-frequency content of the output trace (Berni and Roever, 1989; Baeten et al., 2000; Muyzert and Vermeer, 2004). In many cases, the stacking operation acts as a high-cut filter (Marsden, 1993). This in turn,

reduces the maximum obtainable resolution.

For this reason, seismic exploration has witnessed a trend towards acquiring data with smaller geophone groups up-to the point where single receivers are recorded (Burger et al., 1998; Baeten et al., 2000; Moldoveanu et al., 2004, for example). It is a logical consequence of the increasing need for high-resolution data to focus on progressively smaller subsurface areas. Clearly, the advances in hardware, wiring and computer storage power have contributed to this trend.

The idea of single-receiver acquisition is to preserve as much signal as possible. However, the signal-to-noise ratio can be quite poor on individual traces. Neither is the coherent noise filtered by a stack array nor is the random noise reduced by destructive interference during the group forming process. The philosophy of these methods is that whatever noise was suppressed by stacking the array, can be done better after preprocessing as the dense sampling offers greater flexibility in processing (Baeten et al., 2001). After preprocessing, conventional groups can be formed, which are then expected to be more effective.

While there are those who strongly believe in the benefits of single-receiver recording, a critical note has been offered by Pecholcs et al. (2002) for example, claiming that there are no benefits to be expected from single-receiver recording when the data are very poor to begin with (see also Cooper, 2004).

1.3.2 Near-Surface Corrections Methods

Surface-Consistent Methods

At the processing stage, methods to correct for the time shifts caused by near-surface anomalies are often referred to as static corrections methods (short: statics). Sheriff (2002) defines statics as ‘corrections applied to seismic data to compensate for the effects of variations in elevation, weathering thickness, weathering velocity or reference to a datum. The objective is to determine the reflection arrival times which would have been observed if all measurements had been made on a (usually) flat plane with no weathering or low-velocity material present’.

Statics methods can be roughly divided into three categories: elevation corrections, refraction statics and residual statics. Elevation corrections are used to undo shot and geophone elevation differences. Then, usually, refraction statics are applied to account for varying layer velocities and thicknesses. Any static anomalies not resolved by the first two methods are collected under ‘residual statics’. Because these statics have an impact on velocity analysis, signal-to-noise and, ultimately, the quality of the image, application of residual statics corrections is often an important step in seismic processing.

The assumptions underlying (residual) static correction methods are discussed in Taner et al. (1974, for example), while popular methods for the computation of statics can be found in Wiggins et al. (1976) and Ronen and Claerbout (1985). A comprehensive overview on the entire subject can be found in Cox (1999).

Taner et al. (1974) expect that the overburden works like a filter, causing time and amplitude anomalies in the upcoming wavefront. But, they argue that estimating this filter is not practically feasible. In order to approximate the filter, they introduce some simplifying assumptions. First, they assume that the effect of the near subsurface is a pure time delay and that these delays are surface consistent, implying that each trace at a given surface location gets the same time delay. This is usually explained by assuming vertical ray paths through the overburden. In addition to the vertical ray paths in the overburden, Taner et al. (1974) assume that the near-surface effects do not vary with reflection time. Thus, the traditional statics model assigns the same uniform time shift to each trace from a distinct surface location. In this way, a single time shift corrects the entire trace. The statics shifts are computed relative with respect to some suitably chosen datum.

Most methods start by selecting one or a few time windows around clearly visible reflection events in the data. By first selecting the time windows and subsequently adding the shift to the whole trace, the time corrections are derived from a subset of the data and applied to the entire data set. In the time windows, time-shifts are picked between neighboring traces using cross correlations. These shifts are inserted into an equation that expresses the time shift as a composition of several time-delay effects. In general, this equation breaks the picked static shift down into a source static, a receiver static, an arbitrary shift for the CDP gather and a residual Normal Move Out (NMO) component. This is cast in a linear inverse problem which is under determined. Several solutions have been proposed for this problem. Most statics methods compute surface-consistent time shifts that align a Common-Depth Point (CDP) such that it produces an optimally stacked trace.

Based on the principle of surface consistency, one can also formulate schemes for amplitude corrections (Taner and Koehler, 1981). For the simultaneous estimation of amplitude and time anomalies, surface-consistent deconvolution methods have been developed (Cambois and Stoffa, 1993; Perkins and Calvert, 2001, e.g.). These last methods in fact closely resemble the 'filtering' behavior of the near surface. However, a single filter is estimated for each surface location which makes these methods also single-channel methods.

Redatuming Techniques

It is generally accepted that the near-surface problem is much more complex than described by the statics model described above (Taner and Koehler, 1981; Cox, 1999). In fact, surface-consistent static time shifts can be considered as an approximation to wave-equation datuming, where actual ray paths through the overburden are used.

In the past decade, wave-field-based datuming techniques have been developed to extrapolate the recorded wave field to a new 'datum' just under the overburden, thereby compensating for near-surface variations — or replacing the near-surface by a constant velocity layer (McMechan and Chen, 1990; Berryhill, 1984; Reshef, 1991). Because these methods use ray theoretical operators to redatum the data, they require an accurate velocity model of near subsurface. In complex near-surface regions, this is a serious drawback, because an accurate veloc-

ity model is difficult to obtain. For this reason, 'data-driven' redatuming techniques, like those based on Common Focus Point technology (Hindriks and Verschuur, 2001; Kelamis et al., 2002) may be preferable in areas with strong heterogeneity. However, in these areas, rapid changes in topography or layers may cause scattering and resonances. These are phenomena that are not modeled by ray theoretical methods like the redatuming techniques and, thus, the data have to be conditioned before application of such schemes.

Being based on ray theory, redatuming methods work best if the overburden varies smoothly which corresponds to long to intermediate-wavelength statics. This limits their use to near-surface regions where the wave field is not scattered by cavities, karsts, etc.

1.3.3 Surface-Wave Suppression

For land data, most of the source energy is converted into surface (Rayleigh) waves (Aki and Richards, 1980; Regone, 1998, e.g.). This causes a strong surface wave, usually called 'ground roll' in seismic exploration. Because one is usually interested in body-wave reflections from the deeper subsurface where the target area is, there has been considerable interest in developing methods to suppress (scattered) surface waves (Blonk and Herman, 1994; Regone, 1998; Herman and Perkins, 2004). In this section we review methods to suppress this type of noise.

As discussed before in Section 1.3.1, the surface wave can be suppressed in the field by using suitably chosen patterns of receivers (arrays). This method uses the difference in propagation direction of body waves (close to vertical) and surface waves (horizontal). The Rayleigh wave also differs from body waves in its polarization properties. If multicomponent data are available, it is sometimes possible to distinguish these differences in polarization and reject any arrival with elliptical polarization (Shieh and Herrmann, 1994).

A widely used technique to remove guided (surface) waves is filtering in the wavenumber-frequency ($k - f$) domain (also called dip filtering). This technique is based on the difference in apparent velocity of certain events. The apparent velocity is defined as the quotient of the distance traveled between two geophones and the difference in the arrival times of the event at the these geophones. Thus an upcoming reflection event has high apparent velocity because it arrives at two adjacent geophones nearly at the same time. On the other hand, the (apparent) velocity of ground roll is typically very low. However, they can overlap in the spatial-time ($x - t$) domain because, just like reflection events, surface waves arrive at late times. To use this difference in apparent velocities, one transforms the data with a double Fourier Transformation to the $k - f$ domain, because a double Fourier transformation maps a plane wave (i.e. a wave that is characterized by one apparent velocity) in the $x - t$ domain to a line in the $k - f$ domain with the same slope that corresponds to this velocity (Yilmaz, 2001). In this way, the waves with slower apparent velocities are located along lines with different slopes than events with higher apparent velocities and are thus separated. By defining a suitable pass zone for the events in the $k - f$ domain, all events with apparent velocities outside this pass zone are rejected and one subsequently transforms the data back to the spatial-time domain.

This technique works well if the surface wave is sufficiently sampled in the spatial coordinates to prevent aliasing and if the apparent velocity of the surface waves is the same as the actual velocity (because then it is sufficiently different from the apparent velocities of upcoming reflections). This last condition is only the case when the surface wave travels along the receiver line.

Scattered ground roll presents a complication to most of the ground roll suppression schemes, especially when it has been scattered out of plane. Ground roll that has been scattered away from the line of receivers, has a part with hyperbolic move-out (the apex) and therefore higher apparent velocities which may overlap the body-wave reflections in the $k - f$ domain. Moreover, scattered surface waves can produce such complicated interference that it renders polarization filters useless.

Regone (1997, 1998), discusses the problem of identifying and suppressing coherent noise in seismic data. He focuses mainly on the scattered coherent noise in 3-D acquisition geometries. In these geometries, the wave field is generally not sufficiently sampled at the surface to process the data with conventional methods in such a way that the signal-to-noise ratio (reflections-to-coherent noise-ratio) is acceptable for a reliable subsurface image. Regone (1998) proposes an identification tool to better understand the 3-D properties of the noise wave field. In this way, acquisition design can be optimized so that further processing can attenuate this noise better. This technique shows the strong link between acquisition and successful processing (see also Cooper, 2004, for example).

Another approach has been developed during the last decade at Delft University (Blonk and Herman, 1994; Ernst et al., 1998). Both methods are based on a common philosophy: with knowledge of the near-surface scattering distribution, one can calculate the scattered waves and subsequently subtract them. Thus, an important step in these methods is to find the scattering distribution that causes the near-surface scattered waves.

For the case of surface wave-to-surface wave scattering in the near subsurface (side-scattered waves or additive noise), Blonk (1994) derives an efficient model using scattering of Rayleigh waves in a homogeneous elastic embedding, in which scatterers are distributed near the surface. Ernst (1999) considers the same problem, but in a laterally varying medium. Allowing the background medium to vary introduces more complexity in the model and to keep his theory tractable for large-scale problems, Ernst (1999) approximates the main contribution with a scalar approach.

To model the scattered surface waves, Blonk (1994) first estimates a distribution of near-surface scatterers. This is an inverse problem that he solves by finding a near-surface scattering distribution that minimizes a cost function that consists of the squared difference between the observed near-surface scattered field and the scattered field modeled with his noise model. To condition the data before the inversion, Blonk (1994) first suppresses the direct Rayleigh wave, so that the remaining data consist mainly of scattered surface waves. The remaining data are then fed to the inversion scheme.

The success of this method is based on its ability to discriminate near-surface scattered

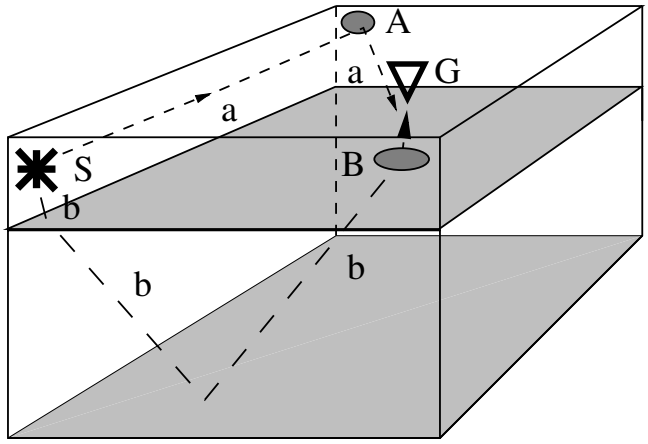

Figure 1.1: *Illustration of two types of near-surface scattering mechanisms: A is a heterogeneity far from the source, S, and receiver G; shot-generated surface waves travel along path a and are scattered at A. This is a form of side-scattered or additive noise. B is a heterogeneity directly beneath the receiver. Body waves travel along path b and are reflected by deeper layers. Each reflection that is recorded by G passes through B and excites (scattered) surface waves.*

waves from body-wave reflections as they are also contained in the input for the inversion algorithm. In order to effectively separate these waves, Blonk (1994); Ernst (1999) estimate a scattering distribution that is consistent with several shot records. In a way, this may be considered the equivalence of the surface-consistency concept used in static corrections methods, where one uses redundancy of the data to obtain more accurate corrections. The method of Blonk and Herman (1994) has been modified for the case of data on a dense grid of shots and receivers by Herman and Perkins (2004).

1.4 A Closer Look at Near-Receiver Scattering

1.4.1 Additive vs Multiplicative Noise

In the previous section, we reviewed some methods to identify and suppress scattered surface waves. These waves are excited by the shot-generated surface wave (or ground roll). Scattered ground roll is sometimes refferd to as side-scattered noise. Because this scattering process takes place in the first tens of meters of the subsurface only, it is independent of body waves that travel into the medium and are reflected back to the surface. Therefore it can be considered as an additive term and we can refer to this type of noise as additive noise. Reduction of additive

scattered noise on seismic data is discussed by Blonk (1994) and Ernst (1999), for example (see Section 1.3.3).

On the other hand, surface waves can also be excited by body-wave reflections impinging on heterogeneities directly beneath the receivers. In this case, body waves are converted into (scattered) surface waves because these heterogeneities act as secondary sources. Although the body wave is also converted to scattered $P-$ and S waves, we restrict our discussion to the scattered Rayleigh wave as this surface wave usually represents the bulk of the scattered wave field. Because the strength of these scattered waves is proportional to the strength of the incident reflection (Bannister et al., 1990, for example), this type of scattered energy can be considered as multiplicative noise. Reduction of this type of multiplicative noise is the main topic of this thesis.

To see the difference, consider the situation sketched in Figure 1.1, where the source S excites both body and surface waves. The shot-generated surface wave travels along path a and scatters far from the source and receivers and is recorded at the geophone G. In this case, the interaction takes place between surface waves only. The body wave however, first travels down, where it is eventually reflected partly into upcoming body waves. These upcoming waves travel through the overburden and can be scattered by heterogeneities close to the receivers where they excite surface waves. In this way, all upcoming body-wave reflections are partly converted into surface waves.

1.4.2 Near-Receiver Scattering vs Short-Wavelength Statics

To understand near-receiver scattering, we analyzed data from a relatively simple synthetic near-surface scattering experiment. Combee (1994) isolated the problem of an upcoming plane scalar wave incident on a near-surface anomaly and presented analytical solutions. He concluded that for sizes of the anomaly in the order of a wavelength, multiple scattering caused the wavelet to change in a way that cannot be corrected for by static correction methods.

Here, we present a similar study, using a 2-D elastic finite-difference method to model the response of the wave field excited by a plane-wave source at the bottom of a two-layered model. This type of model takes conversion of body waves into surface waves and guided waves into account.

The model is shown in Figure 1.2(a). The top layer has a P-wave velocity given by $c_P = 1200$ m/s and a S-wave velocity given by $c_S = 400$ m/s. In the middle of the model the depth of the top layer (10 m) changes to 20 m and back. The P-wave velocity in the base layer is $c_P = 2500$ m/s while the S-wave velocity in the base layer is $c_S = 600$ m/s. The vertical component of the particle velocity, calculated at the surface, is shown as a function of time and position in Figure 1.2b. In this Figure, we have simulated field arrays by averaging over five traces (10 m) of the original record for each trace in this record. In Figure 1.2c the original record of single receivers with a spacing of 2 m is shown.

Figure 1.2c contains a shift, consistent with a static shift calculated along vertical ray paths,

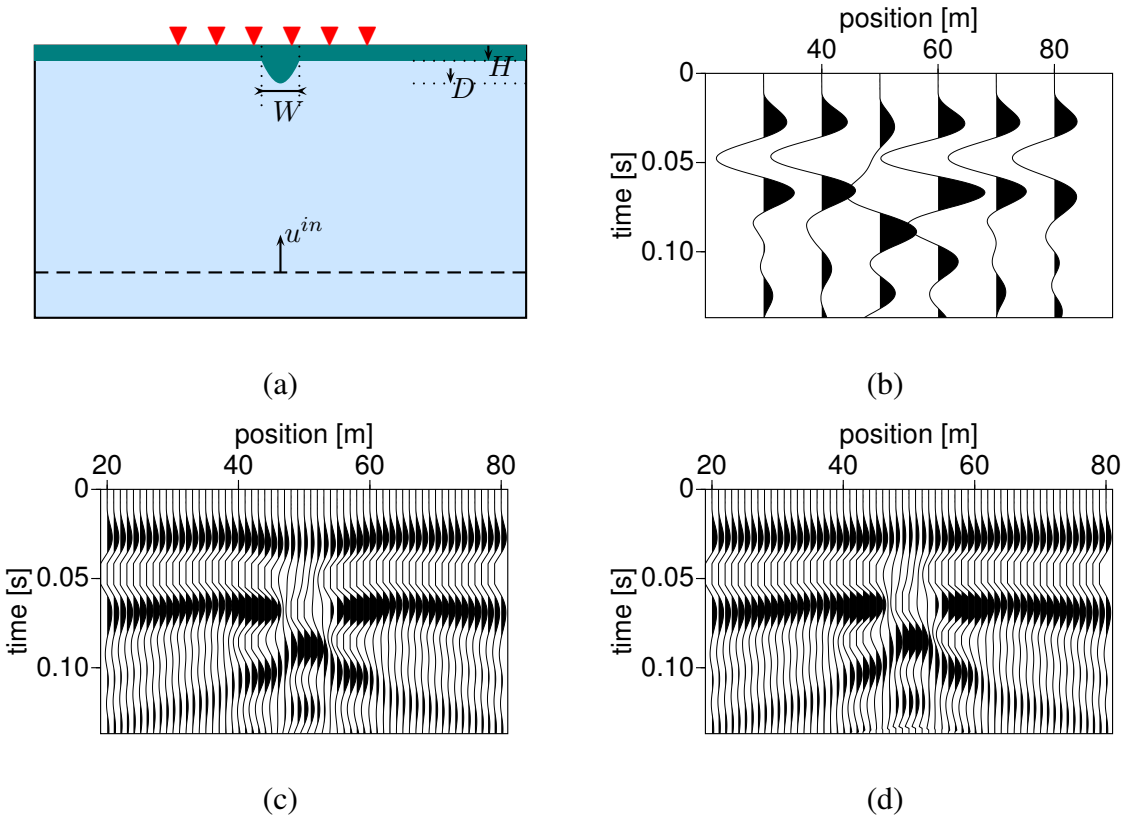

Figure 1.2: *(a) Model with a layer and anomaly. The velocities of the top layer and the anomaly are the same : $c_P = 1200$ m/s and $c_S = 400$ m/s. The velocities of the second layer are $c_P = 2500$ m/s and $c_S = 600$ m/s, respectively. To simulate an upcoming reflection, a plane-wave source, with dominant frequency of about 20 Hz, is located at 25 m depth. The dimensions in terms of the dominant wavelength λ are $W \approx \lambda$,$D < \lambda$ and $H << \lambda$. (b) Response of the plane wave,u^{in}, passing through the low-velocity layer with anomaly. Vertical velocity at the surface, computed with 2-D elastic FD code and averaged over five traces to simulate array forming. (c) Same as in (b), but without averaging. The time shift is consistent with the time shift predicted by the statics model. (d) Same as in (c), but aligned at first breaks.*

at about 25 ms and interference around 70 ms, due to multiple scattering. At later times, one can identify guided waves traveling outward from the anomaly. In Figure 1.2d we have aligned the first arrival times of the traces (first breaks). It is clear that this (simple) static correction does not restore the continuity of the event and stacking these corrected traces will produce nearly the same array-formed stack as the one shown in Figure 1.2b. In the array-formed data, the anomaly appears in the form of a 'static' with additional amplitude and phase distortions,

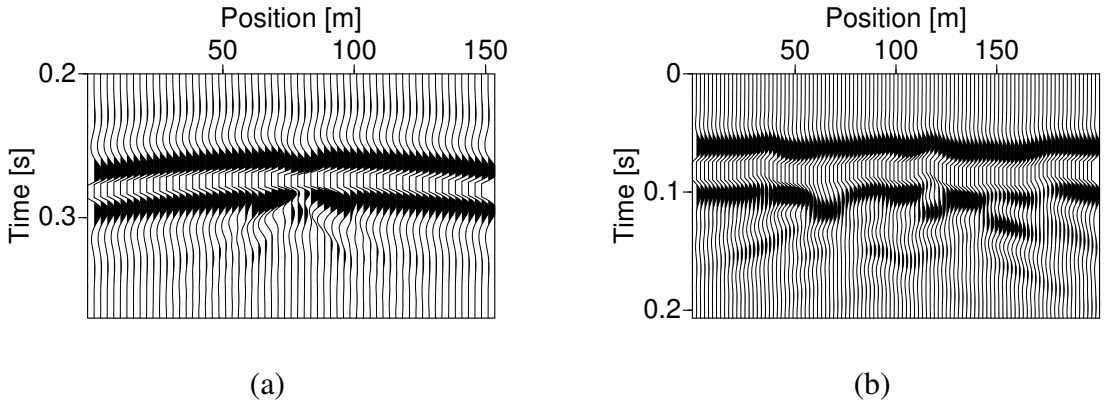

Figure 1.3: *(a) An upcoming wavefront impinges on a near-receiver scatterer. This causes a time-shift and amplitude anomalies in the wave front. The upcoming body wave is also partly converted to a surface wave. This surface wave interferes with the body wave. (b) An upcoming body wave impinges on many near-receiver scatterers. In this case, the secondary surface waves interfere with one another and cause a complicated coda following the upcoming wave. In this case, individual scatterers cannot be identified anymore and the variations may be erroneously interpreted as short-wavelength statics.*

while in the original, single-receiver data, the anomaly is characterized by scattering, including a different time shift for each receiver and interference. This is especially clear in densely sampled data, in which case the diffraction from near-surface heterogeneity can be tracked at least along a few traces in the data, which makes them appear coherent (Telford et al., 1990).

As the near-surface becomes more complex, scattering from different heterogeneities interferes and the noise can appear as rapid (trace-to-trace) variations in the arrival times and amplitudes of reflections. For many, randomly distributed scatterers, this is shown in Figure 1.3b, while Figure 1.3a shows again scattering from one near-surface anomaly. In the context of statics, these variations may be erroneously attributed to (very) short-wavelength (intra-array) statics (Cox, 1999, p. 277).

1.5 Our Method

In Section 1.2 we identified two main problems associated with the near surface: time and amplitude anomalies and interfering (scattered) surface waves. In fact, near-receiver scattering can be considered as a combination of these two problems. Because near-receiver scattering and its related phenomena like interference are deterministic, multichannel, processes, one can infer that the proper way to correct for the anomaly is a multichannel approach, *before* array-forming. Discussing intra-array processing, Baeten et al. (2001) raise a similar point. While they show that statistically based intra-array static corrections can be effective, they argue that

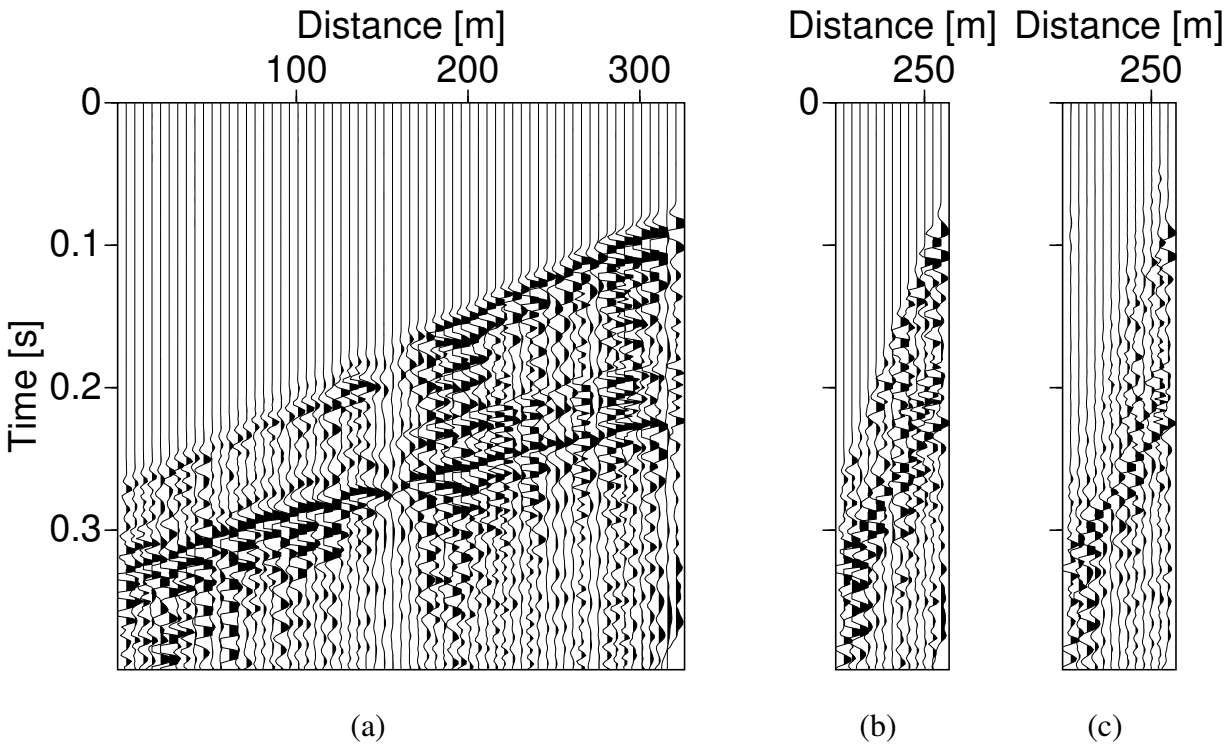

Figure 1.4: *(a) Part of a single-receiver field record with dense spatial sampling. One can identify near-receiver scattering, showing as the diffractions and interference between 125 and 175 m and around 40 m. (b) Same record, but after group forming by summing five neighboring traces. (c) Same as (b), but after suppressing scattered noise with our method. Note that the signal-to-noise ratio of the shallow reflection (the second event) has increased significantly and the amplitudes are better balanced. This example illustrates the potential benefit of our method for densely sampled data.*

perturbations incurred by diffractions and reverberations 'can only be addressed properly by wave-field-based inversion methods'.

In this thesis, we present such a deterministic method to suppress near-receiver scattered noise based on a wave-theoretical model for body wave-to-surface-wave scattering. The underlying idea of our method is the same as in the method developed by Blonk (1994): with knowledge of the near-surface scattering distribution and the propagation characteristics of the near-surface region, we can predict and subsequently subtract the scattered noise. To this end we first formulate a model that describes near-receiver scattering. However, before we can predict the scattered wave field, we need an estimate of the distribution of scatterers that excites this (secondary) wave field. This is an inverse problem, which we solve by iteratively updating a near-surface scattering function that 'best' fits the data using our scattered noise model.

To derive the near-surface scattering function from the data, we use short time windows to

obtain an independent estimate of the scattering distribution. This is similar to the approach taken in residual statics estimation. Our approach differs from statics, because in our formulation, surface-consistent, single-channel, time shifts or filters are replaced by a surface-consistent, multichannel filter. We then use the estimated scattering distribution to forward model the scattered wave field and finally we subtract the scattered wave field.

As an example of the effect of our method on the group forming process, we show part of a shot record from a survey in an area with a significant amount of near-receiver scattering in Figure 1.4a. Figure 1.4b shows the same record, but after conventional group forming by stacking five adjacent traces. After application of our method, the group formed record is depicted in Figure 1.4c. In this figure, the signal-to-noise ratio has been improved and the second reflection event is more pronounced and can therefore be identified with more certainty.

1.6 Outline of This Thesis

In Chapter 2, we start with analyzing propagation and scattering of elastic waves in the near subsurface. Based on physical arguments, we arrive at an approximate integral representation for the near-receiver scattered field. With this representation we can predict the scattered field when the scattering distribution is known. In the second part of this chapter, we discuss a procedure to estimate this near-surface scattering distribution from the seismic data itself. At the end of this chapter we summarize the results, yielding our method to predict and subtract near-receiver scattered waves from seismic data.

In Chapter 3, we investigate the validity and limitations of the main assumptions made to arrive at our scattered noise model. These tests are carried out by applying the algorithm to data obtained from suitably chosen models. In the same chapter, we apply our algorithm to data from two laboratory tests of scattered surface waves. This is an intermediate step before applying the algorithm to field data in Chapter 4.

The application to field data shows the potential of our method and the robustness in the case that the data are contaminated by noise.

In Chapter 5 we conclude with a discussion of the results obtained in this thesis and with recommendations for future work.

2

Formulation of the Forward and Inverse Scattering Problem

We present the basis of our method to predict and suppress near-receiver scattered waves from seismic data. We start by describing propagation and scattering in the near-surface region of an elastic medium. The elastic wave field in the medium is expressed in terms of an integral representation, which consists of one part that accounts for propagation in the embedding medium and one part that is due to perturbations in the elastic parameters.

In Section 2.1, we derive an approximate equation for near-receiver scattering, using mainly physical arguments. We arrive at a scalar representation for the scattered field, describing the dominant scattering effects. This is followed by a prelude to the formulation of the inverse problem. We parameterize our approximate scattering equation in terms of a surface scattering distribution, which represents the impedance experienced by upcoming waves when they travel through the shallow subsurface.

The deterministic approach taken in this thesis hinges on knowledge of the distribution of near-surface heterogeneities that cause scattering. To determine this distribution we need to solve an inverse problem. We describe a sequence of steps that allows us to obtain an independent estimate of the near-surface impedance function from one event, so that we can predict the scattered field on an entire record. This is followed by a description of the inversion algorithm, where we minimize a cost functional consisting of the squared difference of the actual field and the predicted field by iteratively updating the impedance function.

In the final section, we collect the results from this chapter and present a method for suppressing near-receiver scattered waves.

2.1 Propagation and Scattering in the Near-Surface Region

We consider scattering of waves by heterogeneities embedded in an elastic half space occupying the domain $\mathcal{D}$. The heterogeneities occupy the scattering domain $\mathcal{B}$. The boundary of the half space, $\partial\mathcal{D}$, consists of the free surface, Σ, and the lower hemi-sphere, Ω. The configuration is

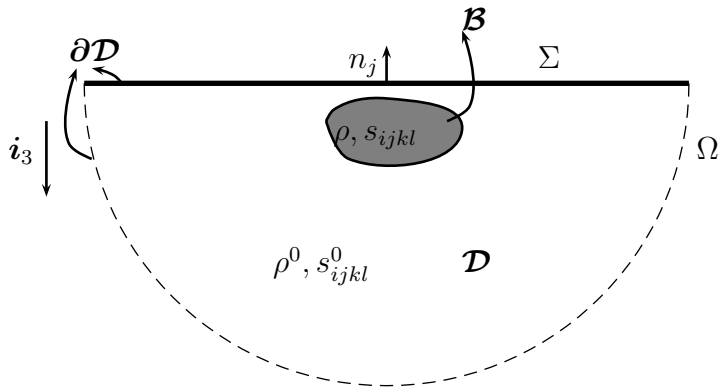

Figure 2.1: *Configuration: a near-surface scatterer with properties ρ and s_{ijkl}, occupies the domain $\mathcal{B}$. It is embedded in an elastic half space ($\mathcal{D}$) where $\rho = \rho^0$ and $s_{ijkl} = s^0_{ijkl}$.*

depicted in Figure 2.1. To denote position, we use coordinates x, y, z with respect to the origin $\mathcal{O}$ of a Cartesian reference frame with unit vectors $\mathbf{i}_1, \mathbf{i}_2, \mathbf{i}_3$ along three mutually perpendicular axes, in this order forming a right-handed system. We use the subscript notation for vectors and tensors. Latin subscripts range from 1 to 3 while Greek subscripts range from 1 to 2. For repeated lower subscripts the summation convention is understood, i.e., $u_i v_i = u_1 v_1 + u_2 v_2 + u_3 v_3$, for example. For position vectors we also use the boldface notation $\mathbf{x} = x\mathbf{i}_1 + y\mathbf{i}_2 + z\mathbf{i}_3$ and $\mathbf{x}_L = x\mathbf{i}_1 + y\mathbf{i}_2$. Partial derivatives with respect to the spatial coordinates are denoted by Latin or Greek subscripts, for example ∂_i or ∂_α. Derivation with respect to time is denoted by ∂_t, 't' being reserved for 'time' (no summation).

2.1.1 Elastodynamic Equations

For small deformations, the local behavior of disturbances in an elastic medium is governed by the linearized equation of motion (Newton's law) and the equation of deformation:

$$\Delta_{ijpq}\partial_j \tau_{pq}(\mathbf{x},t) - \rho(\mathbf{x})\partial_t^2 u_i(\mathbf{x},t) = -f_i(\mathbf{x},t), \tag{2.1}$$

$$\Delta_{ijpq}\partial_p u_q(\mathbf{x},t) - s_{ijpq}(\mathbf{x})\tau_{pq}(\mathbf{x},t) = 0. \tag{2.2}$$

Here, $u_i(\mathbf{x},t)$ [m] denotes the displacement of the solid and $\tau_{pq}(\mathbf{x},t)$ [Pa] the stress in the solid at position $\mathbf{x}$ [m] and at time t [s]; $f_i(\mathbf{x},t)$ [N/m^3] denotes a source term of body forces. The density of the medium at position $\mathbf{x}$ is $\rho(\mathbf{x})$ [kg/m^3], while the compliance is denoted by the rank four tensor $s_{ijkl}(\mathbf{x})$ [Pa^{-1}]. The symmetrical tensor of rank four is defined in De Hoop (1995, Equation (A.7-43)):

$$\Delta_{ijpq} = \frac{1}{2}\left(\delta_{ip}\delta_{jq} + \delta_{iq}\delta_{jp}\right), \tag{2.3}$$

where δ_{ik} is the Kronecker delta ($\delta_{ij} = 1$ for $i = j$ and $\delta_{ij} = 0$ for $i \neq j$). In this thesis, we only consider causal solutions of these equations. In the following, we mainly use the frequency-domain counterparts of Eqs (2.1) and (2.2). Using the Fourier Transformation defined in Appendix A, Equation (A.1), we obtain:

$$\Delta_{ijpq}\partial_j \tau_{pq}(\mathbf{x},\omega) + \rho(\mathbf{x})\omega^2 u_i(\mathbf{x},\omega) = -f_i(\mathbf{x},\omega), \tag{2.4}$$

$$\Delta_{ijpq}\partial_p u_q(\mathbf{x},\omega) - s_{ijpq}(\mathbf{x})\tau_{pq}(\mathbf{x},\omega) = 0, \tag{2.5}$$

where ω [rad/s] denotes the angular frequency, and we have used $\partial_t \rightarrow \mathrm{i}\omega$. From now on, when we work with frequency-domain quantities, we will omit the ω-dependence. When working with time-domain quantities, we will explicitly indicate this. The above equations are complemented with the boundary condition of vanishing traction at the free surface Σ (e.g. Aki and Richards, 1980, pp. 135):

$$n_j \tau_{ij}(\mathbf{x}) = 0, \qquad \mathbf{x} \in \Sigma. \tag{2.6}$$

Here, n_j is the (outward pointing) normal to the surface Σ (see Figure 2.1). As there are no sources at infinity, the wave field consists of waves propagating away from the sources at large distances from the sources.

2.1.2 Integral Representation for the Wave Field

Consider again the configuration depicted in Figure 2.1. Using the Betti-Rayleigh reciprocity theorem (e.g. De Hoop, 1995, pp. 445-448, see also Appendix B), we express the wave field in this configuration as a superposition of a part that accounts for propagation in the embedding medium $\mathcal{D}$, u_i^0, and a secondary wave field, u_i^1, accounting for the presence of local perturbations (occupying the domain $\mathcal{B}$) in the medium (Eq. (B.12)):

$$u_i = u_i^0 + u_i^1. \tag{2.7}$$

In Appendix B, we derive the following integral representation for the displacement in the embedding, u_i^0:

$$u_i^0(\mathbf{x}) = \int_{\mathcal{D}} u_{ij}^G(\mathbf{x},\mathbf{x}') f_j(\mathbf{x}')\mathrm{d}V, \tag{2.8}$$

and for the displacement due to heterogeneities, u_i^1:

$$u_i^1(\mathbf{x}) = \omega^2 \int_{\mathcal{B}} u_{ij}^G(\mathbf{x},\mathbf{x}')(\rho-\rho^0)(\mathbf{x}')u_j(\mathbf{x}')\mathrm{d}V + \int_{\mathcal{B}} \partial_j' u_{ik}^G(\mathbf{x},\mathbf{x}') c_{kjns}^0 (s_{nspq} - s_{nspq}^0)(\mathbf{x}')\tau_{pq}(\mathbf{x}')\mathrm{d}V, \tag{2.9}$$

where c_{ijkl}^0 [Pa] is the stiffness tensor. In Equations (2.8) and (2.9), $u_{ij}^G(\mathbf{x},\mathbf{x}')$ is the Green's function, denoting the i-th component of the wave field at $\mathbf{x}$ due to a point source directed in the j-th direction at $\mathbf{x}'$.

2.1.3 An Approximate Integral Representation for Near-Receiver Scattering

Having presented the integral representation for scattering of elastic waves by contrasts in density and compliance, we now direct our attention to the specific problem of inversion and modeling scattering by heterogeneities close to the receivers. For now, we assume that the scattering takes place at a distance smaller than a Rayleigh wavelength from the surface. In the next chapter, where we test the sensitivity of our method with respect to the depth of the scattering, we will show that this assumption can be relaxed.

In Section 1.3.3 we reviewed the work of Blonk (1994), on imaging and predicting scattered surface waves. To estimate a scattering distribution that predicts scattered surface waves, he minimizes the difference between the observed scattered field and the scattered field calculated with his model of near-surface scattering. This near-surface scattering model only takes into account density perturbations.

In his thesis, Blonk (1994, pp. 55-56) investigated the sensitivity of his method with respect to neglecting the Lamé parameters (for an isotropic solid, the only independent parameters in the compliance tensor are the Lamé parameters) in the inversion scheme for the vertical component of the velocity. It turned out that perturbations in both density and Lamé parameters can be accounted for with a fair degree of accuracy by using only a density perturbation. Note that the distribution of scatterers estimated in this way does not necessarily correspond to the actual scattering distribution in the near subsurface. For his purpose, however, this was not a problem, as long as this estimate could accurately predict scattering.

In our proposed method, we are also primarily interested in accurately estimating scattered waves and we may use the same ansatz. Consequently, we drop the second term on the right-hand side (RHS) of Equation (2.9) containing the compliance contrast. In this way, we obtain

$$u_i^1(\mathbf{x}) = \omega^2 \int_{\mathcal{D}} u_{ij}^G(\mathbf{x}, \mathbf{x}') \Delta\rho(\mathbf{x}') u_j(\mathbf{x}') \mathrm{d}V, \tag{2.10}$$

where $\Delta\rho = \rho - \rho^0$ is the density perturbation.

In the majority of land surveys in seismic exploration, vertical velocity is measured. For practical reasons, we therefore want to express our integral representation in terms of vertical velocity. To do so, we first differentiate particle displacement with respect to time. In the frequency domain, this operation corresponds to a multiplication by $\mathrm{i}\omega$ (see Appendix A). We then obtain:

$$v_i^1(\mathbf{x}) = \omega^2 \int_{\mathcal{D}} u_{ij}^G(\mathbf{x}, \mathbf{x}') \Delta\rho(\mathbf{x}') v_j(\mathbf{x}') \mathrm{d}V. \tag{2.11}$$

This equation expresses that the j-th component of the field at $\mathbf{x}'$ interacts with the scatterer and excites scattered waves in the i-direction. If we consider now the measurement of the vertical component at $\mathbf{x}$, we select $i = 3$, yielding:

$$v_3^1(\mathbf{x}) = \omega^2 \int_{\mathcal{D}} u_{3j}^G(\mathbf{x}, \mathbf{x}') \Delta\rho(\mathbf{x}') v_j(\mathbf{x}') \mathrm{d}V. \tag{2.12}$$

Although we have reduced the problem to an integral representation for one component, three terms play a role in the RHS of Eq. (2.12) (the summation convention applies to subscript j).

For (nearly) plane upcoming P waves with moderate angles of incidence (which we expect to get from reflections from the deeper subsurface), we may assume that the vertical components are larger than the horizontal ones for events arriving at the scatterer[1]. By doing so, we can further reduce the complexity of Equation (2.12). Neglecting the horizontal components at the scatterer, we obtain

$$v_3^1(\mathbf{x}) = \omega^2 \int_{\mathcal{D}} u_{33}^G(\mathbf{x}, \mathbf{x}') \Delta\rho(\mathbf{x}') v_3(\mathbf{x}') \mathrm{d}V. \tag{2.13}$$

On the RHS, we only have one term left. This term contains an exciting field in the $\mathbf{i}_3$-direction and an isotropic scatterer. Therefore, we can think of the factor $\Delta\rho v_3$ as a vertical excitation.

For the wave field excited by a vertical force, Los et al. (2001) show that the vertical component of the field observed within a wavelength of the source may be fairly accurately approximated by a scalar equation. This is considered in the next section.

2.1.4 Green's Function

We construct a scalar Green's function for Equation (2.13) of the form used in Los et al. (2001). Note that we are looking for the vertical *displacement* due to a vertical force. For simplicity, we assume that the medium is isotropic. For such a medium, the stiffness tensor is symmetric and only depends on the Lamé parameters, λ and μ:

$$c_{ijkl}^0 = \lambda^0 \delta_{ij}\delta_{kl} + \mu^0(\delta_{ik}\delta_{jl} + \delta_{il}\delta_{jk}). \tag{2.14}$$

Using $c_{ijkl}^0 = c_{ijlk}^0$ and $\tau_{ij} = \tau_{ji}$ we can write Equation (2.5) as

$$\tau_{ij} = c_{ijkl}^0 \partial_k u_l. \tag{2.15}$$

Substituting Equation (2.14) into Equation (2.15) and then substituting in turn Equation (2.15) into (2.4), we eliminate the stress, arriving at the elastic wave equation for particle displacement (cf De Hoop, 1995, Equation (10.12-13), for example):

$$(\lambda^0 + \mu^0)\partial_i\partial_k u_k + \mu^0 \partial_k \partial_k u_i + \rho^0 \omega^2 u_i = -f_i. \tag{2.16}$$

Here, we assume that the Lamé parameters λ^0 and μ^0 and the density ρ^0 in the embedding close to the surface are constant.

[1] In receiver function studies in global seismology, it is common to assume that the longitudinal (i.e. the vertical) component of the particle velocity consists of near-vertically incident teleseismic $P-$waves only (Langston, 1979, for example).

The Green's function u_{ij}^G is defined as the i-th component of the displacement at $\mathbf{x}$ due to a point source pointing in the j-direction at $\mathbf{x}'$:

$$(\lambda^0 + \mu^0)\partial_i\partial_k u_{kj}^G + \mu^0\partial_k\partial_k u_{ij}^G + \rho^0\omega^2 u_{ij}^G = -\delta_{ij}\delta(\mathbf{x} - \mathbf{x}'). \tag{2.17}$$

To obtain the vertical component of the displacement due to a vertical point excitation, we select $i, j = 3$. Then, the relevant component of the elastic Green's function satisfies

$$(\lambda^0 + \mu^0)\partial_3\left(\partial_1 u_{13}^G + \partial_2 u_{23}^G + \partial_3 u_{33}^G\right) + \mu^0\partial_k\partial_k u_{33}^G + \rho^0\omega^2 u_{33}^G = -\delta(\mathbf{x} - \mathbf{x}'). \tag{2.18}$$

From this equation, a scalar equation can be obtained by neglecting the terms[2] $\partial_1 u_{13}^G$ and $\partial_2 u_{23}^G$. This is consistent with our assumption that the vertical component of particle velocity dominates at the scatterer. Equation (2.18) then simplifies to:

$$(\lambda^0 + \mu^0)\partial_3\partial_3 u^G + \mu^0\partial_k\partial_k u^G + \rho^0\omega^2 u^G = -\delta(\mathbf{x} - \mathbf{x}'). \tag{2.19}$$

We have omitted the subscripts from the Green's function to distinguish between the component from the elastic Green's function u_{33}^G and its scalar approximation u^G. Using the compressional wave velocity $c_P = \sqrt{\frac{\lambda^0+2\mu^0}{\rho^0}}$ and shear velocity $c_S = \sqrt{\frac{\mu^0}{\rho^0}}$, Equation (2.19) can be written as (Los et al., 2001, e.g.):

$$\left[\frac{c_P^2}{c_S^2}\partial_3\partial_3 + \partial_\alpha\partial_\alpha\right] u^G + \frac{\omega^2}{c_S^2}u^G = -\delta(\mathbf{x} - \mathbf{x}'). \tag{2.20}$$

This equation exhibits anisotropy, as the wave front is stretched in the longitudinal direction. Introducing the scaled vertical coordinate $\zeta = \frac{c_S}{c_P}z$, we obtain the scalar Helmholtz equation:

$$\left[\partial_k\partial_k + \frac{\omega^2}{c_S^2}\right] u^G = -\frac{c_S}{c_P}\delta(\mathbf{x}_L - \mathbf{x}'_L, \zeta - \zeta'), \tag{2.21}$$

which we solve in Section D.2, using the boundary condition of a traction free surface at $z = 0$ (i.e. $\partial_\zeta u^G = 0$, $z = 0$). Note that ∂_k in Equation (2.21) is with respect to the scaled coordinate, i.e., $\partial_k = (\partial_x, \partial_y, \partial_\zeta)$. The result is the well-known half space Green's function (for example Morse and Feshbach, 1953, p. 849), in the space-frequency domain given by:

$$u^G(\mathbf{x}, \mathbf{x}') = u^G(\mathbf{x}_L - \mathbf{x}'_L, z, z') = \frac{c_S}{4\pi c_P}\left(\frac{\exp\left(-\mathrm{i}\omega\frac{|\mathbf{x}-\mathbf{x}'|}{c_S}\right)}{|\mathbf{x} - \mathbf{x}'|} + \frac{\exp\left(-\mathrm{i}\omega\frac{|\mathbf{x}-\breve{\mathbf{x}}'|}{c_S}\right)}{|\mathbf{x} - \breve{\mathbf{x}}'|}\right), \tag{2.22}$$

where $\breve{\mathbf{x}}'_L = \mathbf{x}'_L$ and $\breve{z}' = -z'$. In order to simplify notation, we will use z instead of ζ for the scaled coordinate from this equation onwards.

[2]This type of assumption also occurs in soil mechanics, where it is used to calculate vertical stresses in a medium with horizontal constraints (Harr, 1966, but originally attributed to Westergaard). In the context of wave propagation it has been applied by Barends (1971) to calculate the response of an elastic half-space due to a vertical impulsive force source.

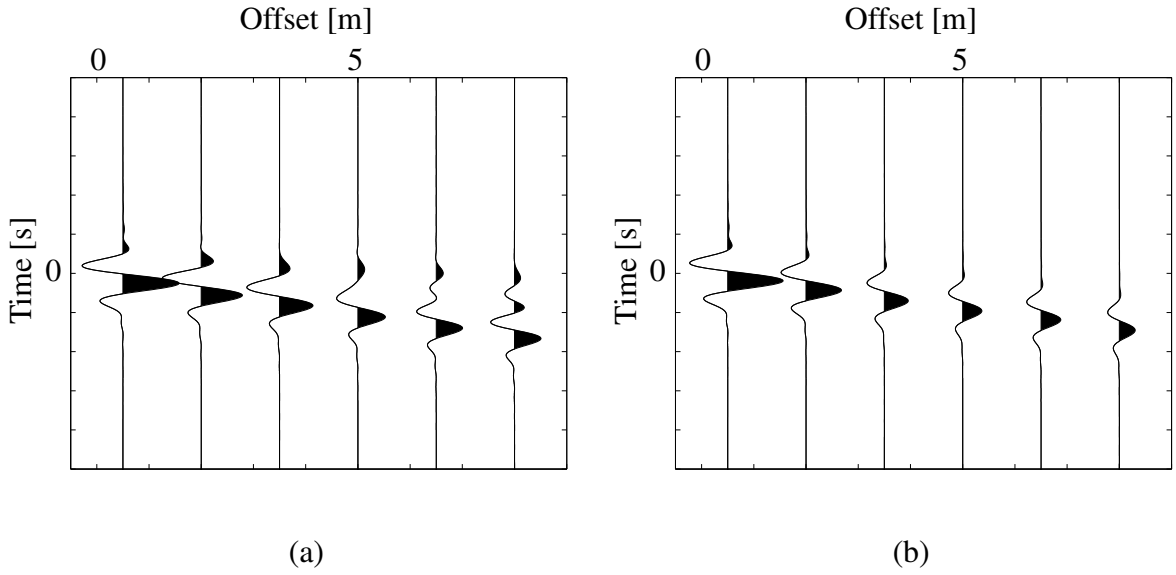

Figure 2.2: *Vertical velocity as a function of time and source-receiver offset at the surface due to a vertical point source at the surface. The parameters used to calculate these wave fields, are such that the dominant wavelength of the Rayleigh wave is about 6m. (a) Calculated with Equation (2.18). (b) Same, but neglecting horizontal components, using the scalar Green's function (from Los et al., 2001).*

In the actual elastodynamic near field, the factor $\frac{1}{R}$ (where R is the distance from the source to the observation point) dominates (Morse and Feshbach, 1953, p. 1784). This factor is of the same order as the ones that occur in our Green's function of Eq. (2.22). Hence, this Green's function should allow us to predict the amplitude behavior of the elastodynamic near field correctly. In contrast, in an asymptotic expression for the far-field behavior of the elastic Green's function u_{33}^G, a factor $\frac{1}{\sqrt{R}}$ dominates (Aki and Richards, 1980, p. 217). Therefore, the asymptotic surface wave Green's function would have been the correct choice if we were interested in the behavior of surface waves at larger distances (Blonk, 1994, for example).

Apart from the amplitude behavior, the kinematic character of the Green's function is an important factor. The Green's function for an elastic half space contains surface waves. These surface waves have linear move-out, while in the scalar Green's function this is hyperbolic move-out. However, in the near field, close to the (secondary) source, no surface wave has yet built up, and therefore the asymptotic surface wave Green's function is not a good approximation for this region (Wu and Ben-Menahem, 1985, for example).

Figure 2.2(a) illustrates what we have discussed so far. It depicts the *elastic* wave field calculated with u_{33}^G (i.e., the solution to Equation (2.18)), while 2.2(b) shows the *scalar* wave field calculated with u^G (i.e., the solution to Equation (2.19)). Both u_{33}^G and u^G have been calculated

using the Cagniard method (for example Aki and Richards, 1980, p.(p.) 218 f(f)). For distances smaller than 6 m (which corresponds roughly to the Rayleigh wavelength) both figures are arguably similar, while for larger distances the scalar wave field starts to deviate from the elastic one. Because we are mainly interested in the wave field within a Rayleigh wavelength from the source/scatterer, this deviation at larger distances is not a critical problem.

With the Green's function (Eq. (2.22)) we arrive at the following scalar representation for the vertical component of the velocity:

$$v^1(\mathbf{x}) = \omega^2 \int_{\mathcal{D}} u^G(\mathbf{x}_L - \mathbf{x}'_L, z, z')\Delta\rho(\mathbf{x}')v(\mathbf{x}')\mathrm{d}V. \tag{2.23}$$

By replacing $u^G(\mathbf{x}, \mathbf{x}')$ with $u^G(\mathbf{x}_L - \mathbf{x}'_L, z, z')$ under the integral in this equation, we have explicitly used the fact that the embedding medium is (laterally) homogeneous close to the surface.

2.1.5 Parameterization

Following Blonk and Herman (1994), we define a suitable parameterization for the near-receiver scattering problem. We assume that the scattering medium can be thought of as being composed of N, thin, laterally homogeneous layers with equal thicknesses Δz, centered around $z^{(i)}$. If Δz is small enough, we can rewrite the integration over the depth direction as a summation over discrete depths. In this way, we approximate the integral over one depth interval as the value of the function at $z^{(i)}$ times the thickness of this interval. For the field at z, Equation (2.23) can then be written as:

$$v^1(\mathbf{x}_L, z) = \omega^2 \sum_{i=0}^{N-1} \Delta z \int_{\Sigma} u^G(\mathbf{x}_L - \mathbf{x}'_L, z, z^{(i)})\Delta\rho(\mathbf{x}'_L, z^{(i)})v(\mathbf{x}'_L, z^{(i)}), \mathrm{d}A \tag{2.24}$$

where $\Delta z = z^{(1)} - z^{(0)}$ and $\mathbf{x}_L = (x, y)$.

Blonk (1994, pp. 50-51) shows that for estimating and predicting scattered surface waves, it suffices to take only one such layer into account, even when the actual scattering distribution consists of more layers (see also Hudson, 1977; Snieder, 1986, e.g., for similar approximations for scattering of surface waves by topography). Because we assume that scattering takes place close to the receivers, we take this reference layer at the surface ($z^{(i)} = z^{(0)}$). For the field at the surface (i.e. $z = 0$) we arrive at:

$$v^1(\mathbf{x}_L, 0) = \omega^2 \Delta z \int_{\Sigma} u^G(\mathbf{x}_L - \mathbf{x}'_L, z^{(0)})\Delta\rho(\mathbf{x}'_L, z^{(0)})v(\mathbf{x}'_L, z^{(0)})\mathrm{d}A. \tag{2.25}$$

Note that the original volume integral in Equation (2.23) is now reduced to evaluating an integral over the surface Σ at one depth, $z^{(0)}$.

At this point we define the impedance function as:

$$\sigma(\mathbf{x}'_L, z^{(0)}, \omega) = \omega^2 \Delta z \Delta\rho(\mathbf{x}'_L, z^{(0)}). \tag{2.26}$$

Here, Δz is interpreted as the thickness of the impedance layer at the surface. This function depends on frequency, because we have included the factor ω^2 into it. However, we also let it depend on frequency to compensate for some variation in the actual depth of the scattering. In this way, depth dependence is converted into frequency dependence, much like in a dispersion relation, where vertical structure is related to frequency-dependent behavior of the modal amplitudes of guided surface waves.

If the heterogeneity is close to the receiver (i.e. $z^{(0)}$ is small compared to the seismic wavelength), we can replace the wave field (in the scattering domain) on the RHS of Equation (2.25) with the wave field measured at the surface: $v(\mathbf{x}_L, z^{(0)}) \approx v^{meas}(\mathbf{x}_L, 0)$. This approach is also taken by Herman et al. (2000a) in the case of tube-wave scattering in a borehole, where it is assumed that the wave field in the borehole is uniform and one can approximate scattering by wash-out zones as a one-dimensional problem.

Finally, we obtain the approximate near-receiver scattering equation:

$$v^1(\mathbf{x}_L, 0) = \int_\Sigma u^G(\mathbf{x}_L - \mathbf{x}'_L, z^{(0)})\sigma(\mathbf{x}'_L, z^{(0)})v^{meas}(\mathbf{x}'_L, 0)\mathrm{d}A, \tag{2.27}$$

where v^{meas} denotes the actual vertical velocity measured by the geophones at the surface. By substituting the data measured at the surface, we do not rely on the Born approximation and we include multiple scattering and resonances which may occur in cavities in the near subsurface, for example. Equation (2.27) is the basis of our estimation-and-suppression algorithm for near-receiver scattered waves.

2.2 Formulation of the Inverse Scattering Problem

In the previous section, we have derived an approximate integral representation that allows one to calculate near-receiver scattering efficiently, using wave-field quantities actually recorded by geophones in the field. In this section we use this representation (2.27) as the basis of an inversion scheme to estimate the near-surface scattering impedance σ. The main difference is that the impedance function in the formulation in the previous section is assumed to be known, while in this section, it is the scattered field that is known, while both σ and the field in the scattering domain are unknown. In general, there are two approaches to solve such an inverse problem.

The first one is a direct approach, where one constructs an (approximate) inverse for the modeling operator (Cohen et al., 1986; Miller et al., 1987, for example). There has been considerable interest in developing such migration schemes for applications in the oil industry, but also for medical applications. Each migration scheme has certain practical advantages over others, but they have in common that they work best with densely and regularly sampled data. If data are missing (due to obstacles at the surface for example), these methods give artifacts (Sevink and Herman, 1994, for example).

The second technique is (linearized) inverse scattering (e.g. Tarantola, 1984; Kleinman and van den Berg, 1991). Here, the material properties are determined by minimizing a cost func-

tional by iteratively updating the model parameters. This type of method only predicts the measured data in the observation points. In this way, they are less sensitive to sampling geometry (as pointed out by Sevink and Herman, 1994). Moreover, it is straightforward to include data from multiple experiments in the same minimization.

We have chosen the second (inverse scattering) approach because it is our aim to estimate a scattering model that best fits the observed scattered data.

2.2.1 Preconditioning

The elastic wave field can be written as a part that accounts for propagation in the embedding, v^0, and a part that accounts for scattering by heterogeneities close to the surface, v^1 (see also Section 2.1.2):

$$v(\mathbf{x}, t) = v^0(\mathbf{x}, t) + v^1(\mathbf{x}, t). \tag{2.28}$$

Note that v^0 can be quite complex in this case. In principle, it includes many events: reflections from the subsurface and possibly multiples, refractions, etc. Thus v^1 *only* accounts for scattering from near-surface heterogeneities.

Here, we calculate v^1 with Equation (2.27), requiring an estimate of the impedance function. To obtain this estimate, however, we need an estimate of the near-surface scattered energy v^1. Thus, we are faced with a *catch 22* situation: to calculate the scattered field, we need the impedance function and to calculate the impedance function, we need an estimate of the scattered energy. This can be solved only if we can obtain an independent estimate of the near-surface scattered energy.

At this point, the similarity of our method to residual statics method becomes clear. In statics, one aims to estimate time shifts in such a way that they correct an entire shot record. These time shifts, however, are derived from one or more time windows in the shot record (Cox, 1999, e.g). In other words, the time shifts are derived from a subset of the available data and then applied to the entire data set.

In fact, we use a similar approach here. A shot record can be thought of as a collection of events. If the scattering takes place close to the receivers, all events — from any angle — pass through the same anomalies. This implies that we can use one such event to derive the near-surface impedance function and use this impedance function to calculate the scattered energy on all (other) events, just like in residual statics. For this purpose we can use an event that is separable in time (using a window) from the rest of the events and shows clear evidence of scattering near the surface. This scattering should be included as much as is possible.

Using the idea of a shot record as a collection of events, we can write for the data:

$$v(\mathbf{x}, t) = d(\mathbf{x}, t) + r(\mathbf{x}, t), \tag{2.29}$$

where d is the *derive* — or reference — event separated by time windowing, and r denotes the rest of the data containing all other events. To derive the image from d we first estimate the scattered energy excited by the reference event. As in Equation (2.28), we decompose the event

into a part accounting for propagation in the embedding medium, d^0, and a part accounting for local perturbations, d^1:

$$d(\mathbf{x}, t) = d^0(\mathbf{x}, t) + d^1(\mathbf{x}, t). \tag{2.30}$$

We discuss this decomposition step in more detail when we apply our method to laboratory and field data. For now, we assume that we have separated the scattered energy from the smooth event using a filtering method, for example. This independently obtained scattered energy is the input for the inversion.

2.2.2 Inversion

We estimate the surface impedance function, σ, by minimizing the squared difference between the scattered field from the reference event and the scattered field calculated with Equation (2.27).

To set up the inversion scheme, we write Equation (2.27) for the reference event in operator form:

$$d_J^{1,op} = \mathcal{K}_J^d \sigma, \tag{2.31}$$

where we use $d_J^{1,op}$ for the modeled scattered field and $\mathcal{K}_J^d$ is an operator defined through (see also Eq. (2.27))

$$\left\{\mathcal{K}_J^d \sigma\right\}(\mathbf{x}_L, 0) = \int_\Sigma u^G(\mathbf{x}_L - \mathbf{x}'_L, z^{(0)}) \sigma(\mathbf{x}'_L, z^{(0)}, \omega) d_J^{meas}(\mathbf{x}'_L, 0) \mathrm{d}A, \tag{2.32}$$

and where J denotes the shot-index. We define the cost function as:

$$F = \frac{\Sigma_J ||d_J^1 - \mathcal{K}_J^d \sigma||^2}{\Sigma_J ||d_J^1||^2} + \lambda ||\sigma||^2. \tag{2.33}$$

Here, λ is a stabilization parameter determining the weight given to minimization of the model and the residual. In Section C.2 we discuss a method to choose λ. We have included the possibility to simultaneously minimize the scattered field from different experiments and obtain an impedance function consistent with several shots. Now, the impedance function is found by iteratively updating σ until it minimizes the cost function F, in the following way:

$$\begin{aligned} \sigma_0 &= 0, \\ \sigma_N &= \sigma_{N-1} + \alpha_N \gamma_N, \qquad N \geq 1. \end{aligned} \tag{2.34}$$

Here, α_N is the step size, γ_N is the update direction and N is the iteration number.

For the minimization, we have chosen a conjugate gradient scheme following Van den Berg (2002). This scheme is briefly outlined in Appendix C, while an efficient scheme to compute the operators discussed above is discussed in Appendix D.

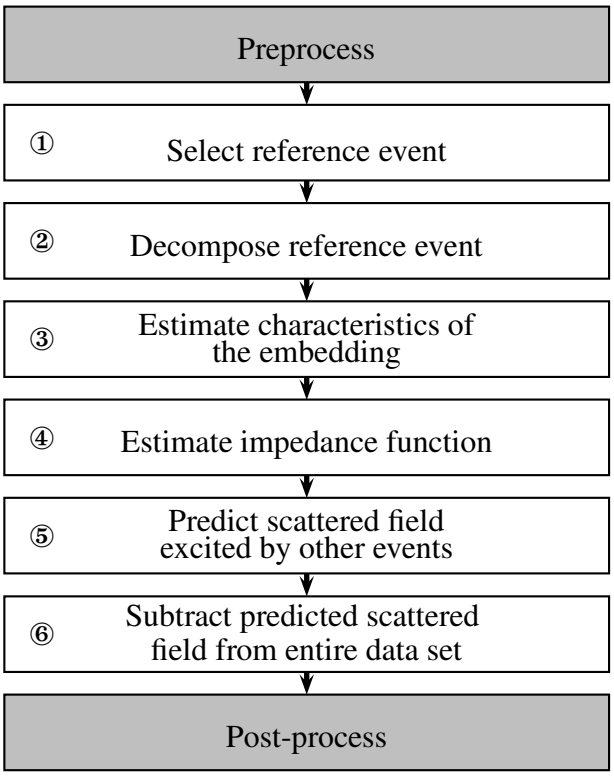

Figure 2.3: Scheme of our method for suppressing near-receiver scattered noise.

2.3 Suppressing Near-Receiver Scattered Waves

With the basic equations in place, we now summarize our method to suppress near-receiver scattered waves.

Figure 2.3 is a schematic of this method. The shaded boxes represent steps that are carried out in standard seismic processing – they are not inherent to our method. In principle, our method can be applied to raw pre-stack common-shot or common-midpoint gathers. Preprocessing should be minimal, but could include enhancing the signal-to-noise ratio. After application of our algorithm, the usual processing can be done.

We briefly review the steps of our method here:

① *Select reference event.* Like in residual statics, we first select a suitable event from the field record. This event should clearly contain scattering by near-surface heterogeneities. Furthermore, it should – ideally – not interfere with other arrivals. We need to use different time windows to obtain an independent estimate of the surface impedance function.

The reference event is denoted d throughout this thesis.

② *Decompose reference event.* In the near-receiver problem, the scattered field can *interfere* with the incoming wave field. Therefore, to extract the relevant scattered energy, sophisticated filtering techniques or wave-field separation methods are required (see also Herman et al., 2000a). This estimate of the scattered field from the reference event is denoted d^1.

③ *Estimate characteristics of the embedding.* This step essentially consists of estimating the surface (Rayleigh) wave velocity. This velocity is required to calculate the Green's function occurring in Equation (2.27).

④ *Estimate impedance function.* Using the estimated scattered field from step ② as input, we estimate the impedance function by iteratively updating σ by minimizing Equation (2.33). This impedance function can be interpreted as a distribution of near-surface scatterers, lumped at the surface (i.e., an image of near-surface scatterers).

⑤ *Predict scattered field excited by other events.* Here, we substitute the wave field measured at the surface for the wave field at the scatterer (see Section 2.1.3). Together with the estimate of the velocity in the embedding and the impedance function, this allows us to *directly* calculate the scattered field v^1 using Equation (2.27).

⑥ *Subtract predicted scattered field from entire data set.* The last step of this scheme is subtracting the predicted scattered field v^1 from the shot record so that the near-receiver scattered energy is canceled due to destructive interference with the predicted scattered field. We have then obtained an estimate of the wave field that would have been measured if there were no near-surface heterogeneities, v^0.

3

Application to Synthetic and Laboratory Data

Our method is based on an approximate integral representation for the near-receiver scattered field. In the derivation of this representation, we have made several simplifying assumptions. Most of these assumptions have been validated separately by others (e.g. Blonk, 1994; Ernst, 1999; Los et al., 2001). However, to use the equation resulting from making all these assumptions simultaneously, we need to investigate if, and to what extent it is accurate.

To this end, we have designed a configuration that allows for testing the two main assumptions, using three-dimensional, elastodynamic, numerically modeled data. We consider scattering of upcoming events in the first part of this chapter. By varying the depth of the scattering and the angle between reference and target events, we test the sensitivity of our method to these parameters. At the end of the first section, we introduce a measure to quantify the spatial continuity of reflectors and the trace-to-trace coherence in order to compare the data before and after application of our algorithm. At the same time, this enables us to investigate the sensitivity of the algorithm with respect to the Rayleigh-wave velocity.

In the second part of this chapter, we describe two laboratory experiments of surface-wave scattering on an Aluminum block. These experiments have been performed in collaboration with the Physical Acoustics Laboratory (PAL) at Colorado School of Mines in Golden, Colorado (US).

The first experiment involves surface waves only, to allow maximum insight in the scattering process. At the same time, the first experiment is an additional validation of our formulation, but now for horizontally traveling incident waves. This experiment also serves to introduce the entire sequence of steps of our algorithm. We illustrate each step with examples taken from this experiment.

In the second experiment, we topped the Aluminum with a (low velocity) Lucite layer to simulate more realistic situations, for instance due to the presence of multiple reflections from the Aluminum-Lucite boundary. Now, the source is excited at the bottom of the block, so we excite upcoming body waves that interact with the scatterer to excite surface waves.

3.1 Test on Synthetic Data

The goal of our method is to estimate and subtract near-receiver scattered waves from seismic data. The basic idea is that we first select a reference event from the data and use this event to estimate a near-surface impedance function. We use this impedance function to calculate the scattered field excited by other, 'target', events using Equation (2.27). Subtracting the calculated scattered field then gives an estimate of the target events in the absence of near-surface scattering.

The impedance function is determined using an inverse scattering method, thus requiring the near-receiver scattered field as input. Consequently, we need to separate the scattered wave field from the reference event. In the test on synthetic data, this is, however, not necessary. The scattered field in this case is 'perfectly' separated from the reference event.

3.1.1 Objective

Here, we investigate the validity of our assumptions and the limitations of our method. In Chapter 2, we used various – mainly physical – arguments to simplify the general integral representation for scattered elastic waves (Equation 2.9).

Essentially, those arguments can be summarized in two main assumptions. These are:

A1 We assume that the vertical component dominates the horizontal components of the field at the scatterer and at the same time we neglect interaction between horizontal components and the vertical component in the Green's function.

A2 We assume that scattering takes place close to the surface and consequently we can concentrate the distribution of scatterers in a layer at the surface.

These steps lead to the following scalar equation:

$$v^1(\mathbf{x}_L,0) = \int_\Sigma u^G(\mathbf{x}_L - \mathbf{x}'_L, z^{(0)})\sigma(\mathbf{x}'_L, z^{(0)})v^{meas}(\mathbf{x}'_L,0)\mathrm{d}A, \tag{3.1}$$

describing the dominant component of the wave field. Because we concentrated scattering in a layer at the surface, the integral in Equation (3.1) is over the *surface* Σ. Inspection of Equation (3.1), reveals that it should hold for any upcoming event, regardless of the angle at which it arrives at the scatterer.

By using an elastic modeling program, we can test if the near-receiver scattered field can be modeled with sufficient accuracy using a scalar representation (in fact, in section 2.1.4 we have already shown that assumption A1 can be used with a fair degree of accuracy when scattering takes place within about a Rayleigh wavelength from the receivers). For this purpose, we use a 3-D elastic integral-equation modeling method, that has been especially developed for analyzing near-receiver scattering problems. For a detailed description of this method and for more examples, see Riyanti and Herman (2005).

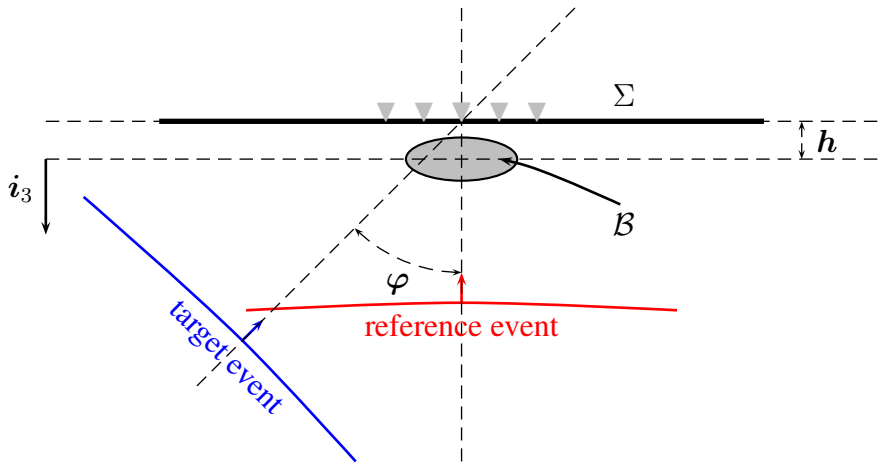

Figure 3.1: *Validation configuration. The scatterer is located at an average depth of h m below the acquisition surface Σ. The angle between the reference and target event is denoted by φ.*

By deriving the near-surface impedance from a vertically upcoming plane wave, and then predicting the scattered field on independent events with increasing angles of incidence, we can test the second assumption. In addition, we vary the depth of the scattering distribution, allowing us to determine the limits of the validity of our formulation.

The configuration of our test model is shown in Figure 3.1. We consider scattering of an upcoming wave by a scatterer embedded in a homogeneous elastic half space. The vertical point source is located at a 300 meter depth. The P-velocity of the embedding is 1100 m/s, while the S-wave velocity of the half space is 450 m/s. The density of the embedding is 2000 kg/m^3 and the density of the scatterer is 5000 kg/m^3. The source wavelet has a flat spectrum between about 20 and 100 Hz. From analyzing the data modeled with these parameters, we find that the Rayleigh wave appears to have a dominant frequency of about 30 Hz, which implies a wavelength, λ_R, of about 14 m.

3.1.2 Results

Sensitivity with Respect to the Angle between the Reference and Target Event

In the first test, we keep the scatterer fixed at the surface, while we move the horizontal position of the source progressively away from the horizontal position of the scatterer. In this way, the condition of scattering close to the surface (in the near field) is fulfilled and we increase the angle of incidence of the target event. Because we choose the vertically incident wave field as the reference event, this angle corresponds to φ in Figure 3.1.

The idea is now to first estimate an impedance function using the scattered energy excited

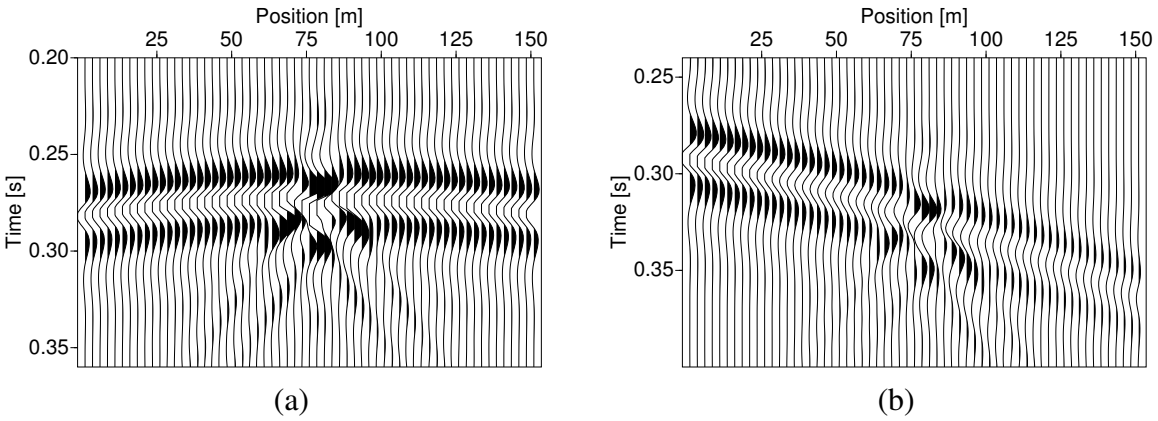

Figure 3.2: *(a) An upcoming P-wave excites scattered waves; this event is used to derive the impedance function. (b) Target event from an angle of about 30 degrees from the vertical. In this experiment, the average depth of the scatterer $h = 4$ m.*

by the reference event, shown in Figure 3.2a. In this way, the impedance function is obtained independently from the target events. Then, we predict and subtract the scattered field excited by the target event. We have done this for events with increasing angles of incidence up to the point where the predicted scattered field started to deviate significantly from the actual scattered field.

Figure 3.2b shows the target event with an angle of about 30 degrees from the vertical. When we use the impedance function obtained from the data of Figure 3.2a to predict the scattered field excited by the event in Figure 3.2b we obtain a good result. This is illustrated in Figure 3.3. Figure 3.3a shows a detail of the target in the area above the scatterer (from 50 to 100 m). The result after predicting and subtracting the scattered energy is shown in Figure 3.3b. We observe that the scattered field has been removed well. There is a small remnant of the Rayleigh wave visible from the remaining interference in the second lobe of the wavelet, but most of the interference is successfully removed. The difference of these two figures corresponds to the predicted scattered field and it is shown in Figure 3.3c.

We have removed the scattering effectively from this event, while the event was not used to derive the impedance function. However, when we further increase the angle, the predicted scattered field and the actual scattered field start to deviate significantly. We can conclude that when the scatterer is close to the surface, we can use a reference event to estimate the impedance function and use this impedance function to predict the scattered field on another event with a

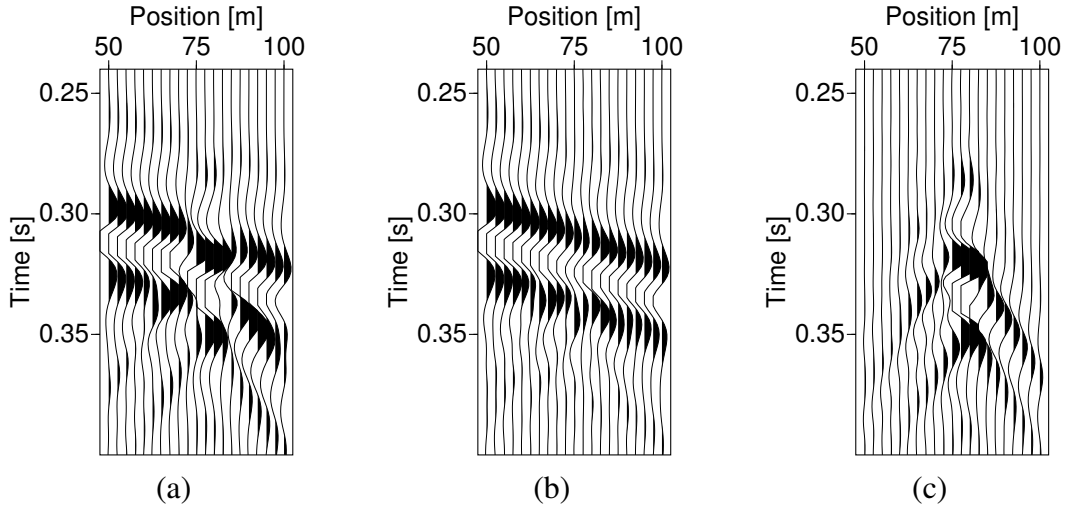

Figure 3.3: *(a) Detail of the target event (Figure 3.2b) from 50 to 100 m. (b) Same detail after predicting and subtracting scattered energy. (c) Difference between (a) and (b), i.e. the predicted scattered field. The average depth* $h = 4$ *m.*

difference in angle at least up to about 30 degrees.

Sensitivity with Respect to the Depth of the Scatterer

In the second experiment we also vary the depth of the scatterer. Doing so, allows us to investigate the limitation of our approach with respect to the depth of the scatterer. In fact, this experiment consists of repeating the first experiment, but now for different depths of the scatterer. We have done this for a few different depths and noted that for a depth $h = 13$ m (about the Rayleigh wavelength) we started to note the limitation of our method (this is the average depth of the scatterer; the top of the scatterer is 8 meters below the surface).

Again, we derive the impedance function from a vertically incident P-wave. However, when we estimate the scattered waves on target events, the modeled scattered field starts to differ from the actual scattered field, for angles exceeding 10 degrees from the vertical.

In Figure 3.4a we show a detail of the target event with an angle of incidence of about 10 degrees from the vertical. Figure 3.4b shows the the same event after subtracting the predicted scattered field shown in Figure 3.4c. Because as the depth of the scatterer increases, the excited scattered field becomes weaker, the result is still quite acceptable. However when we compare the actual scattered energy (not shown here) and the predicted scattered energy, we note that they start to deviate significantly in this case. Hence, we find that our method is limited to small

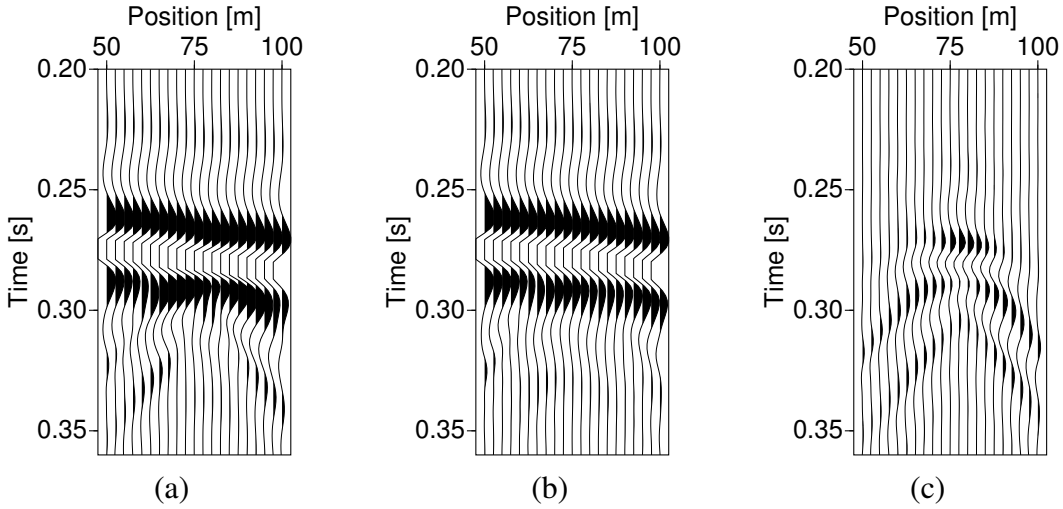

Figure 3.4: *(a) Detail of the target event between 50 and 100 m. The (average) depth, h, of the scatterer is now 13 m, which corresponds roughly to the Rayleigh wavelength. (b) Same detail after predicting and subtracting scattered energy. (c) Difference between (a) and (b) , i.e. the predicted scattered field.*

angles between reference and target events when the scatterer is at a distance from the surface of about one Rayleigh wavelength.

3.1.3 Waveform and Continuity

Statics are often considered as a main contributor to a poor stack response, because when the waveforms are out of phase (i.e. the event is not continuous), they do not align to produce a strong amplitude in the stack. Moreover, static shifts are known to act as a high-cut filter (Marsden, 1993; Cox, 1999; Berni and Roever, 1989). Because static shifts are pure phase shifts, this means that the waveform of a particular event remains the same over different traces, but the waveform of the stack is altered such that the higher frequencies are attenuated due to destructive interference. Amplitude changes on the other hand, scale the output of a stack, but do not change the wave shape.

In principle, such generalizations do not hold for near surface-scattering. This is because the individual waveforms can also be changed by scattering, especially when reverberations play an important role (Combee, 1994, for example). In fact, this is also the reason that Baeten et al. (2000) suggest wave-field-based imaging methods to compensate for time and amplitude

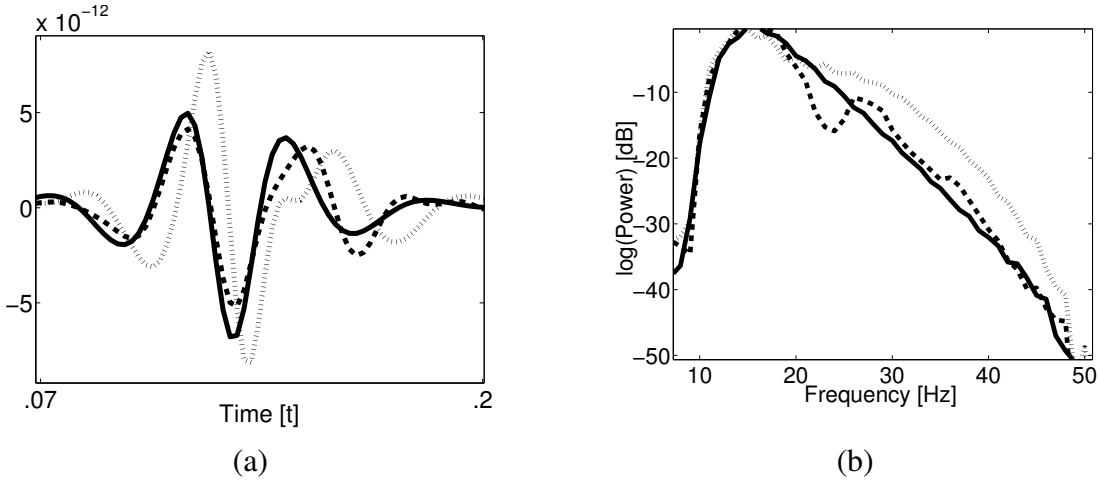

Figure 3.5: *(a) Waveforms of the P-wave on the trace in the center above the cavity (at 75 m). The traces have been shifted, so the timing does not correspond to Figure 3.3, but the time scale does. The dotted line denotes the waveform of the target event (with scatterer), the solid line represents the desired waveform (without scatterer) and the dashed line represents the waveform obtained after predicting and subtracting the scattered energy. (b) The same waveforms but now in the frequency domain (in dB scaled to 1).*

anomalies induced by scattering.

Like in the case of statics, the stack response will typically be degraded by near-receiver scattering due to the various phase and amplitude differences between the different traces. However, because the individual waveforms can be quite complex, it is not immediately clear that stacking acts as a high-cut filter in this case.

In contrast to static correction methods, wave-field based multichannel methods should be capable of correcting for both the time shift and amplitude distortions. In this section, we investigate whether our method is able to restore the original waveform (i.e. the waveform of the event if there were no scatterer).

Wave Shape

The objective of our method is to remove interference between target reflections and scattered waves excited near the surface. This implies aligning the arrival and restoring the waveform.

As an example, consider the first synthetic test again. The results of this test are shown in Figure 3.3.

In Figure 3.5 we compare the waveforms of the trace at 75 m for each of the wave fields shown in Figure 3.3a-b to the desired waveform. The desired waveform corresponds to the waveform that we would have measured in the same model without heterogeneity. It is repre-

Table 3.1: *Semblance calculated for different events.*

Mean Depth 5 m	
Event	Semblance
Before	0.58
After	0.96
Desired	0.97

Mean Depth 13 m	
Event	Semblance
Before	0.91
After	0.99
Desired	0.99

sented by the solid line in Figure 3.5a. The dotted line represents the waveform of the wave field in the model with scatterer (Figure 3.3a).

We clearly observe a time shift in the first break, due to the difference in velocity in the embedding and in the anomaly. This shift can be predicted by an analysis of rays (like in statics) and it can be removed by a static shift. However, additional phase and amplitude distortions can be observed. It is these distortions that can not be predicted by static correction methods.

After applying our method, we obtain the dashed waveform, depicted in Figure 3.5. Comparing it to the desired (solid) waveform, we observe that it has fairly well been restored.

The corresponding waveforms in the frequency domain are shown in Figure 3.5b. In this case the dotted line departs from the solid line, indicating that scattering increased the energy at higher frequencies when compared to the desired waveform. Furthermore, we observe that the spectrum of the waveform after predicting and subtracting the scattered field (the dashed line) agrees well with the spectrum of the desired waveform. Hence, we may conclude that we can restore the original waveform well.

Finally, we remark that it seems contradictory that we have attenuated the higher frequencies in the waveform. Typically, one aims at preserving as much of the high-frequency content in the seismic signal as is possible to obtain maximum resolution. However, because the higher frequencies in our example have been introduced by scattering near the receivers they constitute information from the near-subsurface and they may be erroneously attributed to deeper subsurface effects such as those analyzed for stratigraphic information. Consequently, in order to restore the actual wavelet, they should be attenuated. Conversely, our method should enhance higher frequencies if they are attenuated due to scattering.

Coherency and Continuity

We have shown that we can restore the wave shape fairly well after it has been altered by scattering. In this way, the event will be more coherent and should produce a greater amplitude in the stack than stacking its less coherent counterpart (Telford et al., 1990). Investigating the effect on the stack therefore provides another validation of our method. So, after analyzing the effect of our method on one trace, we now investigate what is the effect of our method on

several traces, to see if the trace-to-trace coherency has increased.

To this end we use semblance (Neidell and Taner, 1971). Telford et al. (1990) define semblance as the ratio of the energy of the stack compared to the energies of the individual traces over a certain time interval. This ratio is expressed as:

$$S = \frac{\sum_{j=k-N/2}^{k+N/2} \left\{ \sum_{i=1}^{M} d(j,i) \right\}^2}{M \sum_{j=k-N/2}^{k+N/2} \sum_{i=1}^{M} d^2(j,i)}. \tag{3.2}$$

Here, the term in the brackets in the numerator is the sum of M traces (the stack). The time gate is a window of length N centered around time k.

Before we calculate the semblance, we first apply (hyperbolic) move-out and then place a window around the event such that the remnants of the surface wave with linear move-out are not included in the calculation. Typically, the time gate for calculating the semblance is about the length of one period of the waveform. When we do this for the events shown in Figure 3.3a-b and Figure 3.4a-b, we obtain the results shown in Table 3.1. As a reference we have again also calculated the semblance of the corresponding events in the model without heterogeneity (the desired events).

These tables demonstrate that the continuity of the event after applying our method is about the same as the continuity of the desired events. This improvement ranges from a few percent to 50 %, depending on the strength of the scattered energy relative to the energy in the total wave field. Note that we calculated these semblances only for the range from 50 to 100 m (M=20).

3.1.4 Sensitivity with Respect to the Velocity of the Embedding

Coherency measures are often used to determine parameters such that they optimize a stack. They can also be used to investigate the sensitivity of a method to certain parameters. Now that we have introduced a measure to calculate the trace-to-trace continuity of seismic events, we can test the sensitivity of our method with respect to the (Rayleigh wave) velocity of the embedding medium. In practice, this parameter is estimated from the data and is therefore prone to deviations from the actual value.

The geometry of the test model is the same as in the previous example, but now the mean scattering depth is 9 m. As in the previous examples, the reference event is a vertically incident P-wave. The target event is fixed at an angle of about 10 degrees from the vertical. We repeat the same test for this target event, but for varying surface wave velocity.

The results are shown in Figure 3.6. If we calculate the semblance of the target event obtained after predicting and removing the scattered energy using surface wave velocities ranging from 300 to 1000 m/s, we obtain the result shown in Figure 3.7. Before calculating the semblance, we have again placed a time window around the event to suppress the remnants of part of the scattered wave with linear move-out. The semblance of the original target event (with

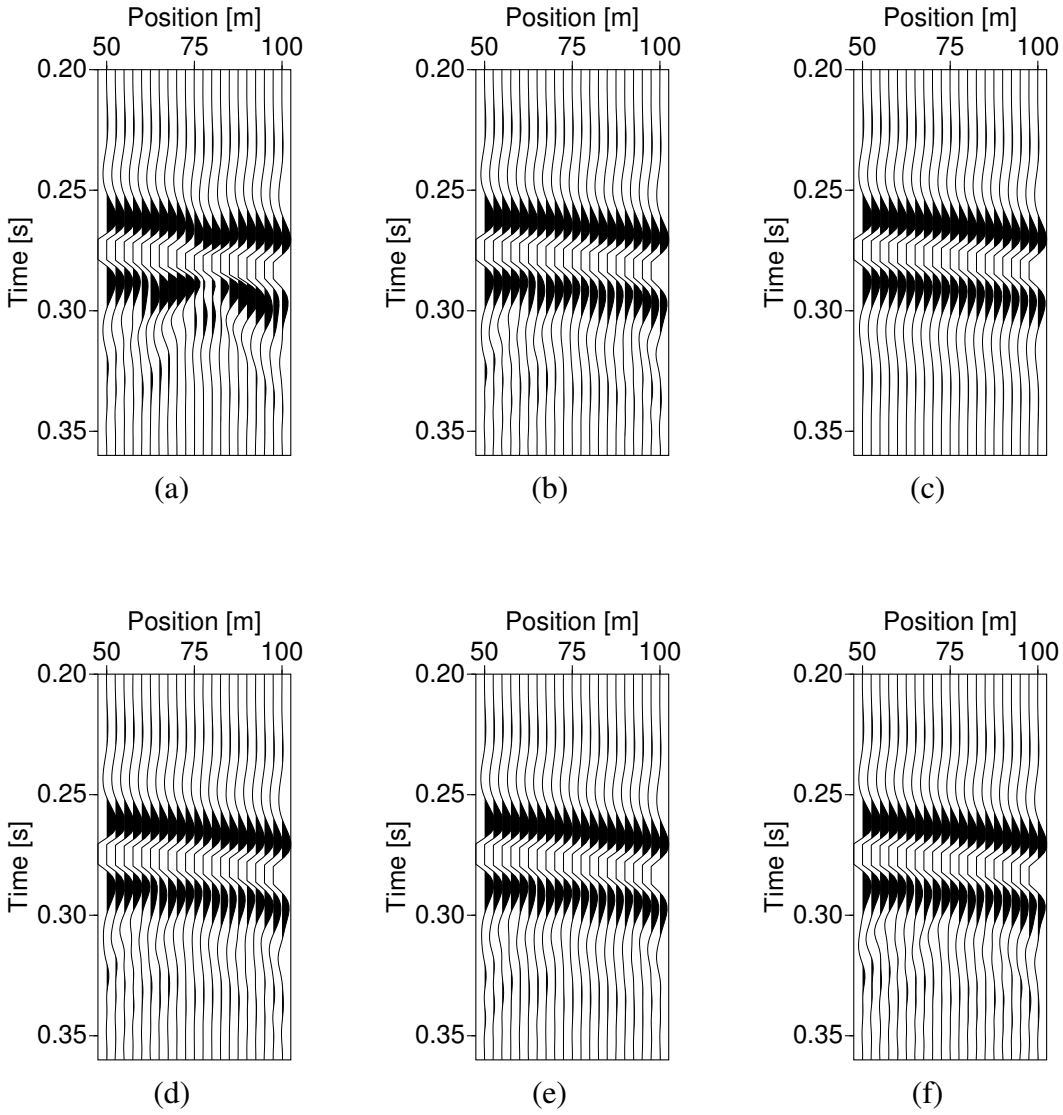

Figure 3.6: *(a) Detail of the target event from 50 to 100 meters. (b) The same detail of the target event, but after predicting and removing the near-surface scattered energy. Here we have used the correct Rayleigh wave speed (about 400 m/s). (c) The desired wave field that would have been measured without anomaly. Note that the result of (b) is almost the same as the wave field in this display. (d) The same detail, but after predicting and removing the scattered energy using a surface wave velocity of 300 m/s. (e) Same as (d), but using a surface wave velocity 500 m/s. (f) Same as (d), but using a surface wave velocity 1000 m/s. Apart from the remnants of the surface wave with linear move out, the continuity of these event has been equally well restored using the different velocities.*

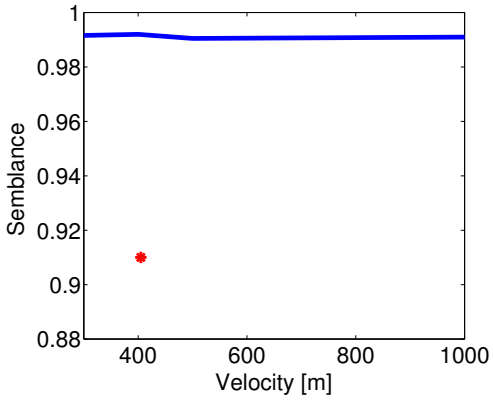

Figure 3.7: *The semblance, calculated for one target event, but after predicting and removing scattered energy using increasing surface wave velocities (from 300 to 1000 m/s). The semblance of the original target event is denoted by the dot.*

scattering) is denoted by the star in this Figure.

We can conclude that for removing the *interference* caused by the scattered surface wave, the method is not very sensitive to the surface wave velocity. In practice however, care should be taken to suppress the remaining parts of the surface wave with linear move-out after application of our method. This can be done by standard techniques, like wavenumber-frequency domain (dip) filtering (Yilmaz, 2001, for example).

3.1.5 Conclusion from Tests on Synthetic Data

In general, we can conclude that the we have obtained a robust algorithm and that the results of this sensitivity analysis justify the assumptions we made about near-receiver scattering. It should be noted that the impedance distribution we obtain from the inversion is not necessarily the true impedance distribution, but one that can accurately explain the observed data with our model of near-receiver scattering. After application of our algorithm, events are more coherent and the original waveforms are restored. Moreover, our method is not sensitive to the surface-wave velocity of the embedding medium. However, with an inaccurate surface wave velocity, part of the surface wave with linear move-out may remain in the result. This is, however, not a serious limitation, because this part can be removed with a mild dip filter.

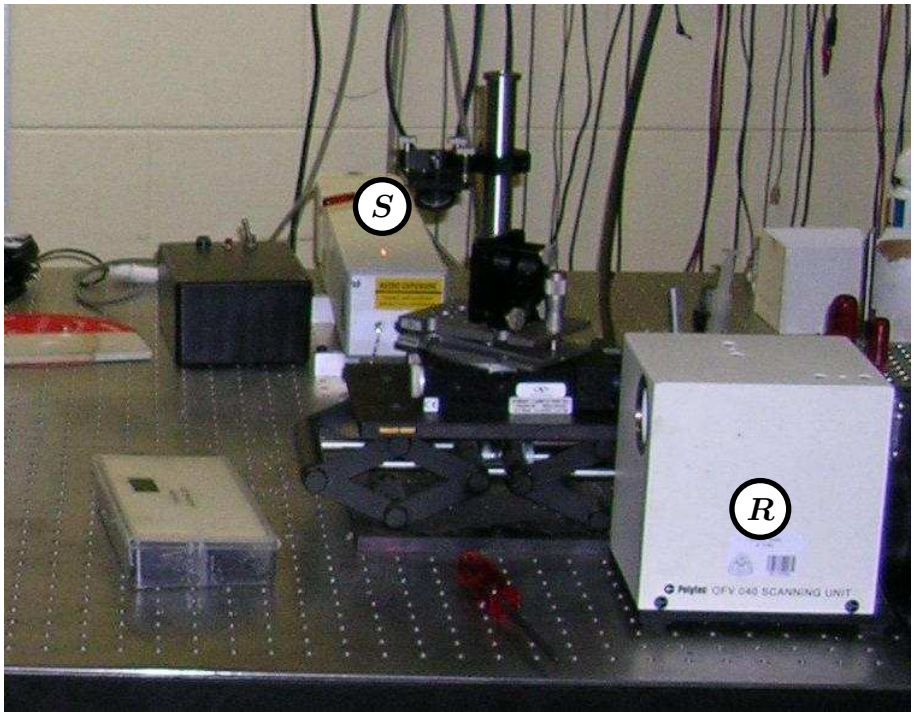

Figure 3.8: *The source laser (S) and the interferometer (R) are mounted to a vibration-free optical bench. The beam from the source laser is redirected and focused through lenses also mounted on this bench.*

3.2 Tests on Laboratory Data

3.2.1 Exciting and Measuring Surface Waves

In this section we briefly describe the instrumentation used in the experiments. These experiments have been carried out in collaboration with the Physical Acoustics Laboratory at the Colorado School of Mines in Golden, Co, US. The entire setup, including the source laser, interferometer and the model to be sampled, is mounted on an optical bench with vibration isolation (see Figure 3.8).

The Laser Source

The source is a pulsed (5 ns) Nd:YAG laser with a wavelength of 1064 nm and an energy of 0.3 J per pulse. Ultrasonic waves are generated by the thermoelastic expansion or ablation depending on the absorbed power and the skin depth of the sample (Scruby and Drain, 1980).

In the thermoelastic regime the effect of the incident laser pulse is a rise in temperature at the spot where the laser hits the Aluminum. This is accompanied by thermal expansion of the Aluminum and this in turn generates a disturbance in the stresses and strains in the material. If more energy is absorbed there will be ablation, but this effect was negligible in our experiments.

The Laser Vibrometer Detector

The wave field is detected by a scanning laser interferometer that measures absolute particle velocity on the surface of the sample via the Doppler shift (Nishizawa et al., 1997; Scales and van Wijk, 1999). The output of the vibrometer-head is a beam of diameter less than 1 mm and a wavelength of 633 nm (red). Once the beam reflects off a moving target, its frequency is Doppler shifted. The beat-frequency of the output plus the reflected signal is decoded in the hardware to give an absolute measurement of particle velocity, without contacting the medium.

The signal of the vibrometer is amplified with a low-noise preamplifier (SR 560 with 12 db/octave 10 kHz high-pass filter) and digitized at 14-bit resolution using a Gage digital oscilloscope card, attached to a PC. The dominant frequency of the measured waves is about 0.6 MHz , while the maximum frequency is limited by the detector electronics.

To ensure high signal-to-noise, thin reflective tape is applied to the model for a strong reflectivity of the interferometer beam. While stacking (averaging) of multiple shots improves data quality, experience tells us that higher levels of noise are mostly caused by a decrease in reflection strength of the interferometer beam. In practice, this often means that there is either an air-bubble between tape and the model, or the reflection strength of the tape is diminished by dirt.

3.2.2 Description of Experiment I

In the first experiment, we consider scattering of surface waves only, to insure maximum control over the scattering process. We focused the laser beam on a line to simulate a line source. This source generates surface waves that are scattered by a cavity with a diameter of 2 mm and a depth of 3 mm, which is roughly the size of the dominant wavelength. Traces are recorded at 0.25 mm intervals, which implies about 10 samples per wavelength.

Figure 3.9a is a picture of the experimental configuration, while Figure 3.9b illustrates a schematic top view of experiment I. Figure 3.10 shows four snapshots (constant time cross sections) of the wave field passing through the cavity for increasing times. The wave is traveling from left to right, clearly showing the circularly expanding scattered surface wave, excited when it hits the cavity (Figures 3.10b-3.10d).

The dense sampling on an areal grid allows for dynamic data visualization, by watching the wave field as a function of time (Scales and Malcolm, 2003, e.g.). A movie of the experiment, showing many constant time cross sections for increasing time, can be downloaded from http://acoustics.mines.edu/research.

We have designed the experiment in such a way that events do not interfere so that they can

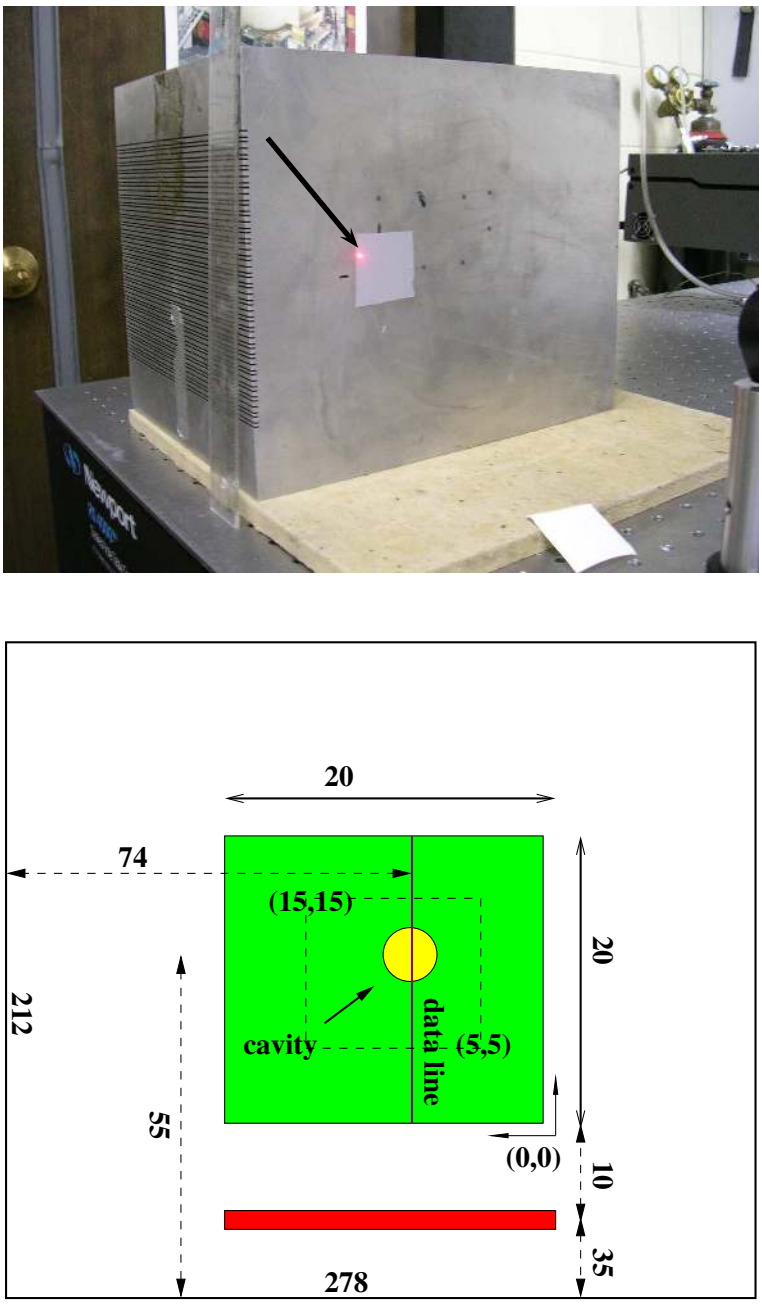

Figure 3.9: *(a) Picture of the Aluminum block. The bright dot (indicated by the arrow) on the reflecting tape is the beam from the interferometer. The source laser is not active. The face of the block in this picture was used for a similar experiment as our experiment I. (b) Schematic top view of the Aluminum block with cavity. The shaded area is the area covered by the receivers (in the examples we use subsets of these data, not exactly centered around the cavity). For this experiment, we focused the source-laser beam on a line (indicated by the dark shaded line). The width of this focused beam is 0.5 mm. Dimensions in the Figure are given in mm.*

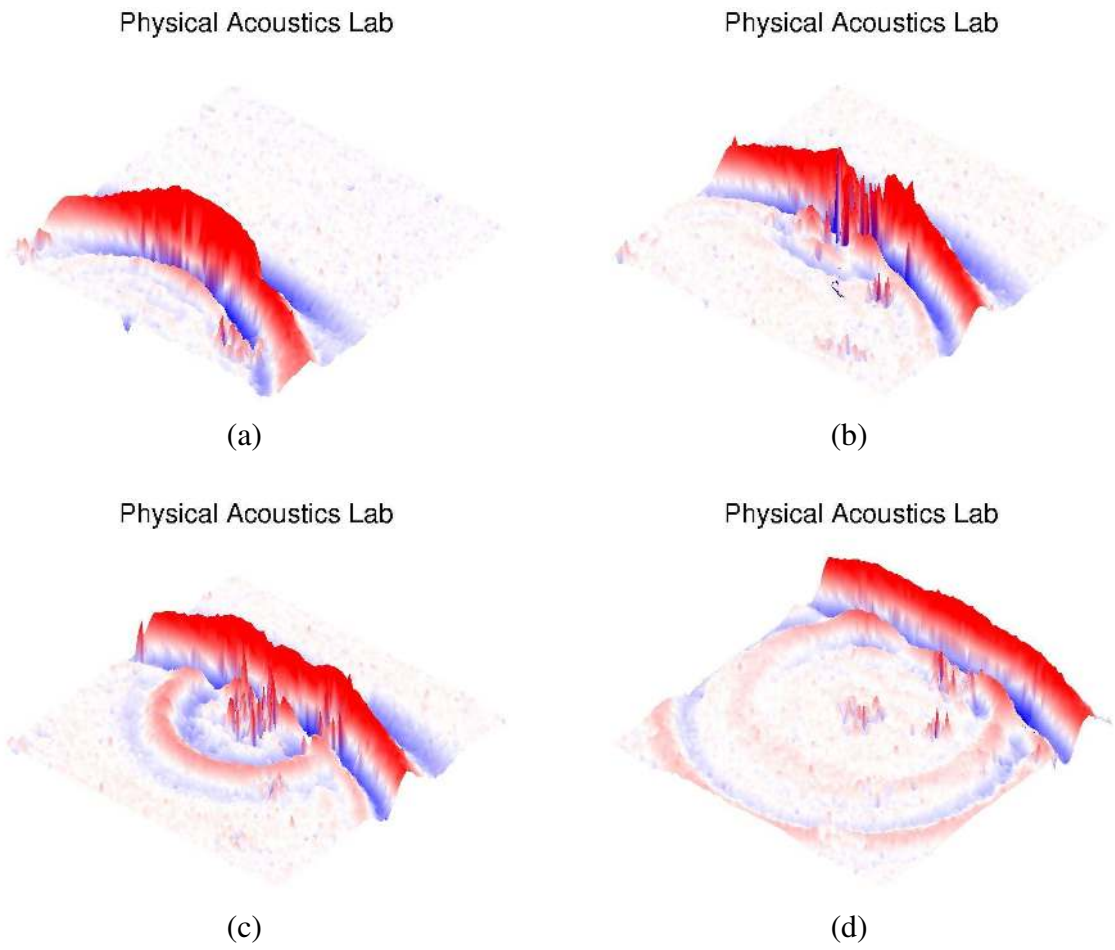

Figure 3.10: *Snapshots (time-slices) of the wave field measured at the surface of the Aluminum block. Time increases from (a) to (d).*

be easily separated by time windowing. This can be verified in Figure 3.11, which shows an inline seismogram of the vertical velocity measured at the surface of the Aluminum block. The various events are labeled as follows: R is the direct Rayleigh wave, C is the Rayleigh wave reflected off the cavity, P is the direct P-wave, G is the 'ghost' Rayleigh wave reflected off the edge of the Aluminum block behind the source, A is an air wave, generated by the thermal expansion as the laser hits the Aluminum, and finally, F is the Rayleigh wave reflected off the far end of the Aluminum block. The presence of the cavity is clear from the repeated diffraction patterns between about 9 and 13 mm, on P, R, G and F. They are indicated by the arrows and labeled S in the Figure. The airwave (A) is unaffected by the cavity, because it travels *over* the surface.

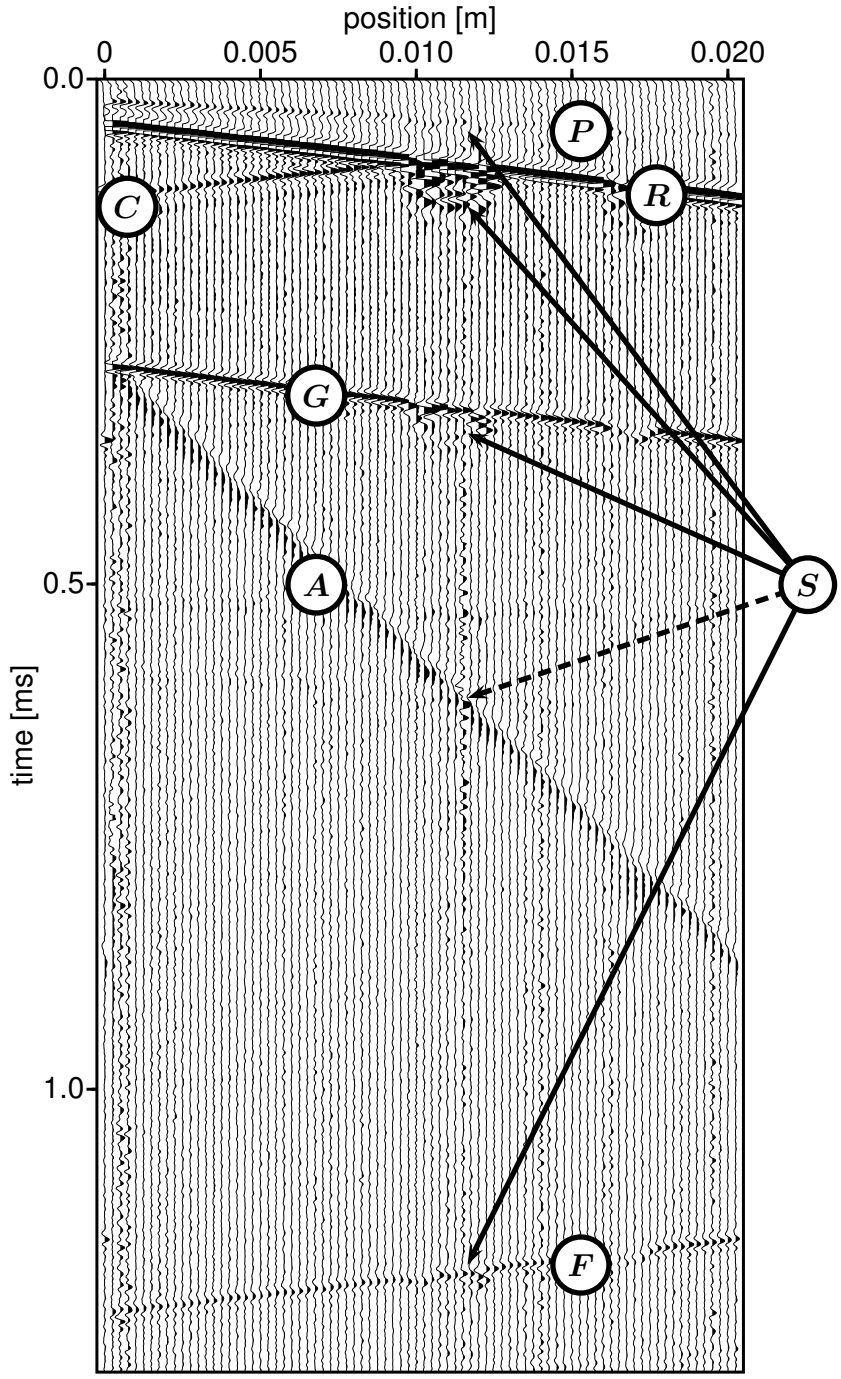

Figure 3.11: *Inline seismogram of the vertical velocity component measured on the surface of the Aluminum block. Events are labeled with letters and are explained in the text. All through the seismogram, the presence of the cavity can be seen between about 9 and 13 mm.*

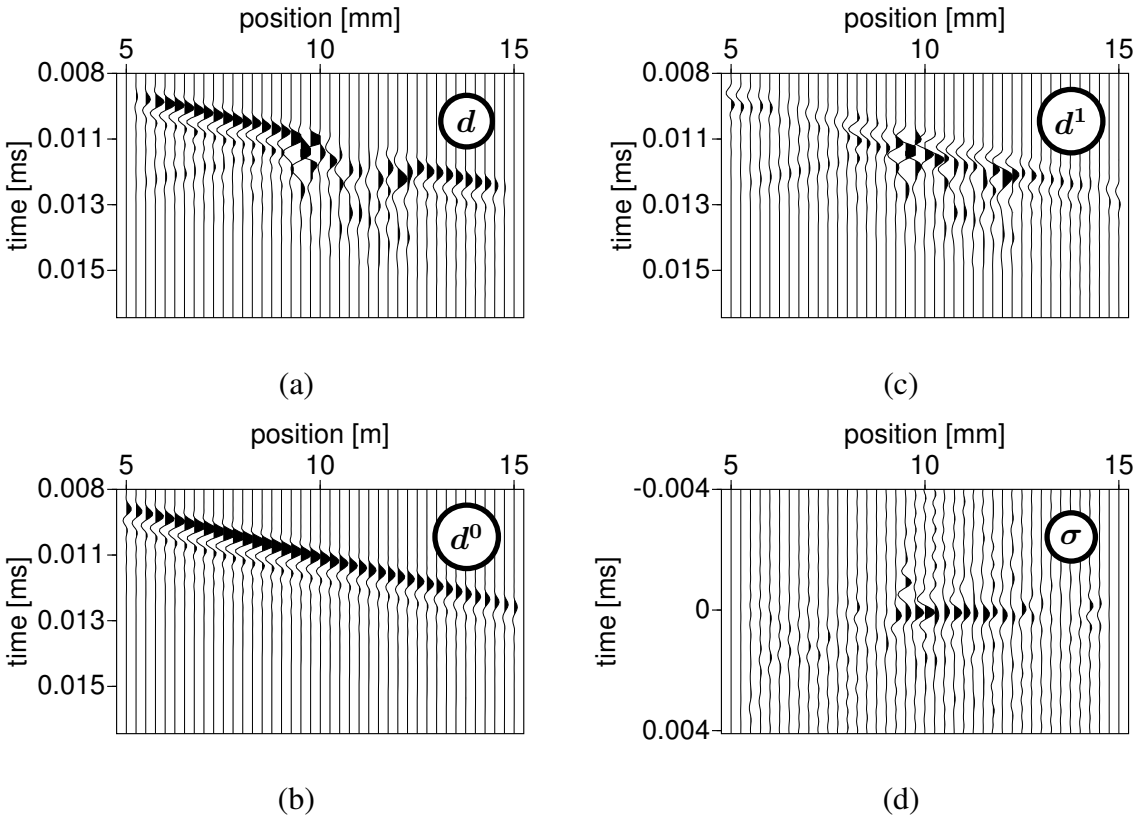

Figure 3.12: *(a) Part of the direct Rayleigh wave (event d in the text). This event is used to derive the scattered energy d^1. (b) The estimated field in the embedding medium (d^0, i.e. if there were no cavity) using a wavenumber-frequency domain filter. (c) Separated scattered energy, d^1. This is the difference between (a) and (b) (cf Eq. (3.3)). (d) Image of the cavity along the same line. Note the improved focusing compared to the scattered field in (c).*

3.2.3 Results from Experiment I

Wave-Field Separation

We now follow the procedure outlined in Section 2.3. To this end, we first select the reference event, d, by time windowing: in this case the direct Rayleigh wave together with the energy scattered by the cavity (displayed in Figure 3.12a). The data consist of 81 by 81 receivers, but in the figure a portion of one seismic line (41 receivers) above the cavity is shown. This line is also indicated in Figure 3.9b as the solid line labeled 'data line'.

To estimate the energy scattered by the cavity, we first estimate the incident wave d^0, using the fact that the incoming wave can be approximated by a plane wave in the measurement area.

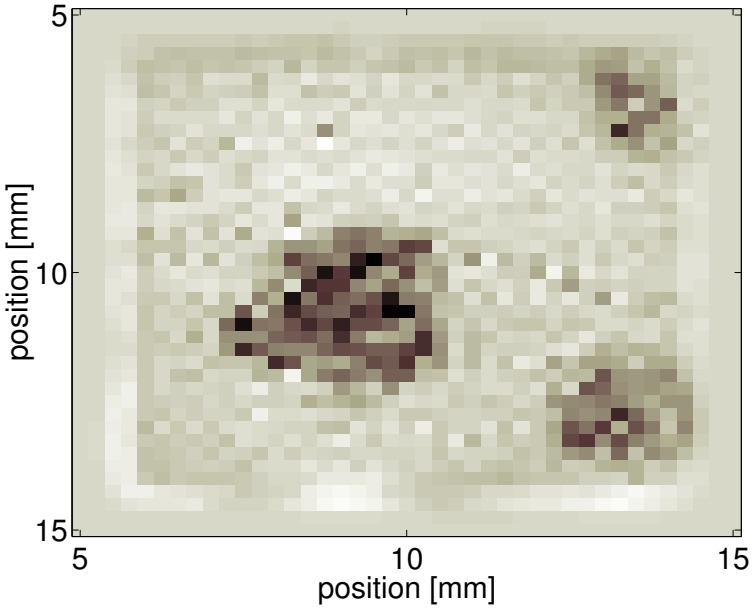

Figure 3.13: *Cross section of the image at $t = 0$ for the first experiment, showing the correct position and size of the cavity. The two dark-shaded dots in the upper and lower right corners are due to scattering from surface disturbances, smaller than the cavity. The darker shades indicate higher amplitudes.*

It is well known that for each frequency, a two-dimensional spatial Fourier transformation maps a plane wave to a point in the wavenumber-frequency domain (Yilmaz, 2001). We use this property to separate the incoming plane wave from its local perturbations. The estimated incident wave is shown in Figure 3.12(b). This filtering operation is further explained in Appendix E.

Subtracting the incident wave d^0 from the reference event d (see also Equation (2.30)),

$$d(\mathbf{x}, t) - \beta d^0(\mathbf{x}, t) = d^1(\mathbf{x}, t), \tag{3.3}$$

we obtain the scattered field d^1. Here, $\beta = 1.12$, due to the fact that we used a very narrow window to estimate d^0. The scattered field is shown in Figure 3.12c. This is the wave field attributed to the presence of the cavity. Clearly, it is an *estimate* of the true scattered field, limited by our separation method, as is evident from the leakage of some coherent energy in the separated scattered field of Figure 3.12(c), other than the wave reflected off the cavity.

Imaging

Next, we estimate the impedance function using (Equation (2.33)):

$$F = \frac{\Sigma||d^1 - \mathcal{K}^d\sigma||^2}{\Sigma||d^1||^2} + \lambda||\sigma||^2. \tag{3.4}$$

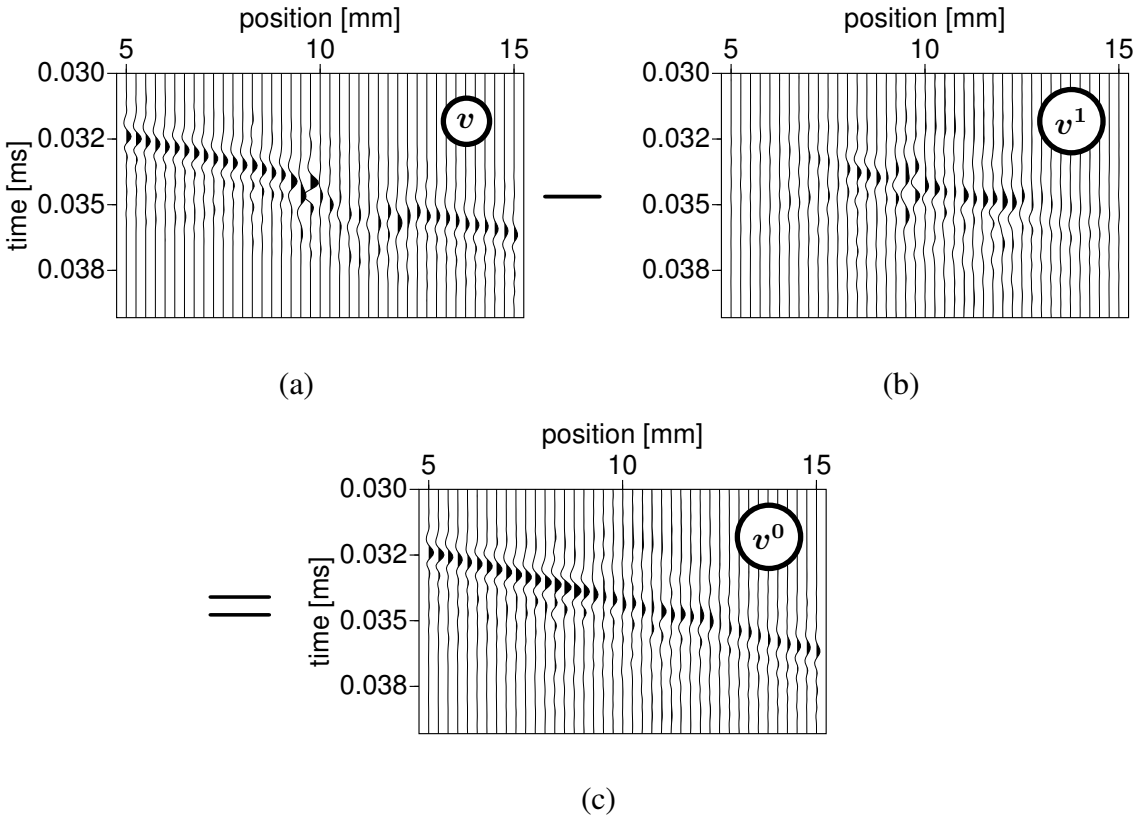

Figure 3.14: *(a) The ghost Rayleigh wave. (b) The predicted scattered field for this event. (c) The ghost Rayleigh wave after removing the predicted near-surface scattered field.*

Because there is only one source position, the index $J = 1$. For simplicity we have omitted this index here. The calculation of the operators requires an estimate of the surface wave velocity, to be able to calculate the Green's function. For a more detailed account of the calculation of the operators, see Appendix D. From the data, we estimate that $c_R \approx 3000$ ms^{-1}, which agrees closely with the observed Rayleigh-wave speed in Aluminum in Scales and van Wijk (1999).

The estimated scattered field d^1 serves as the input for the inverse scattering algorithm as outlined in Section 2.2.2. The impedance function for this in-line data set, obtained after minimizing Equation (3.4), is shown in Figure 3.12d. In this Figure, we observe that the energy is localized in time around $t = 0$ which indicates that the scatterer is indeed at the surface and the scattered energy is spatially focused at the actual location of the cavity.

A top view of the image at $t = 0$ is shown in Figure 3.13. The circular shape of the impedance function slightly to the left from the center, represents the actual shape and location of the cavity (we used a subset of the data, not centered exactly around the cavity – as shown in

the top view of the measurement setup). Anomalies in the right corners of the Figure are due to scattering from smaller surface disturbances.

Prediction and Subtraction

With this estimate of the spatial impedance function from the direct Rayleigh wave, we can calculate the scattered wave field v^1 for a different event, using the following representation (Equation (2.27)):

$$v^1(\mathbf{x}_L, 0) = \int_\Sigma u^G(\mathbf{x}_L - \mathbf{x}'_L, z^{(0)})\sigma(\mathbf{x}'_L, z^{(0)})v^{meas}(\mathbf{x}'_L, 0)\mathrm{d}A \tag{3.5}$$

For the event v^{meas}, we select the Rayleigh wave that is reflected by the end of the Aluminum block behind the source (the "ghost", shown in Figure 3.14a). Note that v^{meas} has not been used for determining the impedance function, and therefore prediction of the scattered field v^1 is a good validation test of the method. The predicted scattered field using Equation (3.5) and the independently estimated impedance function σ, is shown is in Figure 3.14b.

Finally, we obtain the wave field minus the scattered energy from equation (3.3), shown in Figure 3.14c. We observe that the scattering has been effectively removed and that the continuity of the event has increased.

3.2.4 Description of Experiment II

In the second experiment, we consider scattering of upcoming body waves by near-surface heterogeneities. The body waves are excited by a point source at the bottom of a two-layered model, consisting of an Aluminum layer, topped by a Lucite layer, in which we drilled a 2-mm wide and 3-mm deep cavity. When the body waves reach the surface, energy is scattered by the cavity. We record the wave field in a 4-cm^2 region, at 0.1-mm intervals. A top view of this model is shown in Figure 3.15a.

Compared to the data from Experiment 1, these data are further complicated by the fact that they contain multiples from the layer boundary and reflections from the sides of the model as depicted in the side view (Figure 3.15b). Data above the cavity (Figure 3.15c) show the multiples between the layers and reflections from the sides all being scattered by the cavity.

3.2.5 Results from Experiment II

Preprocessing

Due to the fact that the source is at the bottom of the model and the body waves are only partly transmitted through the Aluminum - Lucite interface, the received signal is much weaker than in the first experiment. For this reason, these data required some preprocessing, consisting of tapering-off low frequencies (including a dc-component) and then applying a short spatial convolution filter, to increase signal-to noise. Here, the spatial sampling is dense and the convo-

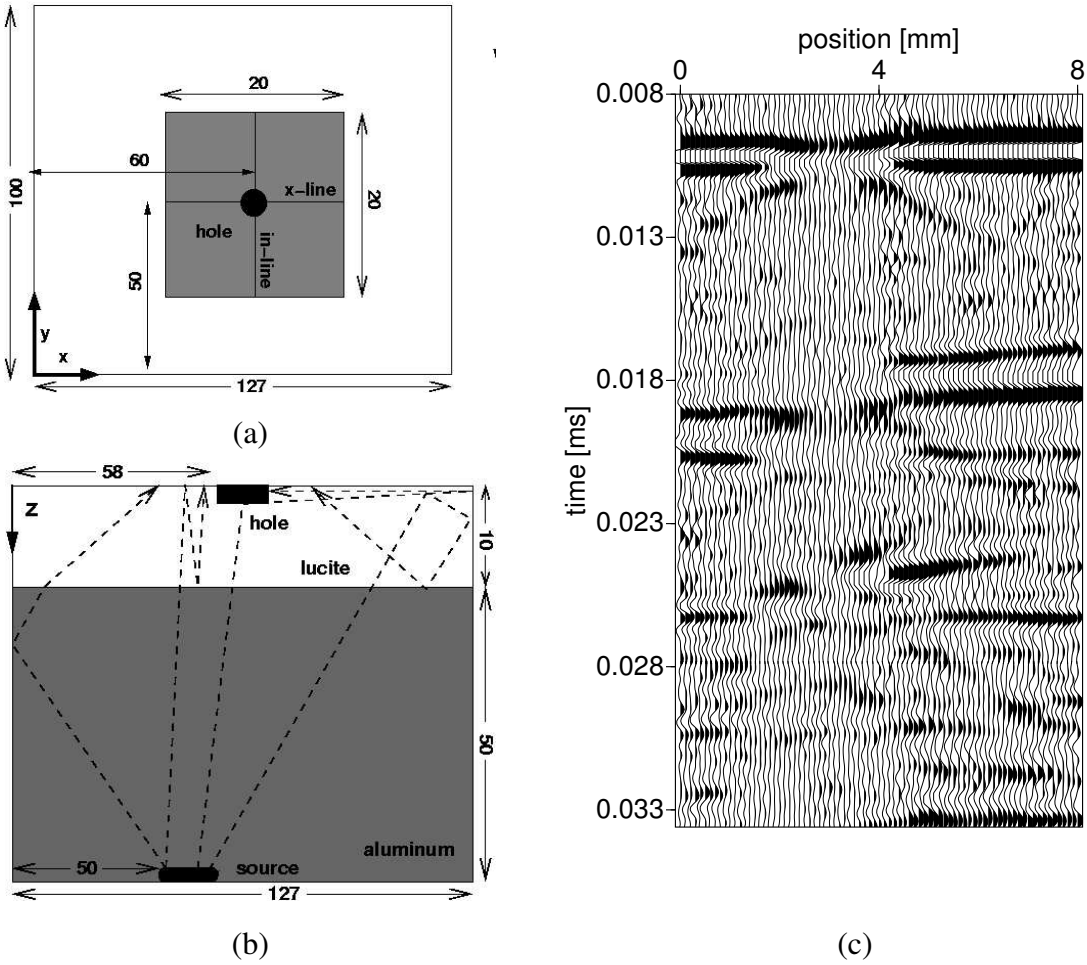

Figure 3.15: *(a) Top- and (b) side view of the two-layered model with cavity. All dimensions are given in mm. (c) Seismogram of part of the data through the cavity.*

lution filter is only 3 traces in each of two perpendicular directions, so that it is not comparable to array-forming and it does not significantly affect the results of our method.

Wave-Field Separation

Apart from the preprocessing of these data, the algorithm is applied in the same way as in Experiment I. Again, we start by selecting a reference event. In this case, we select the first upcoming $P-$wave event, shown in Figure 3.16a. We separate the incident wave (d^0) from the energy scattered by the cavity (d^1), using a narrow wavenumber-frequency domain filter. In this case, we are aided by the fact that the first upcoming P-wave is approximately a vertically incident plane wave. Therefore, most of the energy of the incident wave without scattering should be

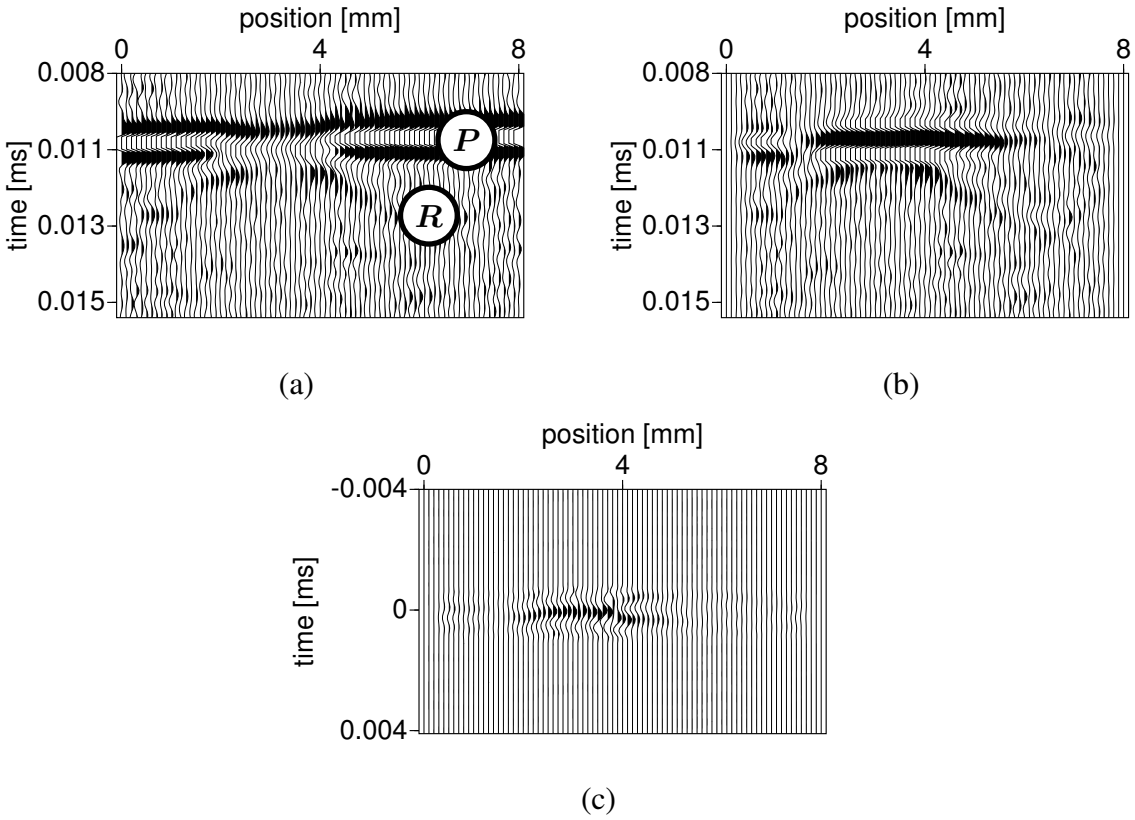

Figure 3.16: *(a) The first upcoming $P-$wave is denoted by P, while the scattered Rayleigh wave is denoted by R. Together they form the reference event (d in the text) used to derive the scattered energy. (b) Separated scattered energy, d^1, using a narrow wavenumber-frequency domain filter. Observe that some coherent energy is not removed by the wavenumber-frequency domain filter, between 0.5 and 1 cm around 0.011 ms. (c) Image of the cavity along the same receiver line.*

concentrated around $k_x, k_y = 0$. This makes the filtering operation particularly straightforward.

We estimate the surface-wave velocity ($c_R \approx 1000$ m/s) from the data shown in Figure 3.16a. The surface wave excited by the upcoming $P-$wave and scattered by the cavity is clearly visible in these data as the 'tails' with linear move-out, following the first arrival (labeled R in the Figure). The separated scattered field d^1 is shown in Figure 3.16b.

Imaging

Using the surface-wave velocity $c_R = 1000$ m/s, we estimate the impedance function depicted in Figure 3.16c. Here, we have windowed the impedance function in the time domain, such that

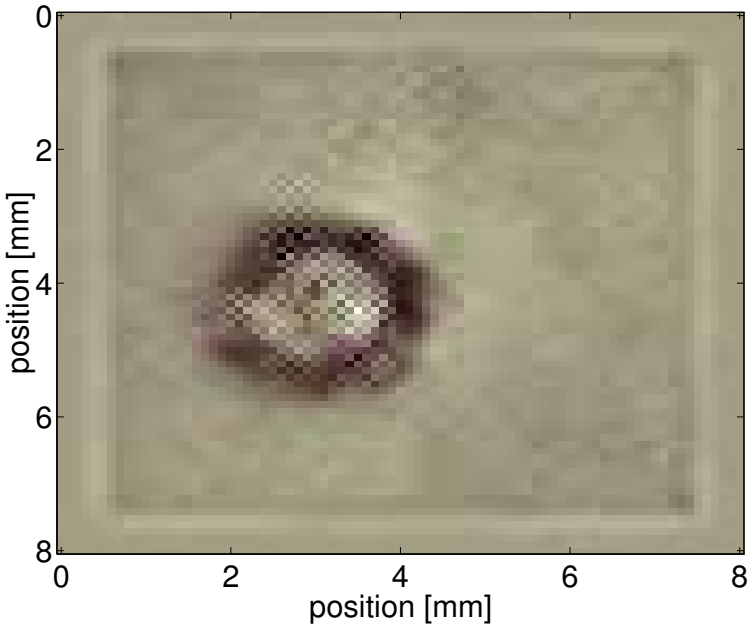

Figure 3.17: *Cross section of the image at $t = 0$ for the second experiment, showing the correct position and size of the cavity.*

the length of the filter is about a period of the dominant wavelength of the event. This is done to reduce "ringing" in the predicted scattered field due to the fact that some frequencies may be dominant in the image. Some incident energy has leaked into the scattered field of Figure 3.16b. Figure 3.17 is a top view of the image at the surface at $t = 0$. The dimensions and location of the image are in agreement with the actual location and shape of the cavity.

Prediction and Subtraction

Finally, we predict the near-surface scattered field in the rest of the data. Depicted in Figure 3.18a is part of the data on a line above the cavity. The data shown in this Figure were not used to derive the impedance function.

Our method is, in some way, sensitive to the velocity of the surface wave, because, as we subtract the modeled scattered waves, a small error in the surface wave velocity may even cause *constructive* interference with the surface waves in the actual data. The same holds true for velocity variations due to dispersion. For this reason, the desired result may contain residual tails from surface waves, but these can be removed by dip filtering. To remove the apexes of the scattering, we have found that an accurate velocity is less important (see also the discussion in Section 3.1.4). So, in order to make a comparison between the data before and after applying the algorithm, we use a dip filter on the input data, as well as on the data after removal of the

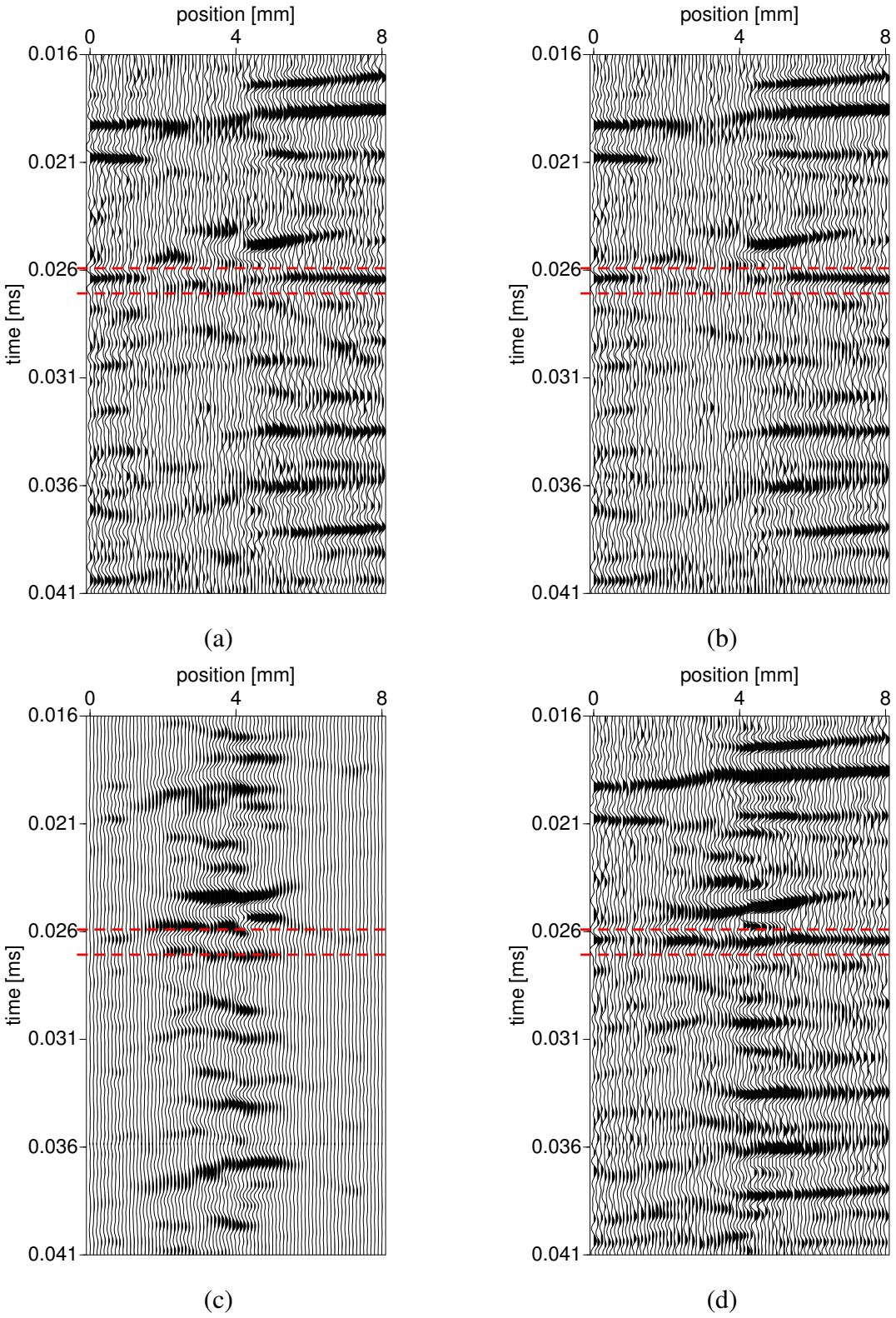

Figure 3.18: *(a) Part of the data following the first P-wave (v in the text). (b) Same as (a) but after a mild dip-filter only. (c) Predicted near-surface scattered field for these data. (d) Same as (a) but after subtracting the predicted scattered field in (c), followed by the same dip filter as in (b). The dashed lines indicate a time window placed around the event at 0.027 ms to calculate the semblance in order to compare this event before and after application of our method.*

scattered surface waves.

The filtered input data are shown in Figure 3.18b. Obviously, the dip filter only removed the flanks of the surface waves, but not the apexes, which have higher apparent velocities and were therefore unaffected by the filter. Especially this part of the surface waves is important to remove, because it is the interference between surface wave scattering and the incident field that diminishes the quality of the target reflection.

Figure 3.18c shows the predicted scattered field excited by the events in Figure 3.18a, calculated using the impedance function shown in Figure 3.16c. This figure shows that we have mainly predicted the part of the scattered waves that cause the strong interference between 3 and 5 mm. The output v^0 after subtracting this predicted scattered field, followed by *the same* dip-filter is shown in Figure 3.18c. When we compare Figure 3.18b to Figure 3.18d, we can conclude that the algorithm has improved the continuity of the reflectors by reducing the interference of the scattered waves.

To quantify this improvement, we again calculate the semblance (see Section 3.1.3). To this end, we select a window of 5 ns around the event at about 0.027 ms (this window is roughly indicated with the dashed lines in Figure 3.18a-d). The semblance of the raw event is $S = 0.2861$. After applying the dip filter only, the semblance is $S = 0.3825$. After applying our algorithm, the semblance of the same event is $S = 0.5769$, which demonstrates that the coherency among the traces has improved.

4

Field-Data Examples

In Chapter 3, we applied our method to data from two laboratory models. In these models, we chose the parameters and geometry such that it was relatively easy to precondition the data for our method (as described in Section 2.2.1). Apart from being a further validation of the method, these laboratory tests can be seen as an intermediate step directed to the application of our algorithm to field data.

In the present chapter, we apply our prediction-and-subtraction algorithm to two field data sets containing significant near-receiver scattering. These tests on field data serve to show the applicability of our method to exploration seismic problems and to further investigate the limits of the method.

Anticipating further developments in seismic data acquisition, we have designed our method for 3-D densely sampled data, despite the fact that in current practice these data sets are rare (even so, examples of such data exist Herman and Perkins, 2004; Moldoveanu et al., 2004, for example). However, with a minor adjustment, our algorithm can be readily applied to 2-D data sets as we will show in this chapter.

The first data set has been provided by Schlumberger Cambridge Research and Western/Geco. It was collected at a field experiment in Michigan, US. This data set comprises two densely sampled receiver lines recorded in an area with significant amounts of near-surface scattering. Each trace in these data has been recorded by an individual receiver (thus there has been no group forming).

The second one, from a high-resolution survey in the Saudi Arabian desert, has been provided by Saudi Aramco. In the area where the data were collected, surface topography is present. This has consequences for the preprocessing step in our algorithm. We will place emphasis on this step when we discuss application of our method to these data. The Aramco data also differ from the Schlumberger data in that they have been group formed in the field in the crossline direction to suppress ground roll. The inline direction however, has been densely sampled. The group forming may influence the inversion and modeling part of our algorithm.

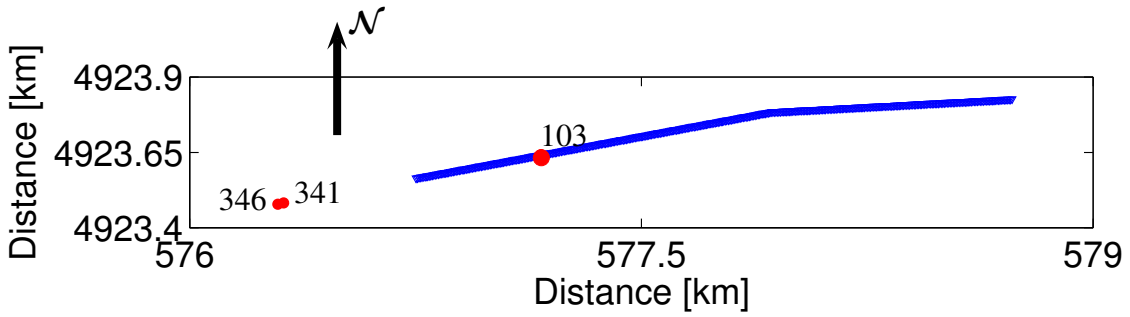

Figure 4.1: *Geometry of the Michigan field experiment. The line represents the receiver line with 401 receivers. The receiver spacing is 5 m, while the shot spacing is 10 m. The dots represent source positions, labeled with their numbers.*

4.1 Michigan Experiment — Schlumberger Data

4.1.1 Geometry

During the summer of 2002, Schlumberger/WesternGeco recorded two lines with 401 multi-component receivers each, in a cross-spread geometry. From these two lines, we have analyzed the vertical component of the velocity of one line running roughly from West to East. The geometry of this line is shown in Figure 4.1. After analyzing these data, we have focused on the data from the shots indicated in this figure in more detail (shot 103, 341 and 346). From these shots, we have selected areas where we have applied our prediction-and-subtraction algorithm.

The receivers were laid out on the line shown in Figure 4.1, without being moved during the survey. The total length of the receiver line is 2000 m. Each shot is recorded by the entire line of 401 receivers with a spacing of 5 m. For the survey, (single) explosive sources with a spacing of 10 m were used. No arrays were formed in the field, so that each trace from this densely sampled data set was stored on tape.

Two typical shot records are shown in Figure 4.2a and b. First, we describe the application of our method to the part of the data in the boxed area of Figure 4.2a. In Figure 4.3, we have zoomed in on this part.

4.1.2 Near-Receiver Scattering

The data shown in Figure 4.2a-b were collected in an area where substantial near-surface scattering is present. The near-surface region consists of a glacial till containing large boulders. Since receiver intervals (or geophone spacings) are small (5 m), we can clearly identify near-

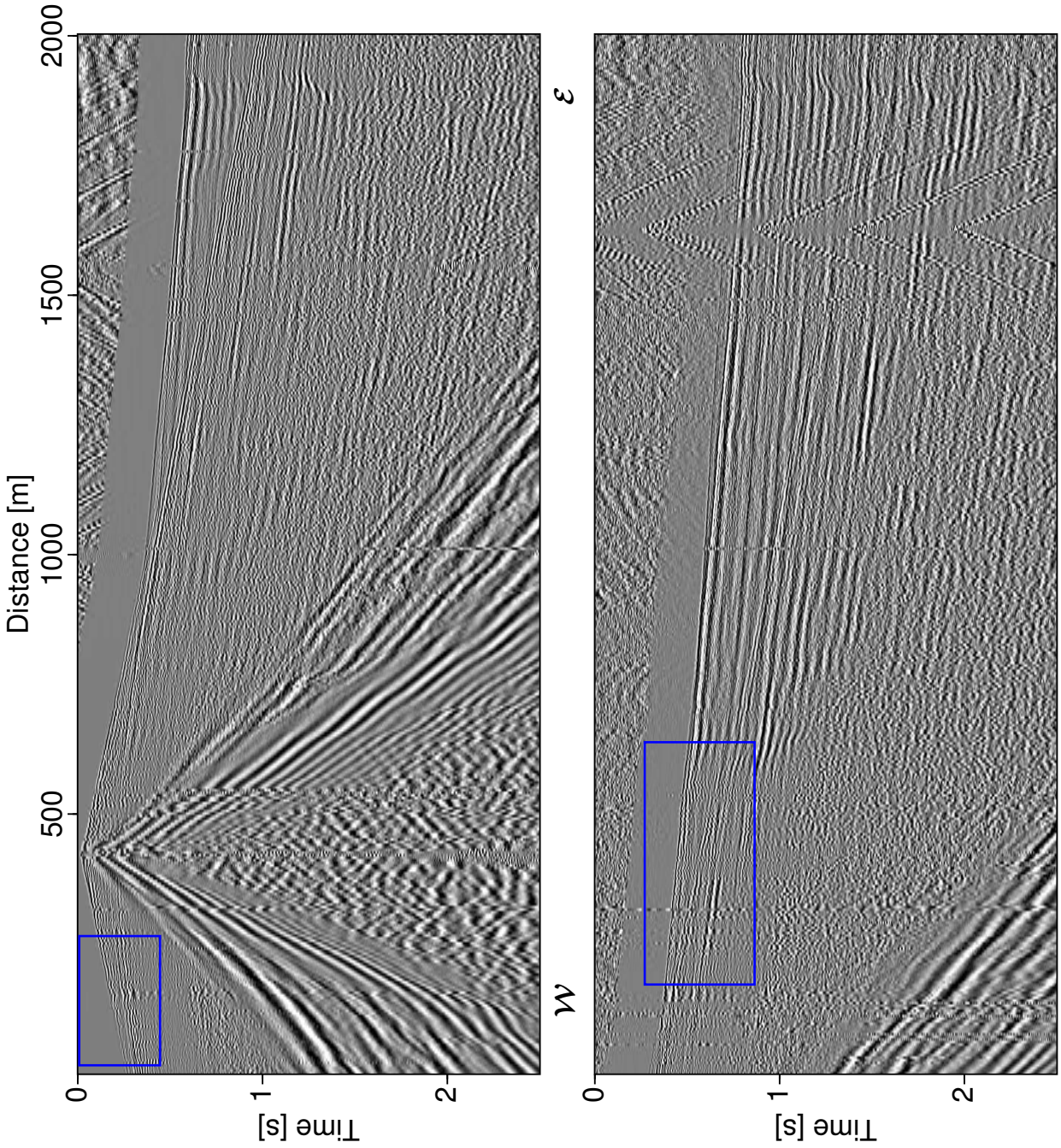

Figure 4.2: *Two typical shots record from the Michigan Experiment. (a) Shot 103 (see Figure (4.1)) and (b) shot 346. We have applied AGC to both shots for display purposes. The distance is measured from the beginning of the receiver line. The near-surface region varies along the line. There are two transitions in ground conditions from West to East. First the ground is wet, then dry sand and at the end of the line the ground is moist.*

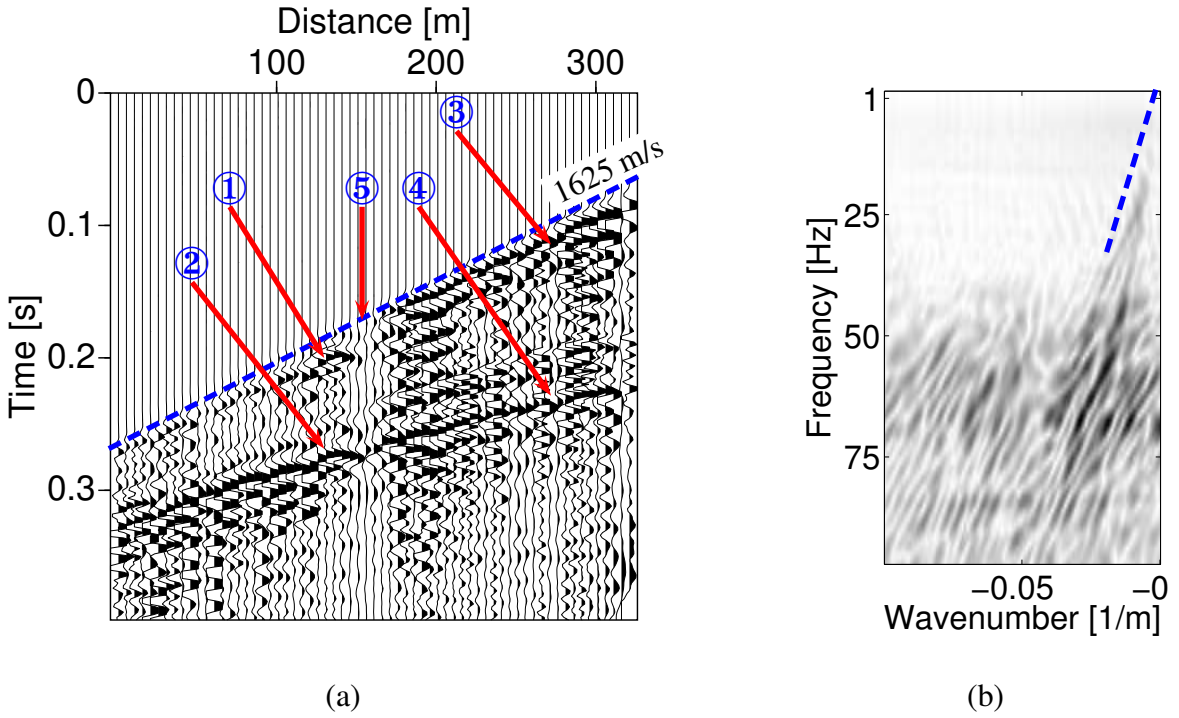

Figure 4.3: *(a) Detail of shot record 103 (corresponding roughly to the boxed area in Figure 4.2a). We clearly observe the effects of the near subsurface on the two events in this display. We can identify diffraction hyperbolas around 125 m and strong interference around 150 m, typical of near-surface scattering. They are indicated by the arrows; the numbers are explained in the text. (b) Wavenumber-frequency domain spectrum of the data displayed in (a). In this domain, we also observe effects introduced by the near subsurface. These are explained in the text.*

surface scattering. Because the near surface varies considerably along the line, we have selected a few areas where the near surface is (hopefully) not changing too much.

In Figure 4.3a we zoom in on the boxed area in Figure 4.2a. The arrows point to some characteristic features of near-surface scattering. We observe diffraction hyperbolas marked with ①, ②, in the figure. We also note parts of diffractions with linear move-out (③,④). Note that the scattering features are consistently repeated in the later (reflection) event. This is typical of near-receiver scattering (or multiplicative noise) because each event passes through the same anomaly close to the receiver (see also Section 1.4). Along the part of the line shown here, there are no significant elevation variations. Around 175 m, a strong discontinuity is present in both the first arriving wave and the reflection (⑤). From looking at the elevations in the headers of the data, this discontinuity has no apparent surface manifestation. This observation leads us to believe that the discontinuity is also caused by near-surface scattering.

Figure 4.3b shows part of the wavenumber-frequency ($k - f$) spectrum of the data shown

in Figure 4.3a. The velocity of the first arriving wave is roughly 1625 ms^{-1} (indicated by the dashed line in Fig 4.3a). Because this wave has linear move-out we should be able to observe a coherent alignment in the $k-f$ spectrum with a slope of about .0007 sm^{-1}. The beginning of this line is indicated with the dashed line in Figure 4.3b.

We observe that due to near-surface perturbations, this event is not a well-defined linear alignment as we would expect to get from a linear arrival in the data. Moreover, we observe that much energy is 'smeared' over the wavenumber-frequency space due to amplitude and arrival time anomalies (Panea et al., 2003). We observe the dipping lines, almost parallel to the dashed line typical of random static effects (Blaquière and Ongkiehong, 2000; Panea et al., 2003). This noise is dispersed throughout the $k-f$ domain and is thus partly localized in the pass band of a dip filter (in the context of the effect of perturbations on linear noise arrivals, this is discussed in Cox, 1999, pp. 311-313). This is the same for the scattering hyperbolas induced by near-surface scattering, as the apex has higher apparent velocities than linear coherent noise.

We have selected this part of the data such that it does not interfere with the strong ground roll visible in Figure 4.2.

4.1.3 Wave-Field Separation

Wave-field separation is part of the preconditioning of the data before inversion as described in Section 2.2.1. To estimate a near-surface impedance function, we require an estimate of the near-surface scattered field. Because we assume that the scattering takes place immediately under the receivers, we can assume that each event passes through the same heterogeneous domain. Consequently, we need only one event to characterize the immediate subsurface. This is the 'reference' event.

In Figure 4.3a, such an event is the first arriving wave. To select this event, we place a time-window around it. In this case we use a constant velocity (from the data we estimate $c \approx 1625$ ms^{-1}):

$$\begin{aligned} t_{min}(x) &= T_0 - x/c - \mu T_w, \\ t_{max}(x) &= T_0 - x/c + (1-\mu) T_w. \end{aligned}$$

Here, x denotes the offset, c the velocity, T_0 the intercept time of this event (in this case about 0.1 s) and T_w is the length of the time window. The window length T_w should be long enough to include scattering coda, but, preferably not too long so that it includes other events. The parameter μ controls the portion of this window to include the reference event and the portion to include scattering following this event so that it does not have to be centered around T_0 (if $\mu = 0.5$, the window is centered around T_0). Defined in this way, $t_{min}(x)$ described the minimum time selected for each trace, while $t_{max}(x)$ describes the maximum time included for each trace. In practice, we also taper the edges of this window to reduce artifacts in further processing.

The next step is to separate the wave field in the embedding from the wave field due to local

perturbations. Because scattering takes place close to the receivers (i.e. in the near field), it interferes with the incident wave. For this reason, careful processing is required. Various methods can be used to separate the local perturbations from this event. For example, in Section 3.2 we use a wavenumber-frequency domain filter for a (approximately) plane incident waves in a medium with a homogeneous near-surface region. For more complicated arrivals, for example in the presence of topography one can use smoothing techniques that afford slow variations in the incident wave field (Gersztenkorn and Scales, 1988, e.g.). In the case where different events interfere, one can use more advanced techniques, for example based on the singular value decomposition, used in vertical seismic profile processing (Mars et al., 1999, e.g.).

From looking at the data we infer that the first arriving wave varies somewhat smoothly. From this observation we presume that the embedding changes slowly. Although we have assumed that the near-surface region in our scattered-noise model is homogeneous, we can allow for some lateral variation as long as we can obtain a reasonable estimate for the wave field in the embedding through preprocessing. To afford such slow variations while separating the faster variations, we have chosen an α-trimmed mean (α-TM) filter (Bednar and Watt, 1984, see also Section E.2). The window length of the α-TM filter offers a handle on the smoothness of the changes that we want to maintain in the incident field.

First, we apply linear move-out correction (LMO) to the reference event to align it horizontally. Then we apply the α-TM filter, as described in Appendix E, Section E.2 to estimate the wave field in the embedding medium. Once we have obtained an estimate of the incident field, we subtract it from the total field in the following way (Equation (2.30)):

$$d^1(\underline{\mathrm{x}}, t) = d(\underline{\mathrm{x}}, t) - \beta d^0(\underline{\mathrm{x}}, t), \tag{4.1}$$

to obtain the near-surface scattered energy d^1 for the reference event. In the subtraction we include a simple scaling factor (β) so that the incident wave is optimally removed from the total field.

This procedure is depicted in Figures 4.4a-c, where the (spatial) window length for the α-TM filter is 11 points and $\alpha = .2$. The reference event is shown in Figure 4.4a, while the estimated incident wave is shown in Figure 4.4b. Finally, the estimated scattered field is shown in Figure 4.4c. Inspection of this figure reveals that most of the smooth event has been removed from the reference event. In particular, note that the apex of the hyperbola around 130 m is unimpaired, which indicates that we chose the filter parameters correctly.

4.1.4 Imaging and Suppressing Near-Surface Scattering

Imaging

Once we have an estimate of the near-surface scattered energy, the next step is to image it. This yields the near-surface impedance function.

The inversion scheme is formulated in terms of minimizing a misfit between the estimated scattered field and a forward-modeled scattered field by iteratively updating the impedance

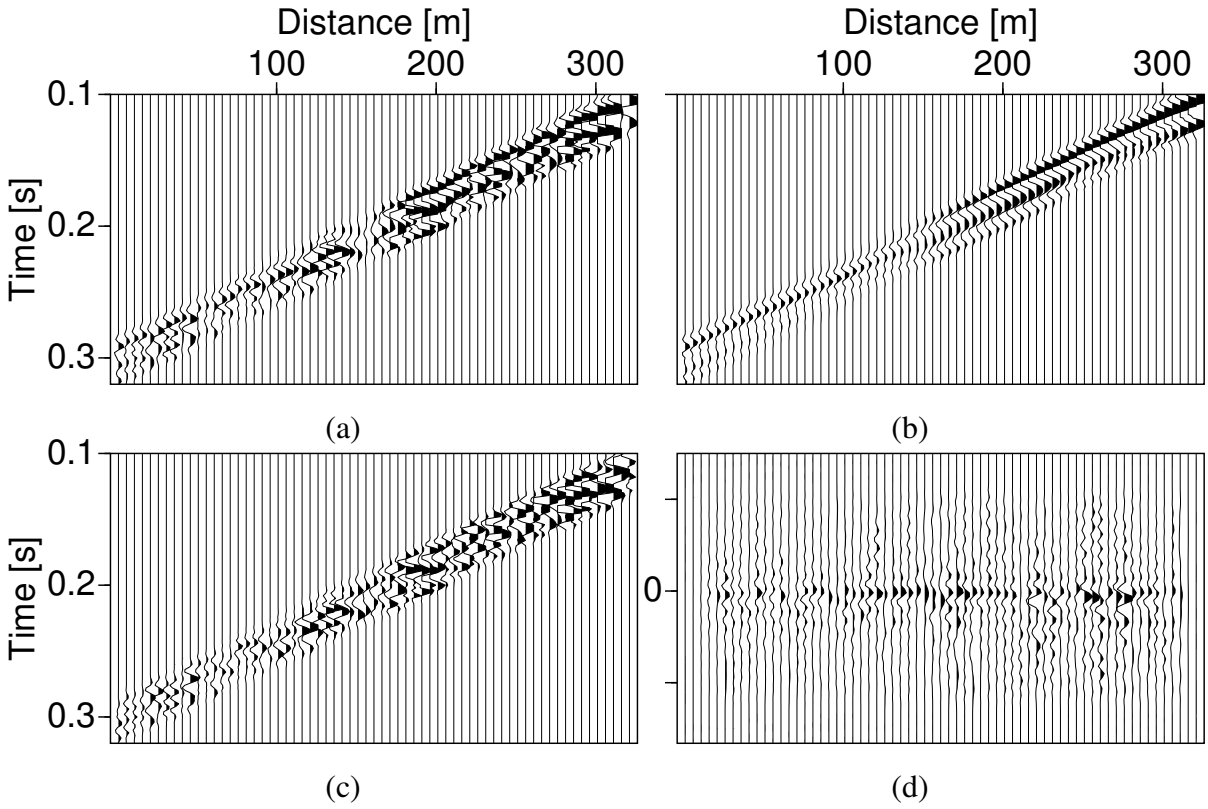

Figure 4.4: *(a) The reference event selected from the detail of shot record 103. (b) Estimate of the incident wave field. This estimate is obtained using the α-TM filter. (c) Estimated near-surface scattered energy. This is the wave field attributed to the presence of local heterogeneity. (d) Near-surface impedance function.*

function as described in Appendix C.

The algorithm has been set up to handle 3-D data, and up to now we have used 3-D data exclusively. However, without major modifications, we can use our algorithm for 2-D data. In fact, because the data were collected along a line, and because we assume that the scattering takes place directly under the receivers, the only modification is that we now constrain the impedance function to lie on the receiver line, instead of in a surface. Apart from this, the entire inversion is carried out in the same way as in the 3-D case.

For the inversion we require a velocity model of the embedding. We use the fundamental mode Rayleigh-wave velocity in this area to characterize the model. We estimate this velocity from the data (see for example Figure 4.2); it is given by $c_R \approx 300$ ms^{-1}. Even though the Rayleigh wave is dispersive, we may use the velocity of the fundamental mode, because our algorithm is not very sensitive to this velocity (see Section 3.1.4).

After minimizing the difference between the modeled scattered field and the scattered field

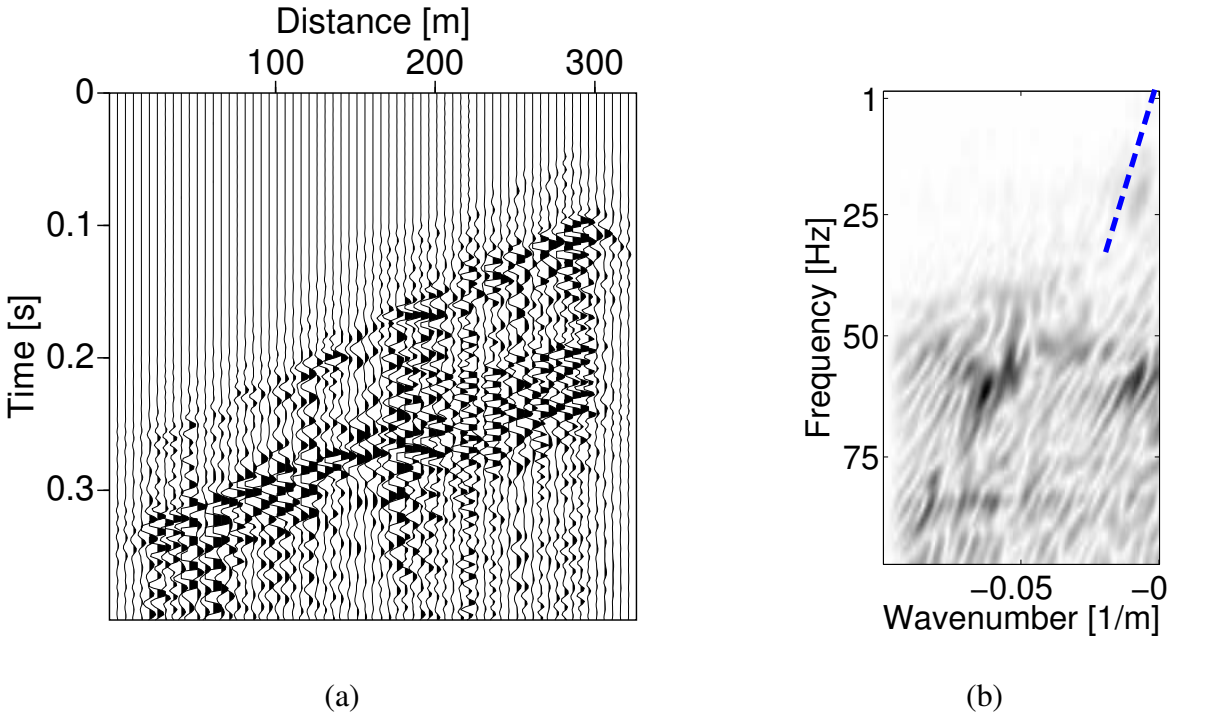

Figure 4.5: *(a) Scattered field predicted with Equation (2.27) and using the impedance function of Figure 4.4d. We observe that we have mainly predicted scattered energy because there is hardly any coherent incident or reflection energy in this prediction. (b) Wavenumber-frequency domain spectrum of the predicted scattered field.*

obtained from the reference event using the algorithm outlined in Appendix 2.2.2, we obtain the impedance function shown in Figure 4.4d. The scattered energy has been focused around $t = 0$, which indicates that the scattering takes place close to the surface.

Predicting and Subtracting Near-Receiver Scattered Waves

With this estimate of the impedance function, we calculate the scattered field on the data shown in Figure 4.3a, using Equation (2.27). This predicted scattered field is shown in Figure 4.5a. From inspecting these predicted data we conclude that we have not modeled coherent incident or reflection events, but only the part of the wave field that we attribute to the presence of near-surface heterogeneity. From this observation we conclude that our scattering model (Equation (2.27)) effectively discriminates near-surface scattering from reflection events.

This can also be observed in Figure 4.5b, which shows the $k - f$ representation of the predicted data (the gray scales of Figure 4.3b and 4.5b are the same). The dashed line shows the start of the expected linear alignment of coherent energy from the first arriving wave.

Finally, we show the data after subtracting the predicted scattered energy in Figure 4.6.

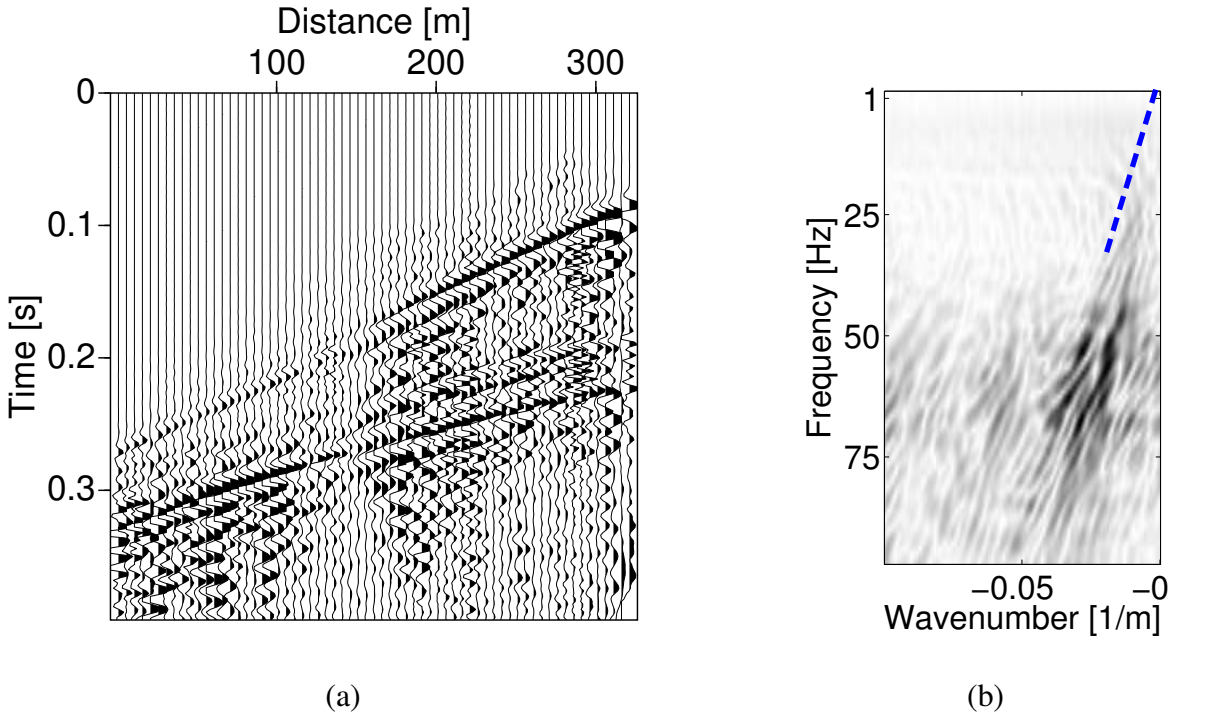

Figure 4.6: *(a) Detail of the shot record after predicting and subtracting the near-receiver scattered waves. It corresponds to the difference of Figure 4.3a and Figure 4.5a. (b) The clean data in the $k - f$ domain.*

This figure demonstrates that we have removed most of the interference caused by scattering. However, there are some remnants of coherent energy with the steeper dips. This energy is most probably introduced by the ringing in the impedance function, because they appear to have a strong dominant frequency.

As a quick way of quality control, we can compare the estimate of the incident field from the reference event (Figure 4.4b) with the same event in Figure 4.6a. A quick glance at both figures confirms that they resemble quite well. The difference is due to the fact that we allow a small residual after the minimization, because our scattering model does not explain all the energy separated from the reference event, as it also includes incoherent noise for example.

In Figure 4.7a, we show the input data after applying a dip filter to remove that part of the scattering that has lower apparent velocities than those in the area between the dashed line and the vertical axes. From this figure it is clear that the apexes (i.e., part of the scattered waves with higher apparent velocities) and the interference are left unaffected by the dip filter.

After modeling and subtracting the scattered field on the record in Figure 4.2a, we obtain the desired output shown in Figure 4.7b followed by *the same* dip filter. This is an estimate of the record that would have been measured without near-receiver scattering.

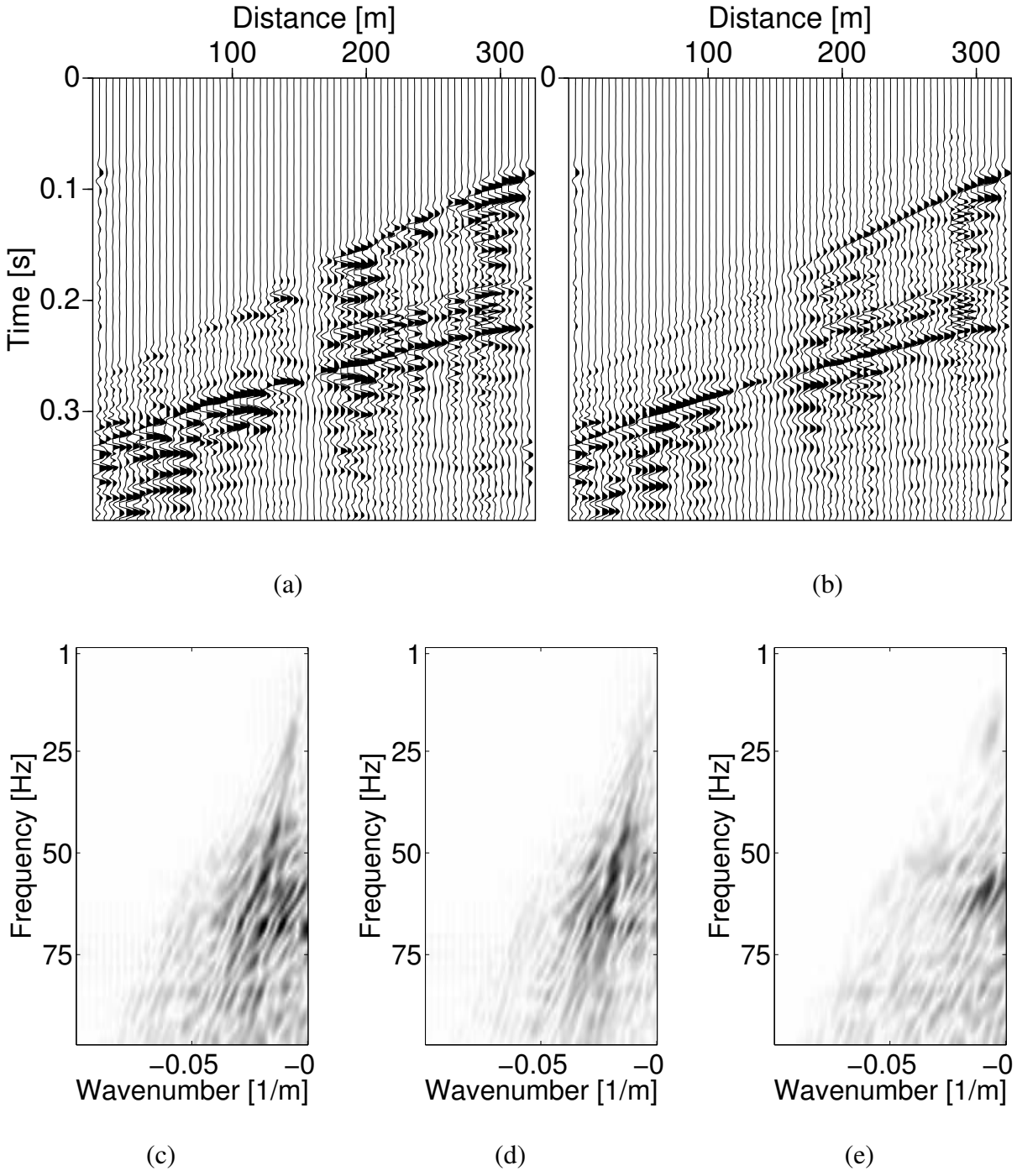

Figure 4.7: *(a) Detail of the shot record after applying a $k-f$ filter to remove part of the record with lower apparent velocities. (b) Same detail, but after predicting and subtracting scattered waves followed by the same dip filter. Observe that we have successfully removed most of the interference. (c) Wavenumber-frequency domain spectrum of the data shown in (a). Note that the dip filter removed the part with lower apparent velocities (compare with Figure 4.3b). (d) Wavenumber-frequency domain spectrum of the the data shown in (b). (e) Difference between (c) and (d). This is the $k-f$ spectrum of the noise that is passed by the dip filter, but is removed by our method.*

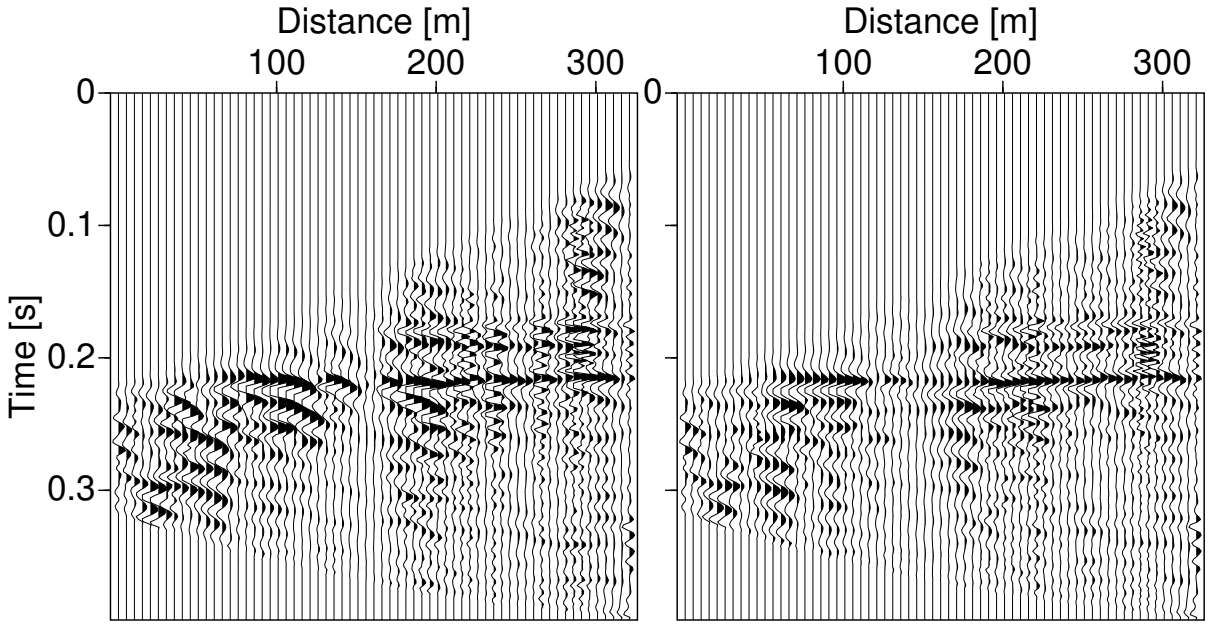

Figure 4.8: *(a) Same as Figure 4.7a, but after normal move-out correction. (d) Same as Figure 4.7(b), but after normal move-out correction. This figure emphasizes the visual improvement obtained for the second event in these data.*

Figure 4.7c depicts the $k - f$ spectrum of the data shown in Figure 4.7a. This figure shows that the dip filter removed the the part of the data with lower apparent velocities, while it passed all energy in a cone around the vertical (only half of this cone is shown in this figure because the events all dip in negative direction). Figure 4.7d shows the spectrum of the data in Figure 4.7b. The difference of these spectra is shown in Figure 4.7e. This figure shows the $k - f$ spectrum of the noise that is passed by the dip filter, but is removed by our method. This figure illustrates how our method complements the well-known dip filter.

4.1.5 Continuity and Coherency

Cox (1999, p.(p.) 451 f(f)) gives a list of quality control (QC) tools that can be used for residual statics estimations. One of the tools is to look at the continuity and trace-to-trace coherency in a common-midpoint (CMP) gather. Furthermore, Cox (1999, p. 457) notes that residual statics should improve the stack response of a stack made in any record domain. In principle, we should obtain similar results with our method, although we leave smooth variations intact as far as they are they are included as a priory information in the estimation of the incidence field

Table 4.1: *Semblance calculated for different events. In these tables, R denotes the raw event after NMO, RD denotes the event after the dip filter followed by NMO, C denotes the event after subtracting the predicted scattered energy followed by NMO and CD denotes the event after prediction and subtraction, followed by a dip filter and NMO. The window for the calculation of the semblance is centered around time sample k and is about the length of one cycle of the waveform. The traces included run from m_1 to m_2, so that $M = m_2 - m_1$. In this case we have chosen $k = 115$ which corresponds to $t = 0.23$ s.*

$k = 115, m_1 = 5, m_2 = 60$	
Event	Semblance
R	0.21
RD	0.30
C	0.47
CD	0.63

of a reference event. Hence, we do not expect to get a perfectly aligned shot-gather. However, compared to the initial shot gather, we should see an improvement in continuity due to the fact that we have removed the interference between the upcoming reflection and the scattered waves.

Because we have worked on common-shot records only, we use this for QC. Note, that this stack can include structural components when the near subsurface is complex. However, we assume that this structural component is negligible because we use only a portion of the data which covers a limited part of the line. From Figure 4.7a-b, we see a clear visual improvement of the reflection event after we have applied our method. In Figure 4.8, we have applied NMO to align the reflection event. This emphasizes the improvement in continuity of this event. While it also shows that it has not been flattened completely, the variations are much less rapid than in Figure 4.8a, implying that current statics methods may be expected to be more effective after application of our method.

At the same time, we expect improved trace-to-trace coherency, because the multi-channel filter also corrects for interference that causes amplitude and phase anomalies other than shifts in the arrival times due to the difference in velocity between the scatterer and the embedding medium. This has been discussed in Section 3.1.3. Here, we calculate the semblance of a part of the event shown in Fig 4.8a-b, before and after applying a dip filter and/or our method. We assume that there is no structural component, but, nonetheless, we don not include the farther offsets because the waveforms there are stretched due to the NMO correction. The results of these calculations are summarized in Table 4.1. From this table we conclude that the dip filter increases the coherency moderately, while application of our method (without a dip filter) about doubles the semblance coefficient. Finally, after we applied our method *and* a dip filter the

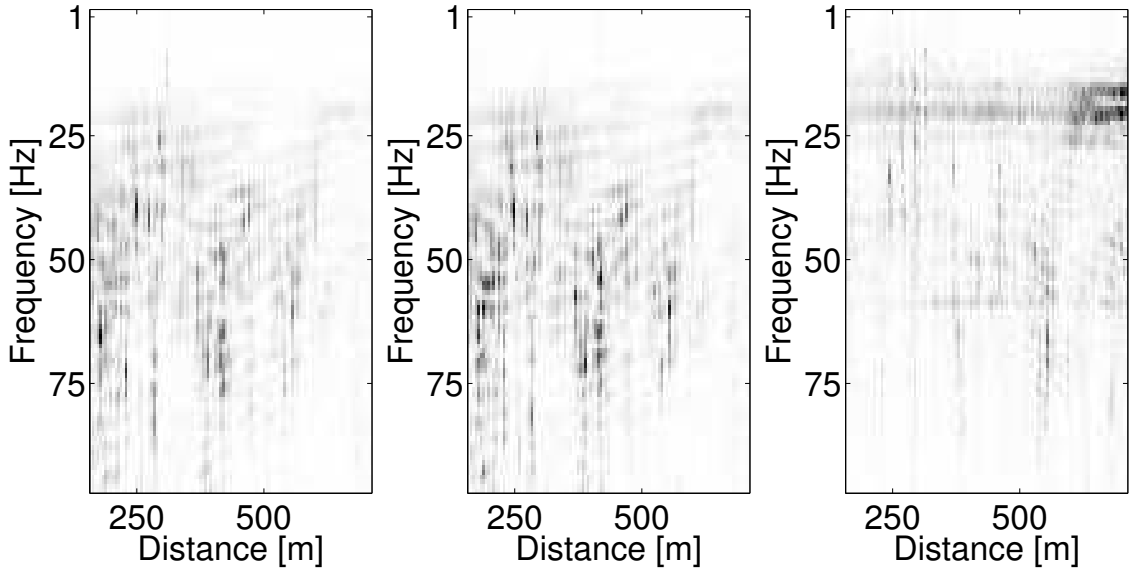

Figure 4.9: *(a) Frequency spectrum of a detail of shot record 341 (the boxed area in Figure 4.2b). (b) Frequency spectrum of the part of shot number 346 covered by the same receivers. This shot is from the area where the ground conditions are similar to those for shot 341. (c) Frequency spectrum of the part of shot 343 covered by the same receivers. This shot is located at the other side of the receiver line, where the ground conditions differ from those of the area of shot 341 and 346.*

semblance coefficient has increased considerably (three times the semblance coefficient of the original event).

4.1.6 Surface Consistency

Practically all near-surface correction methods use the concept of surface consistency. This entails the approximation that ray paths through the overburden are vertical and that the all traces measured at a specific surface location are effected in the same way. Using redundancy of measurements at surface locations, one can use this to obtain statistically inferred corrections.

If one assumes vertical ray paths through the overburden, the static shift at each surface location is the same, regardless of from which shot the data are. Thus, near-surface corrections methods assign the same uniform time shift or filter to a distinct surface location.

Now consider near-receiver scattering. If the anomaly is close to the receiver, it does not matter if the ray path through the overburden is vertical or not (this reasoning is consistent with

the conclusions from Section 3.1). Each reflection event scatters at the same anomaly. In this way, our impedance is surface consistent.

To verify this assertion, we derive an impedance function from the first arriving wave in shot record 341 and use this function to estimate scattered energy on another record (shot 346). To this end, we have selected a shot record with comparable frequency content. The frequency spectrum of shot record 341 is shown in Figure 4.9a. Because the ground conditions along the survey line can be roughly divided in three different areas, we select a shot from the same area. This spectrum is shown in Figure 4.9b. Comparing Figure 4.9a-b reveals that the frequency content is comparable.

To give an idea of the variability of the frequency spectrum among different shot positions, we have plotted the spectrum of part of a shot at the other side of the line with different ground conditions (shot 343), for the same receivers. Comparing these figures, it is clear that the frequency content of shot 343 is lower than that of shot 341 and 346. Consequently, the impedance function derived from an event in shot 341, can not cover the whole range of frequencies found in shot 343. Moreover, from looking at the data from this shot we have found that they seem to be less sensitive to the near-surface heterogeneity. This is most probably due to the longer wavelengths observed in this record that are less sensitive to small-scale heterogeneities. This example shows that the local ground conditions at the source and the propagation path from the source to the heterogeneities can have impact on the application of our method.

In Figure 4.10a we zoom in on the boxed area in Figure 4.2b (shot 341), while Figure 4.10b shows the same area but from shot 346. We now follow the procedure described above, and estimate the near-surface impedance function from the first arriving event in Figure 4.10a. In Figure 4.10c we show the part of shot 341 after we have predicted and subtracted the near-receiver scattered energy followed by a mild $k - f$ filter. With the same impedance function, derived from the event in shot record 341, we now predict the near-surface scattered field on shot record 346. After subtracting this predicted scattered energy and applying the same $k - f$ filter as in Figure 4.10c, we obtain the record shown in Figure 4.10d.

As a verification that this result is due to application of our method, we show the same part of shot 341 after the mild $k - f$ filter only in Figure 4.10e. Finally, the same part of shot 346 after application of the same $k - f$ filter is shown in Figure 4.10f, which shows that the interference remains after the dip filter only. Consequently, the improvement in this record is due to application of our method.

From a glance at Figures 4.10c-d we find that the results obtained are similar for both shot records. Thus, even though we have derived the impedance function from one shot record, we can use it to predict the scattered energy effectively on another shot record. We have actually carried out this test for a few shot records. From these tests we have found that it is important that the frequency contents of the shot records are comparable. Because we estimated an impedance function under receivers that are fixed at the same surface location for different shots, this is a demonstration of surface-consistency.

This example also suggests that we could derive an impedance function that is consistent

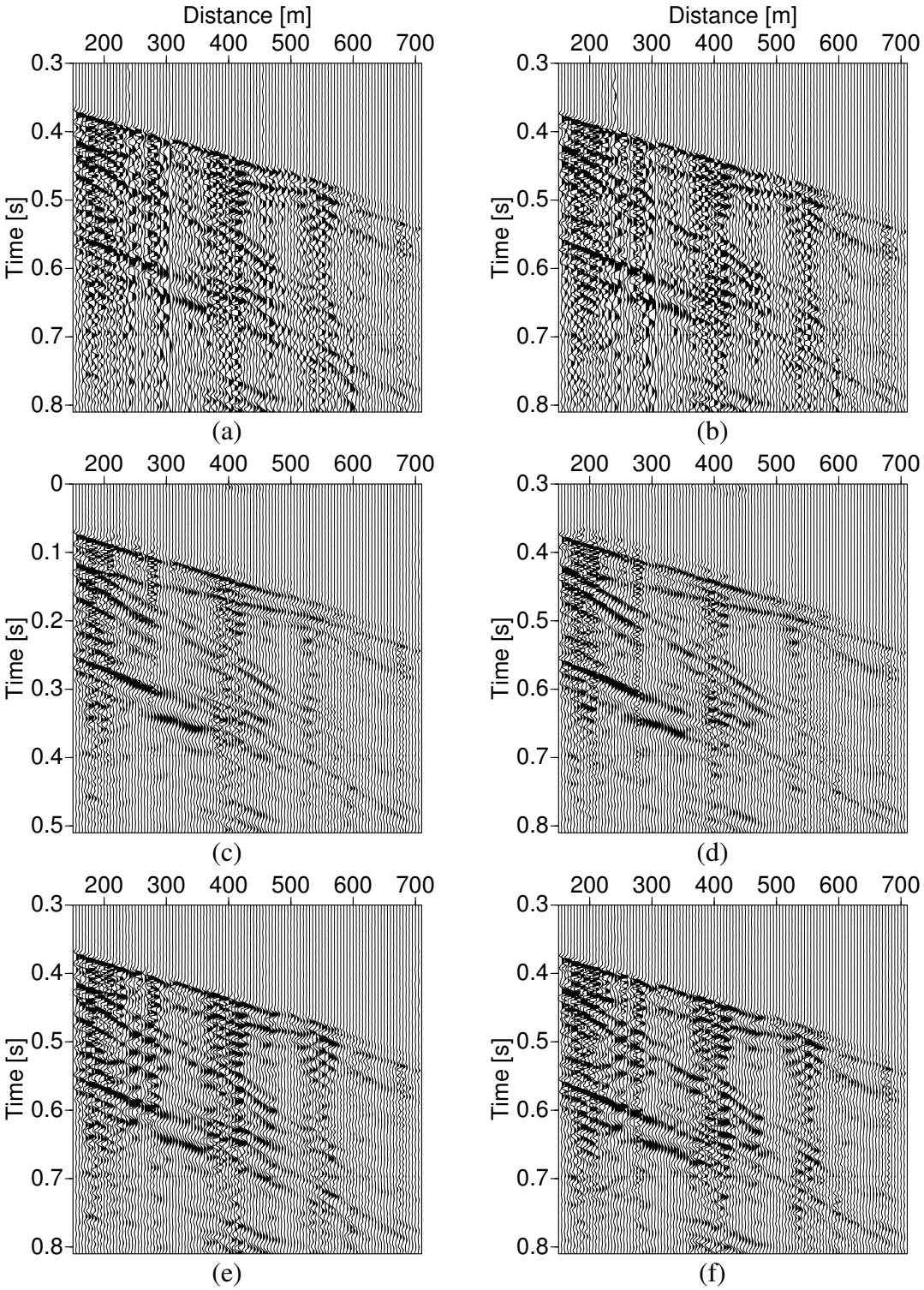

Figure 4.10: *(a) Detail from shot 341 (the boxed area in Figure 4.2b). (b) Same detail, but now from shot 346. (c) Same as (a), but after predicting and subtracting near-receiver scattering and a mild $k - f$ filter. (d) Same as (b), but after predicting and subtracting near-receiver scattering and the same $k - f$ filter. The impedance function used to predict the scattered field on this record was derived from the first arriving event of shot 341 in (a). (e) Same as (a), but after a dip filter only. (f) Same as (b), but after a dip filter only.*

with several shot records. This was also found and shown by Blonk and Herman (1994). Even though we have included this possibility in our algorithm, it requires that we also estimate the scattered energy from several reference events in a consistent way. So far, consistently estimating this scattered energy from several events in different shot records remains a challenge.

4.2 Saudi Aramco Data

4.2.1 Geometry

The data from Saudi Aramco were acquired in the desert of Saudi Arabia. In the acquisition area surface topography plays a more significant role than in the area where the data of the previous section were acquired. Besides topography, occasionally there can be some lateral variations due to surface anhydrite, but in the areas we have analyzed these variations do not play a significant role; we show that scattering is most probably due to the changes in topography. We focus our attention on the shot record shown in Figure 4.11 (displayed is the vertical velocity).

This shot record contains 2880 traces. Each trace in the data actually represents the sum of a group with twelve elements. The groups are used to suppress side-scattered noise (see also Pecholcs et al., 2002). The group spacing is 5 meter in the inline direction, while the width of a group is about 2 meter and its length 27.5 meter.

4.2.2 Topography

We selected the area between 2860 and 3470 meters (121 stations) in Figure 4.11. In this area, surface topography changes relatively fast compared to other areas, which results in scattering.

When we plot the topography on top of the data, we clearly see that the first arrival follows the topography (note that the wavefront is shifted down when the elevation is higher). From the headers we infer that the difference in elevation does not exceed 10 m in this part of the data. The lateral extent ranges from roughly 50 to 100 meters. Even though the elevation is moderate compared to the lateral extent of the dunes, from inspecting Figure 4.12 we conclude that there is a strong correlation between the location of the elevation variations and scattering. This is most evident from the scattering and interference between 2900 and 3100 m and between 3200 and 3300 m.

As we have discussed in Section 1.2, elevation statics are often corrected by time shifts based on the elevation in the header and a known velocity, assuming vertical ray paths in the near subsurface. More recently, wave-field based datuming techniques have been used to redatum the data collected at the surface to a datum beneath the overburden (Berryhill, 1984; Kelamis et al., 2002). In principle, this should also undo the effects of surface topography. In general, these datuming methods are based on a ray-approximation of the (primary) wave field. For this reason, they do not take into account the near-receiver scattered field, including body-to surface

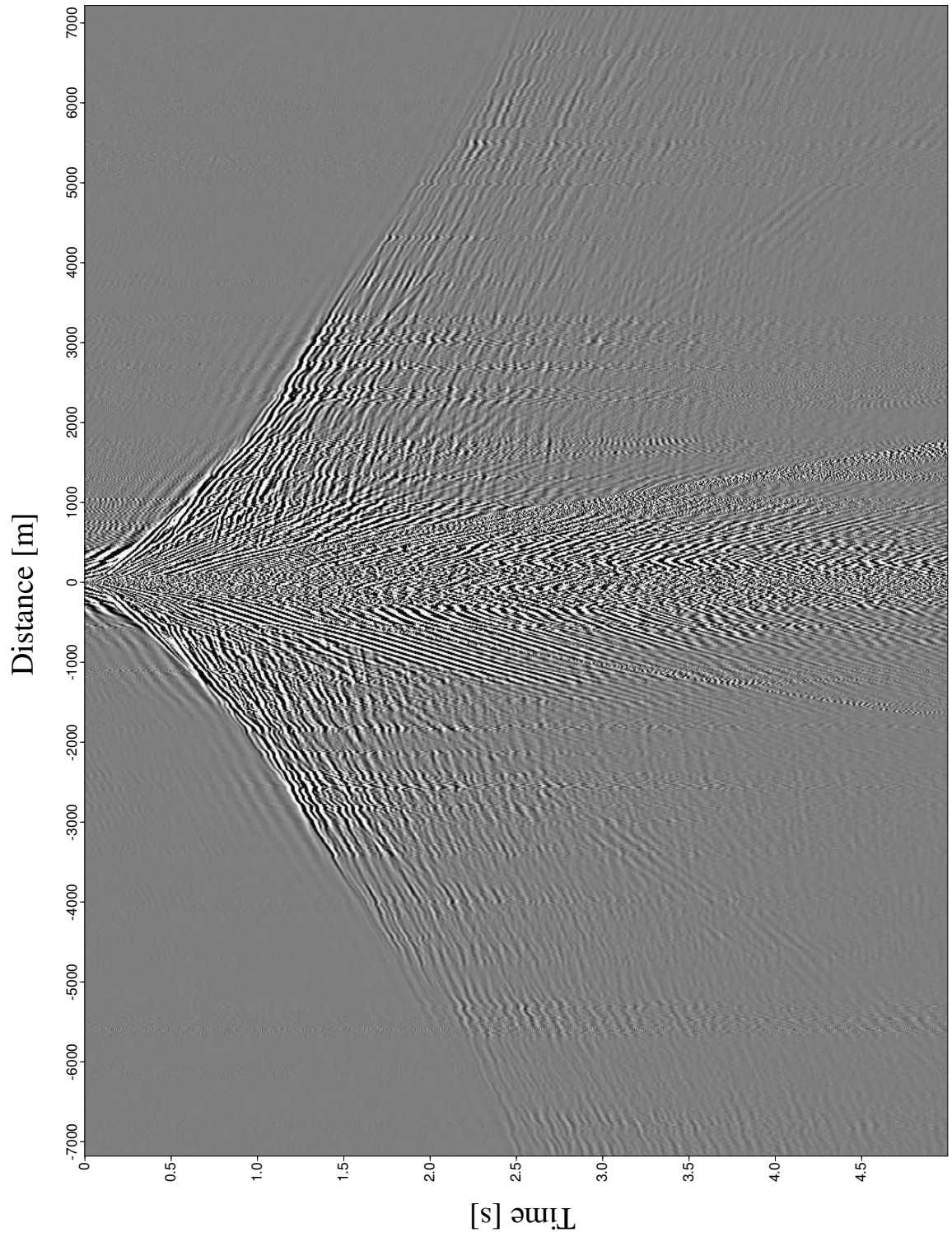

Figure 4.11: *Representative shot record from the Saudi Aramco data. The lateral near-surface variations are mostly attributed to topography (sand dunes). In general, variations are quite smooth. However, in some areas, more rapid variations cause scattered noise which interferes with reflections.*

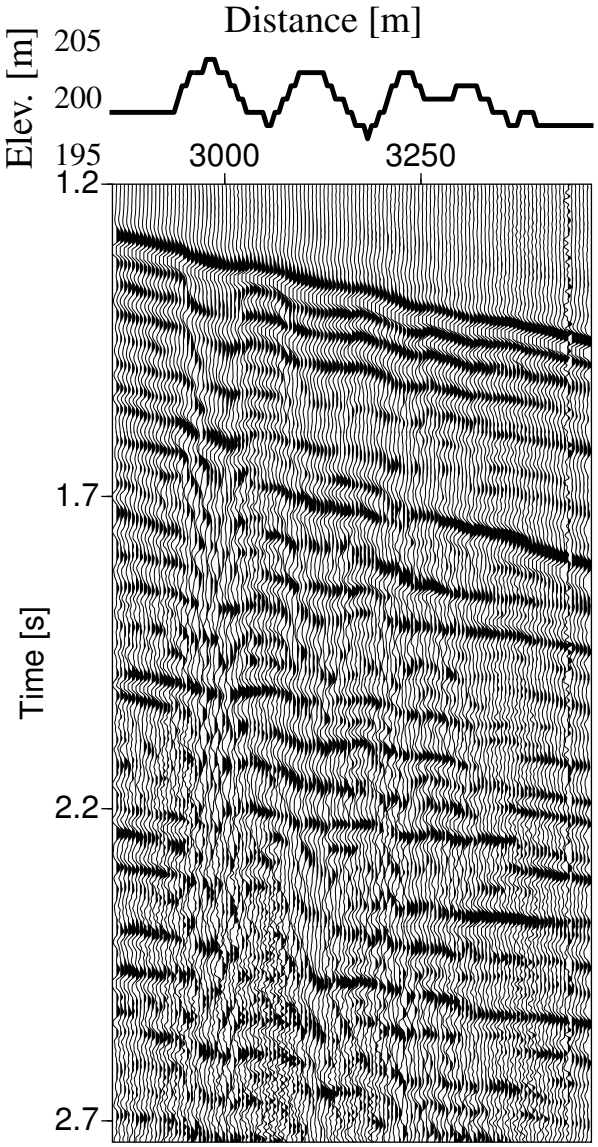

Figure 4.12: *(a) Selected data from Figure 4.11, with topography indicated. These data are the input of our algorithm. We have applied AGC to balance the amplitudes for display purposes.*

wave conversions.

Therefore, before redatuming methods can be successfully applied, near-surface scattered noise should be removed. If this noise is not suppressed, it will be extrapolated with the same operators giving rise to artifacts. This will especially affect the amplitudes of the redatumed data (Hindriks, 2003).

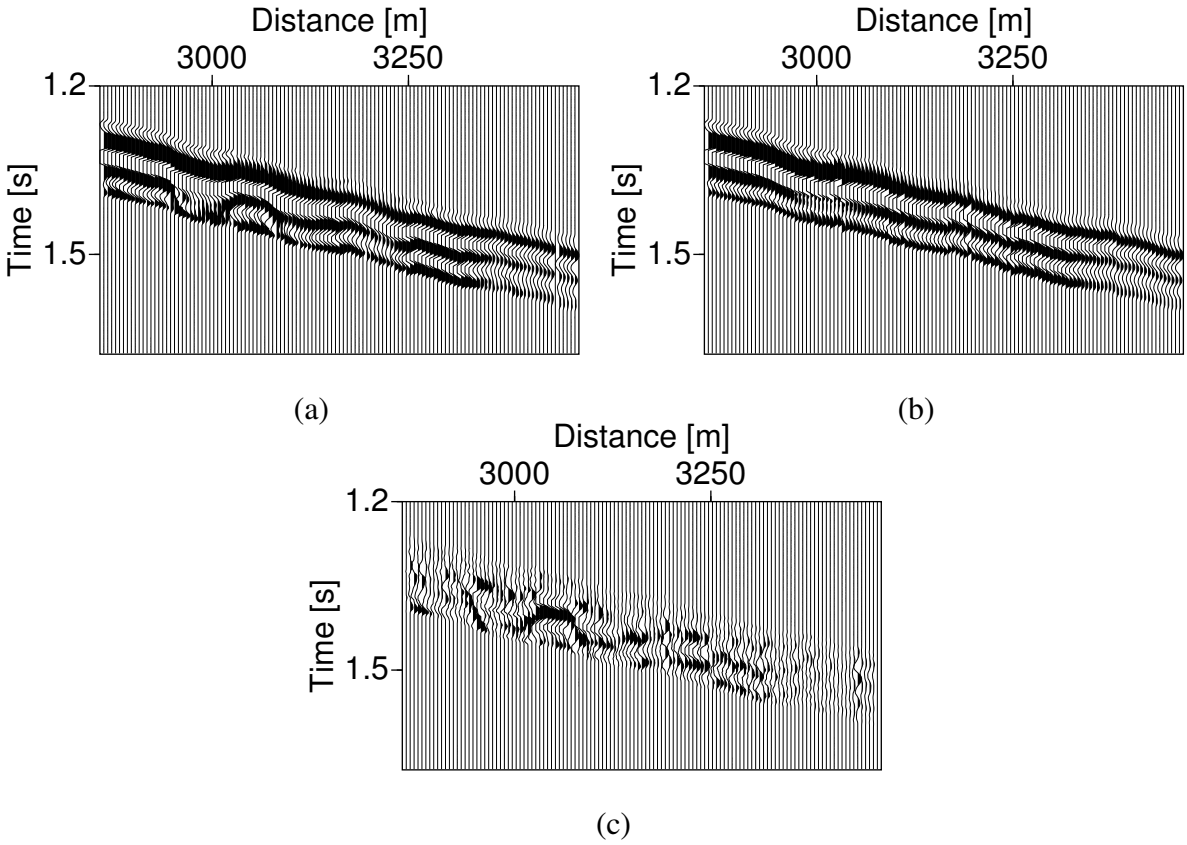

Figure 4.13: *(a) The reference event. (b) Estimated wave field in the embedding. We have kept the topography trend in this estimate. (c) Estimated scattered energy, i.e. the difference of (a) and (b). Note the diffraction at 3050 m responsible for the interference observed in (a).*

4.2.3 Wave-Field Separation

The whole sequence of steps to apply to these data is similar to the one in the previous example. However, here we deal with more complicated surface topography. In Figure 4.12, we have plotted the elevation (taken from the headers of the data) on top of the part of the line we process.

We start by selecting a reference event. For this purpose, we use the first two arrivals (see Figure 4.13a). Because of the surface topography, we did not apply NMO in this case. Instead, we picked the arrival times following the first breaks. In this way, we keep the main trend of the surface topography in the reference event.

After aligning this event using the picks, we apply an α-trimmed mean filter. Using this filter we can separate the more rapid variations from the slower variations. The rapid variations are

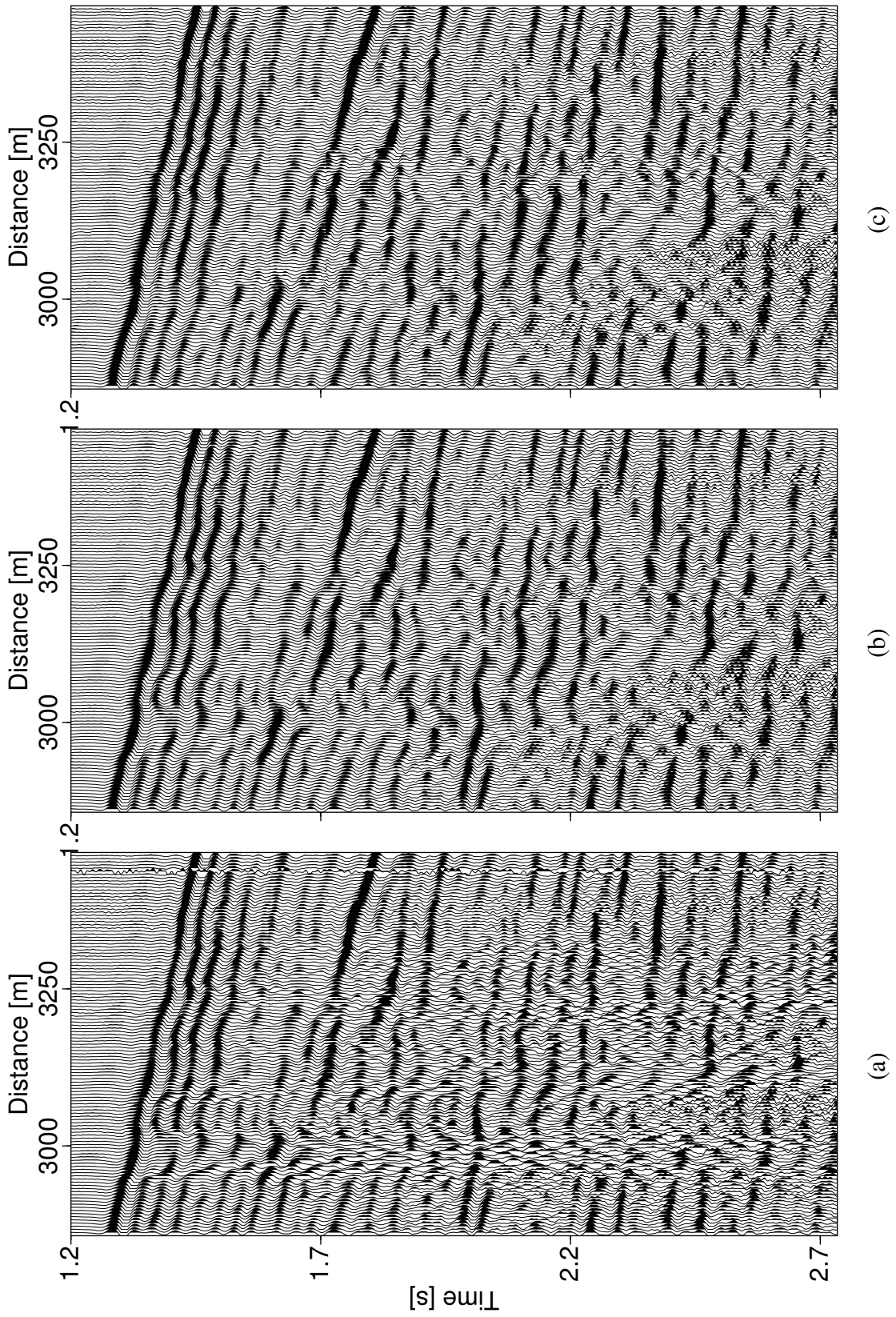

Figure 4.14: *(a) Same as Figure 4.12 (b) Same as (a), but after a mild dip filter to remove the steeply dipping noise trains. (c) Same as (a), but after subtracting predicted scattered waves followed by application of the same dip filter as in (b). We have applied AGC to balance the*

attributed to scattering from topography changes (Figure 4.13b), while the slow variations are attributed to propagation in the laterally varying near-surface region of the embedding medium (Figure 4.13c). We observe that we have maintained the topography trend in the estimate of the wave field in the embedding.

By preserving the slow topography variations in the reference event we do not correct for them in our procedure. However, because we aim at removing the locally scattered energy which interferes with reflections, the data will be better conditioned for application of methods that correct for topography, such as those discussed in Section 1.3.2.

4.2.4 Result

After separating the scattered energy from the reference event, we apply our algorithm in exactly the same way as in the previous section. First, we image the scattered energy, yielding the near-receiver scattering distribution. With this distribution, we predict the scattered energy in the rest of the data. The input data are repeated in Figure 4.14a.

For comparison, we have again plotted the input data after a mild dip filter to remove the coherent noise trains with steep dips (Figure 4.14b). This noise is especially clear between 2900 and 3000 meter and is most probably due to conversion of incident body waves and refractions to Rayleigh waves. Note that it is quite well removed using the dip filter, as can be observed in the figure. However, we observe that the parts of the scattered noise with higher apparent velocities still cause interference. A smaller pass band of the dip filter does remove some of the higher apparent velocities, but at the cost of 'smearing' the reflection energy and a consequent loss of high frequencies.

After subtracting the predicted scattered waves and applying the same dip filter, we obtain the output shown in Figure 4.14c. We observe that the continuity of events is better. Note that the first arrival has been used to derive the near-receiver scattering impedance and should therefore resemble the incident wave field shown in Figure 4.13b. Comparing these figures indeed conforms that they resemble quite well, which indicates that the minimization scheme worked well.

Because we kept the topography trend in the estimate of the wave field in the embedding we have shown that our method is not restricted to areas with a strictly flat surface. However, a more rigorous analysis of how to incorporate topography in our method has to be performed because in our example we used hand picked times. Doing so, we assume that we have information about how the topography changes. In order to incorporate actual topography, one could think of constraining the filter to follow a moving average of the actual elevation header values. We also expect that the results obtained here can be improved by using a semi-automatic picking program, because it will lead to a smoother estimate of the incident wave field.

We have applied this test to other areas in these data, where the surface is changing more slowly. It turned out that our method hardly affects the data in those areas. In those cases, the dip filter is about as effective as our method because there are hardly any rapid changes that

cause scattering.

Finally, we note that despite the fact that the data have group formed in the cross line direction, our method gives good results, without introducing artifacts.

5

Conclusions and Discussion

Conclusions

We developed a method to image, predict and suppress near-receiver scattered waves for seismic land data. The objective of our method is to obtain an estimate of the wave field that would have been measured if there were no heterogeneities close beneath the receivers.

To develop an efficient model, we identified the main features of near-receiver scattering. It is characterized by a time shift in the wavefront of upcoming reflections, due to the difference in velocity between the embedding and scattering media. Secondly, the incoming wavefront excites surface waves when it impinges on near-receiver heterogeneity. These surface waves cause interference with the incident wave, resulting in additional phase and amplitude changes. Based on these observations we derived an integral representation, accounting for the dominant effects of body-to-surface wave scattering in the vicinity of the receivers.

Our representation contains an approximation to the near-field behavior of the elastic Green's function of the near-surface region, a surface impedance function (representing the scatterers) and the actual vertical particle velocity measured in the field. We have shown that this scalar representation accurately models elastic scattering in the near-field region of the geophones. Even though we have focused on body-to-surface wave scattering, we have found that it applies to surface-to-surface wave scattering as well.

The integral representation forms the computational basis of our method to suppress near-receiver scattered waves. The underlying idea, however, is that with knowledge of the distribution of near-surface scatterers, it is possible to predict and subsequently subtract scattered waves. Hence, an important step is the determination of a near-surface scattering distribution. We estimate this distribution from the data itself, using short time windows to obtain an independent estimate of the impedance function. Despite the fact that we only require this impedance function to predict the scattered wave field accurately, we have found that in many cases it results in a physically meaningful spatial image of the scattering distribution.

We have demonstrated that the impedance function, derived from one event in the data, predicts the scattered waves excited by other events with different angles of incidence for mean scattering depths up to about a Rayleigh wavelength. From tests on synthetic data we found that

if the scatterers are deeper and the the difference between the angle of incidence from the reference event and that of the target event is larger than about 10 degrees, the predicted scattered fields start to differ significantly from the actual scattered field. Nonetheless, in most cases the dominant energy in the scattered field (in the apex of the scattering hyperbola) is still effectively modeled.

The embedding medium is characterized by the fundamental mode Rayleigh wave velocity, but our method is not very sensitive to this parameter. In practice, we apply a mild dip filter to remove any remnants of scattered surface waves with linear move out. Because our method compensates for rapid time shifts observed in the wavefronts and additional phase and amplitude changes, the continuity and trace-to-trace coherency of events is greatly improved after application. In addition, our method restores individual wave forms fairly well.

From our experience with two field data sets we conclude that our method suppresses scattered noise due to heterogeneities and changes in surface topography. These tests show that our scattering model effectively discriminates between upcoming body-wave reflections and scattered noise. Because the data were quite noisy and in one example data were acquired with geophone arrays, we conclude that our method is quite robust. These tests also confirm that we do not need detailed information about the subsurface. The fundamental Rayleigh wave velocity suffices and this can be estimated from the data. By estimating the impedance function from one shot, and successfully predicting and subtracting the scattered field from data from another shot, we show that our method is surface consistent.

Discussion

The results described in this thesis show the potential of our prediction and suppression method for use on a larger scale. However, there is room for improvements and extensions.

Although the method has been implemented such that we can use information from various shot records to estimate an impedance function that is consistent with these records, we have not yet used this possibility. The main reason for this is that to obtain an impedance function, also the separated scattered energy from the events from the different records have to be consistent. In this case, data selection is important and the filter has to be the same over the various events.

Although it should be limited to a minimum, we expect that some data preprocessing may improve our results. For example, our inversion algorithm is more sensitive to higher amplitudes than to lower amplitudes. For this reason, we expect that trace editing to remove anomalous traces and trace balancing before inversion results in a physically more reasonable impedance function.

In this thesis we have specifically focused on developing our method for and applying it to exploration seismic data. In recent years, however, there has been a large effort in adopting seismic imaging algorithms for teleseismic imaging of the Earth's upper-mantle (Marfurt et al., 2003, e.g.). This development has been stimulated by the availability of increasingly denser

geophone arrays. Especially data from short-period sensors have the potential of producing high resolution images. However, body-to-surface wave scattering limits the maximum obtainable resolution from these data (Wagner and Langston, 1992; Morozov and Dueker, 2003; Rondenay et al., 2003). We expect that one can also apply our method to suppress scattered surface waves in short-period passive-source seismic data without major modifications.

Although we do not require the impedance function to correspond to the actual scattering distribution, we found that it does give physically meaningful spatial images of the near-subsurface. In Herman et al. (2000b) and Campman et al. (2004), it is shown that by imaging the near-surface scattered field, one can spatially resolve near-surface scatterers. From these images, we cannot infer the depth of the scatterers, but in combination with other (dispersion, e.g.) information, this image may provide useful information that can be used in archaeology, civil engineering, (non contacting) land-mine detection (Van Wijk et al., 2005) or even exploration of aquifers.

Bibliography

Aki, K. and Richards, P. G. (1980) Quantitative seismology, vol. I, Freeman.

Baeten, G. J. M., Belougne, V., Combee, L., Kragh, E., Laake, A., Martin, J. E., Orban, J., Özbek, A., and Vermeer, P. L. (2000) *Acquisition and processing of point receiver measurements in land seismic*, in: *Exp. Abstr., 70th Ann. Internat. Mtg.*, Soc. of Expl. Geoph., pp. 41–44.

Baeten, G. J. M., Combee, L., and West, L. (2001) *Static perturbation corrections on single sensor data*, in: *Ext. Abstr., 63rd Mtg.*, Europ. Assn. Geophys. Eng., Session: IS–01.

Bannister, S. C., Husebye, E. S., and Ruud, B. O. (1990) *Teleseismic P-coda analyzed by three-component and array techniques –deterministic location of topographic P-to-Rg scattering near the NORESS array*, Bull. Seism. Soc. Am., **80**, pp. 1969–1986.

Barends, F. B. J. (1971) Elasto-dynamic response of a half plane, Internal Report, Dept. of Civil Eng.,Delft University.

Bednar, J. B. and Watt, T. L. (1984) *Alpha-trimmed means and their relationship to median filtering*, IEEE Trans. on Acoust., Speech, Signal processing., **32**, pp. 145–153.

Berni, A. J. and Roever, W. L. (1989) *Field- array performance: Theoretical study of spatially correlated variations in amplitude coupling and static shift and case study in the paris basin*, Geophysics, **54**, pp. 451–459.

Berryhill, J. R. (1984) *Wave-equation datuming before stack*, Geophysics, **49**, pp. 2064–2066.

Blaquière, G. and Ongkiehong, L. (2000) *Single sensor recording: anti-alias filtering, perturbations and dynamic range*, in: *Exp. Abstr., 70th Ann. Internat. Mtg.*, Soc. of Expl. Geoph., pp. 29–32.

Bleistein, N., Cohen, J. K., and Stockwell Jr., J. W. (2001) Mathematics of multidimensional seismic imaging, migration and inversion, Springer-Verlag.

Blonk, B. (1994) Removal of scattered surface waves from seismic data, PhD-thesis, Delft University.

Blonk, B. and Herman, G. C. (1994) *Inverse scattering of surface waves : A new look at surface consistency*, Geophysics, **59**, pp. 963–972.

Brigham, E. O. (1988) The Fast Fourier Transform and its applications, Prentice Hall.

Burger, P., Garotta, R., and Granger, P.-Y. (1998) *Improving resolution and seismic quality assurance through field preprocessing*, The Leading Edge, **17**, pp. 1562–1568.

Cambois, G. and Stoffa, P. (1993) *Surface-consistent deconvolution in the log/Fourier domain*, Geophysics, **57**, pp. 1099–1111.

Campman, X., van Wijk, K., Riyanti, C. D., Scales, J., and Herman, G. (2004) *Imaging scattered seismic surface waves*, Near Surface Geophysics, **2**, pp. 223–230.

Cohen, J. K., Hagen, F. G., and Bleistein, N. (1986) *Three dimensional Born inversion with an arbitrary reference*, Geophysics, **51**, pp. 1552–1558.

Combee, L. (1994) *Wavefield scattering by a 2-d near-surface elliptic anomaly*, in: *Exp. Abstr., 64th Ann. Internat. Mtg.*, Soc. of Expl. Geoph., pp. 1306–1309.

Cooper, N. (2004) *A world of reality – Designing land 3D programs for signal, noise and prestack migration – Part 2*, The Leading Edge, **23**, pp. 1230–1235.

Cox, M. J. G. (1999) Static corrections for seismic reflection surveys, Soc. of Expl. Geophys.

De Hoop, A. T. (1995) Handbook of radiation and scattering of waves, Academic Press.

Ernst, F., Blonk, B., and Herman, G. (1998) *Reduction of near-surface scattering effects in seismic data*, The Leading Edge, **17**, pp. 759–764.

Ernst, F. E. (1999) Modeling, imaging and removal of guided waves, PhD-thesis, Delft University.

Gersztenkorn, A. and Scales, J. A. (1988) *Smoothing seismic tomograms with alpha-trimmed means*, Geophysical Journal, **92**, pp. 67–72.

Hansen, P. C. (1997) Rank-deficient and discrete ill-posed problems: Numerical aspects of linear inversion, SIAM.

Harr, M. E. (1966) Foundations of theoretical soil mechanics, McGraw-Hill.

Herman, G. C., Milligan, P. A., Dong, Q., and Rector, J. W. (2000a) *Analysis and removal of multiply scattered tube waves*, Geophysics, **65, 3**, pp. 745–754.

Herman, G. C., Milligan, P. A., Huggins, R. J., and Rector, J. W. (2000b) *Imaging shallow objects and heterogeneities with scattered guided waves*, Geophysics, **65**, pp. 247–252.

Herman, G. C. and Perkins, C. (2004) *Predictive scattered noise removal*, in: *Ext. Abstr., 66th Mtg.*, Europ. Assn. Geophys. Eng., Session: D027.

Hindriks, C. O. H. (2003) Personal Communication.

Hindriks, C. O. H. and Verschuur, D. J. (2001) *CFP approach to the complex near surface*, in: *Expanded abstracts, 71st Ann. Internat. Mtg.*, Soc. of Expl. Geoph., pp. 1863–1866.

Hudson, J. A. (1977) *Scattered waves in the coda of P*, J. Geophys., **43**, pp. 359–374.

International Energy Agency (2004a) *Oil Market Report,*10 nov, <http://omrpublic.iea.org/omrarchive/10nov04full.pdf>.

— (2004b) World energy outlook 2004, International Energy Agency, Paris.

Kelamis, P., Erickson, K. E., Verschuur, D. J., and Berkhout, A. J. (2002) *Velocity-independent redatuming: A new approach to the near-surface problem in land seismic data processing*, The Leading Edge, **21**, pp. 730–735.

Kleinman, R. E. and van den Berg, P. M. (1991) *Iterative methods for solving integral equations*, Radio Science, **26**, pp. 175–181.

Langston, C. A. (1979) *The structure under Mount Rainer, Washington, inferred from teleseismic body waves*, J. Geophys. Res., **84**, pp. 4749–4762.

Levander, A. R. (1990) *Seismic scattering near the Earth's surface*, Pure Appl. Geophys., **132**, pp. 21–47.

Los, H. S., Herman, G. C., and Hölscher, P. (2001) *Dynamic interaction between train wheels and the subsurface*, Journal of sound and vibration, **247, 5**, pp. 917–926.

Marfurt, K. J., Johnson, R. A., and Pennington, W. D. (eds). (2003) *Special section: Solid-Earth seismology*, The Leading Edge, **22**, pp. 218–271.

Mars, J., Rector, J., and Lazaratos, S. K. (1999) *Filter formulation and wavefield separation of cross-wellseismic data*, Geophysical Prospecting, **47**, pp. 610–636.

Marsden, D. (1993) *Static corrections — a review, part 1*, The Leading Edge, **12**, pp. 43–49.

McMechan, G. A. and Chen, H. W. (1990) *Implicit static corrections in prestack migration of common-source data*, Geophysics, **55**, pp. 757–760.

Miller, D., Oristaglio, M. L., and Beylkin, G. (1987) *A new slant on seismic imaging: Migration and integral geometry*, Geophysics, **52**, pp. 943–964.

Moldoveanu, N., Uribe, J., and Stathopoulos, D. (2004) *Point-source/point-receiver land acquisition: Torrecillas- Mexico experiment*, in: *Exp. Abstr., 74th Ann. Internat. Mtg.*, Soc. of Expl. Geoph., p. ACQ 1.6.

Morozov, I. B. and Dueker, K. G. (2003) *Signal-to-noise ratios of teleseismic receiver functions and effectiveness of stacking for their enhancement*, J. Geophys. Res., **108**(B2), doi:10.1029/2001JN001692.

Morse, P. F. and Hildebrandt, G. F. (1988) *Ground-roll suppression by the stackarray*, in: *Exp. Abstr., 58th Ann. Internat. Mtg.*, Soc. of Expl. Geoph., p. S14.5.

Morse, P. M. and Feshbach, H. (1953) Methods of theoretical physics, Mc. Graw-Hill.

Muyzert, E. and Vermeer, P. (2004) *The impact of acquisition perturbations on land seismic data*, in: *Exp. Abstr., 74th Ann. Internat. Mtg.*, Soc. of Expl. Geoph., Session: ACQ 3.5.

Neidell, N. S. and Taner, M. T. (1971) *Semblance and other coherency measures for multichannel data*, Geophysics, **36**, pp. 482–497.

Nishizawa, O., Sato, T., Lei, X., and Kuwahara, Y. (1997) *Laboratory studies of seismic wave propagation in inhomogeneous media using a laser Doppler vibrometer*, Bull. Seism. Soc. Am., **87**, pp. 809–823.

Panea, I., Drijkoningen, G. G., Bertotti, G., and Matenco, L. (2003) *Effect of perturbation on array forming*, in: *Exp. Abstr., 73rd Ann. Internat. Mtg.*, Soc. of Expl. Geoph., pp. 1–4.

Pecholcs, P. I., Hasting-James, R., Barsoukov, N., and Al-Ramadhan, A. A. (2002) *Universal land acquisition 14 years later*, in: *Exp. Abstr., 72rd Ann. Internat. Mtg.*, Soc. of Expl. Geoph., pp. 56–59.

Perkins, C. and Calvert, R. (2001) *Mixed phase surface consistent deconvolution without phase unwrapping*, in: *Ext. Abstr., 63th Mtg.*, Europ. Assn. Geophys. Eng., Session: A–23.

Regone, C. J. (1997) *Measurement and identification of 3-D coherent noise generated from irregular surface carbonates*, in: *Carbonate seismology* (K. J. Marfurt, ed.), Soc. of Expl. Geophys., pp. 281–305.

— (1998) *Suppression of coherent noise in 3-D seismology*, The Leading Edge, **17**, pp. 1584–1589.

Reshef, M. (1991) *Depth migration from irregular surfaces with depth extrapolation methods*, Geophysics, **49**, pp. 119–122.

Riyanti, C. D. and Herman, G. C. (2005) *Three-dimensional elastic scattering by near-surface heterogeneities*, Geophys. J. Int., **160**, pp. 609-620.

Rondenay, S., Bostock, M. G., and Fisher, K. M. (2003) *Multichannel inversion of scattered teleseismic body waves: practical considerations and applicability*, in: *Seismic data analysis and imaging with global and local arrays* (A. Levander and G. Nolet, eds.), AGU, In press.

Ronen, S. and Claerbout, J. F. (1985) *Surface-consistent residual statics estimation by stack-power maximization*, Geophysics, **50**, pp. 2759–2767.

Rowbotham, P. S. and Goulty, N. R. (1990) *Wavefield separation by 3-D filtering in crosshole seismic reflection processing*, Geophysics, **55**, pp. 1216–1222.

Scales, J. A. and Malcolm, A. (2003) *Laser characterization of ultrasonic wave propagation in random media*, Phys. Rev. E, **67, 4**, pp. 046618–046624.

Scales, J. A. and van Wijk, K. (1999) *Multiple scattering attenuation and anisotropy of ultrasonic surface waves*, Applied Physics Letters, **74**, pp. 3899–3901.

Scruby, C. B. and Drain, L. (1980) Laser ultrasonics: techniques and applications, IOP.

Sevink, A. G. J. and Herman, G. C. (1994) *Fast iterative solution of sparsely sampled seismic inverse problems*, Inverse Problems, **10**, pp. 937–948.

Sheriff, R. E. (2002) Encyclopedic Dictionary of Applied Geophysics, Soc. of Expl. Geophys.

Shieh, C. F. and Herrmann, R. B. (1994) *Ground roll: Rejection using polarization filters*, Geophysics, **59**, pp. 1065–1071.

Snieder, R. K. (1986) *3d linearized scattering of surface waves and a formalism for surface wave holography*, Geophys. J. R. Astron. Soc., **84**, pp. 581–605.

Stewart, R. R. and Schieck, D. G. (1989) *3-D F-K filtering*, in: *Exp. Abstr., 59th Ann. Internat. Mtg*, Soc. of Expl. Geophys., pp. 1123–1126.

Taner, M. T. (1997) *Seismic data processing flow in areas of shallow carbonates*, in: *Carbonate seismology* (K. J. Marfurt, ed.), Soc. of Expl. Geophys., pp. 223–279.

Taner, M. T. and Koehler, F. (1981) *Surface consistent corrections*, Geophysics, **46**, pp. 17–22.

Taner, M. T., Koehler, F., and Alhilali, K. A. (1974) *Estimation and correction of near-surface time anomalies*, Geophysics, **39**, pp. 441–463.

Tarantola, A. (1984) *Linearized inversion of seismic reflection data*, Geophysical Prospecting, **32**, pp. 998–1015.

Telford, W. M., Geldart, L. P., and Sheriff, R. E. (1990) Applied Geophysics, Cambridge.

Van den Berg, P. M. (2002) *Nonlinear scalar inverse scattering: algorithms and applications*, in: *Scattering and inverse scattering in pure and applied science* (R. Pike and P. Sabatier, eds.), Academic Press, pp. 142–161.

Van der Veen, M. and Herman, G. C. (2001) *Impact of near-surface scattering on seismic data in Oman*, in: *Ext. Abstr., 63rd Mtg.*, Europ. Assn. Geophys. Eng., Session: IS–05.

Van Wijk, K., Scales, J. A., Mikesell, T. D., and Peacock, J. R. (2005) *Toward noncontacting seismology*, Journal of Geophysical Research, **32**, dio:10.1029/2004GL021660.

Wagner, G. S. and Langston, C. A. (1992) *Body-to-surface-wave scattered energy in teleseismic coda observed at the NORESS seismic array*, Bull. Seism. Soc. Am., **82**, pp. 2126–2138.

Wendlandt, A. and Bream, R. (2003) *Shell to face grilling over reserve levels*, Financial Times, London, Mar 21.

Wiggins, R. A., Larner, K. L., and Wisecup, R. D. (1976) *Residual statics analysis as a general linear inverse problem*, Geophysics, **41**, pp. 922–938.

Wu, R. S. and Ben-Menahem, A. (1985) *The elastodynamic near field*, Geophys. J. R. Astr. Soc., **81**, pp. 609–621.

Yilmaz, O. (2001) Seimic data analysis, Soc. of Expl. Geophys.

Zhdanov, M. S. (2002) Geophysical inverse theory and regularization problems, Elsevier.

A

Fourier Transformations

A.1 Temporal Fourier Transformation

Let $f(\mathbf{x}, t)$ be a real valued function of space and time. The forward temporal Fourier transform is defined by

$$\tilde{f}(\mathbf{x}, \omega) = \int_{-\infty}^{\infty} f(\mathbf{x}, t) \exp(-\mathrm{i}\omega t) \mathrm{d}t, \tag{A.1}$$

and the inverse transform:

$$f(\mathbf{x}, t) = \frac{1}{2\pi} \int_{-\infty}^{\infty} \tilde{f}(\mathbf{x}, \omega) \exp(\mathrm{i}\omega t) \mathrm{d}\omega. \tag{A.2}$$

Here, i is the imaginary unit ($\mathrm{i} = \sqrt{-1}$) and ω is angular frequency. For notational convenience, we omit the tilde over the frequency-domain function in the main text of this thesis. The only way we distinguish between time and frequency-domain quantities is via their arguments.

We will frequently use the property of this transformation that a differentiation with respect to time corresponds in a multiplication by $\mathrm{i}\omega$ in the frequency domain.

A.2 Spatial Fourier Transformation

The two-dimensional spatial Fourier transformation of $f(\mathbf{x}, \omega)$ is defined as:

$$\hat{f}(\mathbf{k}_L, \omega) = \int_{-\infty}^{\infty} \int_{-\infty}^{\infty} \tilde{f}(\mathbf{x}_L, \omega) \exp(\mathrm{i}k_\alpha x_\alpha) \mathrm{d}^2\mathbf{x}_L, \tag{A.3}$$

and the inverse transformation as:

$$\tilde{f}(\mathbf{x}_L, \omega) = \frac{1}{(2\pi)^2} \int_{-\infty}^{\infty} \int_{-\infty}^{\infty} \hat{f}(\mathbf{k}_L, \omega) \exp(-\mathrm{i}k_\alpha x_\alpha) \mathrm{d}^2\mathbf{k}_L. \tag{A.4}$$

Here, $\mathbf{x}_L = (x, y)$, $\mathbf{k}_L = (k_x, k_y)$ and $k_\alpha x_\alpha$ is the subscript notation for $\mathbf{k}_L \cdot \mathbf{x}_L$ (see also Section 2.1). For notational convenience, we omit the hat over the wavenumber-domain function in the main text of this thesis. The only way we distinguish between the spatial and wavenumber-domain quantities is via their arguments.

We use the property of the spatial Fourier transformation that a spatial differentiation in the spatial-domain is replaced by multiplication with $-\mathrm{i}k_\alpha$ in the two-dimensional wavenumber domain.

A.3 Convolution Theorem

We use the convolution theorem to calculate the convolutions occurring in our integral equation. This theorem follows from the properties of the Fourier transform as defined above. Let $f(\mathbf{x}, t)$ and $g(\mathbf{x}, t)$ be two functions of space and time. Then the temporal convolution integral of f and g is defined as:

$$h(\mathbf{x}, t) = \int_{-\infty}^{\infty} f(\mathbf{x}, t - t')g(\mathbf{x}, t')\mathrm{d}t'. \tag{A.5}$$

Taking the Fourier transformation of Equation (A.5), we obtain

$$h(\mathbf{x}, \omega) = f(\mathbf{x}, \omega)g(\mathbf{x}, \omega). \tag{A.6}$$

This result is known as the convolution theorem (see also Brigham, 1988).

Similarly, for two functions of space and frequency, we have the convolution integral in the spatial coordinates:

$$h(\mathbf{x}_L, \omega) = \int_{-\infty}^{\infty}\int_{-\infty}^{\infty} f(\mathbf{x}_L - \mathbf{x}'_L, \omega)g(\mathbf{x}'_L, \omega)\mathrm{d}^2\mathbf{x}'_L, \tag{A.7}$$

and the spatial convolution theorem:

$$h(\mathbf{k}_L, \omega) = f(\mathbf{k}_L, \omega)g(\mathbf{k}_L, \omega). \tag{A.8}$$

B

Derivation of Equation (2.7)

Using the elastic frequency-domain reciprocity theorem of time convolution type (De Hoop, 1995, pp. 445-448), we derive an integral representation for the wave field in terms of particle displacement.

B.1 Reciprocity

Let the interaction quantity $\Delta_{ijpq}\partial_i(\tau^A_{pq}u^B_j - \tau^B_{pq}u^A_j)$ account for local interaction between two elastodynamic states, denoted by superscripts A and B, in a solid occupying domain $\mathcal{D}$. Both states satisfy Equations (2.4) and (2.5). For the moment we do not specify boundary conditions.

We can write the interaction quantity as:

$$\Delta_{ijpq}\partial_i(\tau^A_{pq}u^B_j - \tau^B_{pq}u^A_j) = \Delta_{ijpq}\Big[\left(\partial_i\tau^A_{pq}\right)u^B_j + \tau^A_{pq}\left(\partial_i u^B_j\right) - \left(\partial_i\tau^B_{pq}\right)u^A_j - \tau^B_{pq}\left(\partial_i u^A_j\right)\Big]. \quad \text{(B.1)}$$

By substituting terms using Equations (2.4)-(2.5), one obtains:

$$\Delta_{ijpq}\partial_i(\tau^A_{pq}u^B_j - \tau^B_{pq}u^A_j) = \omega^2\left(\rho^B - \rho^A\right)u^A_i u^B_i + \left(s^B_{ijpq} - s^A_{pqij}\right)\tau^A_{ij}\tau^B_{pq} - f^A_i u^B_i + f^B_i u^A_i, \quad \text{(B.2)}$$

where we have used $\Delta_{ijpq} = \Delta_{pqij}$ and $s_{ijpq} = s_{pqij}$. This is the local form of the reciprocity theorem. Integrating over the domain $\mathcal{D}$ and applying Gauss' theorem, we obtain the global form of the Betti-Rayleigh reciprocity theorem:

$$\Delta_{ijpq}\int_{\partial\mathcal{D}} n_i\left(\tau^A_{pq}u^B_j - \tau^B_{pq}u^A_j\right)\mathrm{d}A = \int_{\mathcal{D}}\Big[\omega^2\left(\rho^B - \rho^A\right)u^A_i u^B_i + \left(s^B_{ijpq} - s^A_{pqij}\right)\tau^A_{ij}\tau^B_{pq}\Big]\mathrm{d}V - \int_{\mathcal{D}}\Big[f^A_i u^B_i - f^B_i u^A_i\Big]\mathrm{d}V. \quad \text{(B.3)}$$

As this relation holds for any two states in the domain $\mathcal{D}$, we can derive a representation for the actual wave field (state B) in $\mathcal{D}$, by suitably choosing state A.

B.2 Green's State

Green's state is the wave field in the embedding medium ($\rho = \rho^0, s_{ijkl} = s^0_{ijkl}$) caused by an impulsive point force in an arbitrary direction:

$$\Delta_{ijpq}\partial_j\tau^G_{pql}(\mathbf{x},\mathbf{x}') + \rho^0(\mathbf{x})\omega^2 u^G_{il}(\mathbf{x},\mathbf{x}') = -\delta_{il}\delta(\mathbf{x},\mathbf{x}'), \quad \text{(B.4)}$$

$$\Delta_{ijpq}\partial_p u^G_{ql}(\mathbf{x},\mathbf{x}') - s^0_{ijpq}(\mathbf{x})\tau^G_{pql}(\mathbf{x},\mathbf{x}') = 0. \quad \text{(B.5)}$$

The Green's state is labeled with superscript ^{G}. The boundary condition at the free surface for the Green's state is:

$$n_j \tau^G_{ijl}(\mathbf{x}) = 0, \qquad \mathbf{x} \in \Sigma, \tag{B.6}$$

while on account of the radiation condition, the wave field of the Green's state consists of waves propagating away from the sources at large distances.

B.3 Integral Representation

Associate the Green's state with state A and the actual wave field with state B. They satisfy the radiation condition and the following boundary conditions:

$$n_j \tau^G_{ijl}(\mathbf{x}) = 0, \qquad \mathbf{x} \in \Sigma, \tag{B.7}$$

and

$$n_j \tau_{ij} = 0, \qquad \mathbf{x} \in \Sigma. \tag{B.8}$$

On account of these conditions, the surface integral on the LHS of Equation (B.3) vanishes. Upon substituting the states and rearranging, this yields:

$$u_i(\mathbf{x}) = \int_{\mathcal{D}} u^G_{ij}(\mathbf{x}, \mathbf{x}') f_j(\mathbf{x}') \mathrm{d}V + \\ \omega^2 \int_{\mathcal{D}} u^G_{ij}(\mathbf{x}, \mathbf{x}')(\rho - \rho^0)(\mathbf{x}') u_j(\mathbf{x}') \mathrm{d}V + \int_{\mathcal{D}} \partial'_j u^G_{ik}(\mathbf{x}, \mathbf{x}') c^0_{kjns}(s_{nspq} - s^0_{nspq})(\mathbf{x}') \tau_{pq}(\mathbf{x}') \mathrm{d}V. \tag{B.9}$$

Here, we have used the reciprocity relation $u^G_{ij}(\mathbf{x}, \mathbf{x}') = u^G_{ji}(\mathbf{x}', \mathbf{x})$ (De Hoop, 1995, p. 471, Equation (15.8-47)) and we have expressed the stress Green's tensor, which occurs in the third term on the RHS of Equation (B.9), in terms of particle velocity, using the generalized Hooke's law:

$$\tau^G_{ijl} = c^0_{ijpq} \partial_p u^G_{ql}, \tag{B.10}$$

where c^0_{ijpq} [Pa] is the stiffness tensor. Here, we used $c_{ijkl} = c_{ijlk}$ and $\tau_{ijl} = \tau_{jil}$ (Aki and Richards, 1980).

Because we assume that the actual medium (ρ, s_{ijkl}) only differs from the embedding medium (ρ^0, s^0_{ijkl}) in the near-surface scattering domain $\mathcal{B}$ (see Figure 2.1), we may write:

$$u_i(\mathbf{x}) = \int_{\mathcal{D}} u^G_{ij}(\mathbf{x}, \mathbf{x}') f_j(\mathbf{x}') \mathrm{d}V + \\ \omega^2 \int_{\mathcal{B}} u^G_{ij}(\mathbf{x}, \mathbf{x}')(\rho - \rho^0)(\mathbf{x}') u_j(\mathbf{x}') \mathrm{d}V + \int_{\mathcal{B}} \partial'_j u^G_{ik}(\mathbf{x}, \mathbf{x}') c^0_{kjns}(s_{nspq} - s^0_{nspq})(\mathbf{x}') \tau_{pq}(\mathbf{x}') \mathrm{d}V. \tag{B.11}$$

The first term on the right hand side of Equation (B.9) is the incident field, the second and third term represent the secondary field caused by perturbations of the medium with respect to a background medium. Hence, the representation can be written as a superposition of the incident wave field u^0 and the scattered wave field u^1:

$$u_i(\mathbf{x}) = u_i^0(\mathbf{x}) + u_i^1(\mathbf{x}). \tag{B.12}$$

C

Iterative Minimization

C.1 Conjugate Gradient Method

We have posed the inversion problem as the problem of finding an impedance function that minimizes a cost function, consisting of a squared error between the measured data and the calculated data.

First, we define the residual, i.e. the misfit between the actual data and the calculated data:

$$r = d^1 - \mathcal{K}\sigma, \tag{C.1}$$

where the operator $\mathcal{K}$ has been defined through (Equation (2.32)):

$$\{\mathcal{K}\sigma\}(\mathbf{x}_L, 0) = \int_\Sigma u^G(\mathbf{x}_L - \mathbf{x}'_L, z^{(0)})\sigma(\mathbf{x}'_L, z^{(0)}, \omega)d^{meas}(\mathbf{x}'_L, 0)\mathrm{d}^2\mathbf{x}'_L. \tag{C.2}$$

Now, we define the error as the (L^2) norm of the residual:

$$\mathrm{Err} = ||r|| = \langle r, r\rangle^{\frac{1}{2}}, \tag{C.3}$$

where $\langle\cdot,\cdot\rangle$ denotes the inner product defined on the domain Σ:

$$\langle f, g\rangle = \int_\Sigma f(\mathbf{x}_L)\bar{g}(\mathbf{x}_L)\mathrm{d}^2\mathbf{x}_L. \tag{C.4}$$

Here, the over bar denotes complex conjugate.

We minimize the following cost function (Equation 2.33):

$$F = \frac{\sum_J ||d^1_J - \mathcal{K}_J\sigma||^2}{\sum_J ||d^1_j||^2}, \tag{C.5}$$

such that $F = 1$ if $\sigma = 0$ and $F = 0$ if σ is the exact solution, which corresponds to the normalized error. This cost function is minimized by iteratively updating the impedance function in the following way:

$$\begin{aligned} \sigma_0 &= 0, \\ \sigma_N &= \sigma_{N-1} + \alpha_N\gamma_N, \qquad N \geq 1. \end{aligned} \tag{C.6}$$

where γ_N is a suitably chosen update direction.

We use Polak-Ribière conjugate-gradient directions so that (e.g. Van den Berg, 2002):

$$\gamma_N = g_N + \frac{\mathrm{Re}\langle g_N - g_{N-1}, g_N\rangle}{||g_{N-1}||^2}\gamma_{N-1}, \tag{C.7}$$

where g_N is the gradient $\partial F_{N-1}/\partial\sigma$:

$$g_N = -\frac{\sum_J \mathcal{K}_J^* r_{J,N}}{\sum_J ||d_J^1||^2}, \tag{C.8}$$

and the adjoint operator $\mathcal{K}^*$ is defined through:

$$\langle \mathcal{K} f, g\rangle = \langle f, \mathcal{K}^* g\rangle. \tag{C.9}$$

For details about obtaining the gradient and an explicit expression for the adjoint, we refer to Zhdanov (2002), for example.

Carrying out the analysis described therein, yields:

$$\{\mathcal{K}^* r\}\,(\mathbf{x}'_L, z^{(0)}) = \bar{d}^{meas}(\mathbf{x}'_L, 0)\int_\Sigma \bar{u}^G(\mathbf{x}'_L - \mathbf{x}_L, z^{(0)}) r(\mathbf{x}_L, 0)\mathrm{d}^2\mathbf{x}_L, \tag{C.10}$$

for the adjoint operator.

To complete the algorithm, we determine α. By writing out Equation (C.5) and requiring for the derivative of the cost functional with respect to α to vanish, we obtain

$$\alpha_N = \frac{\sum_j \mathrm{Re}\langle r_{J,N-1}, \mathcal{K}_J\gamma_N\rangle}{\sum_J ||\mathcal{K}_J\gamma_N||^2}. \tag{C.11}$$

C.2 Regularized Conjugate Gradients

In practice, data contain noise and the solution described above may depend on it, leading to an unstable solution. To ensure a reasonable estimate of the impedance function, we regularize the inverse problem.

One way to regularize the minimization is to add a stabilizing term in the cost function:

$$F = \frac{\sum_J ||d_J^1 - \mathcal{K}_J\sigma||^2}{\sum_J ||d_J^1||^2} + \lambda||\sigma||^2. \tag{C.12}$$

In this way, with the right choice for λ we accomplish that the solution remains close to that of the solution of the unperturbed problem (with small residual norm and a model norm of 'reasonable' size).

We adopt a practical (and popular) method to choose this parameter: via the L-curve method (see Hansen, 1997, for an extensive treatment of this method). To this end, we introduce separate cost functions for either term in Equation (C.12):

$$F = \Phi(\sigma) + \lambda\Psi(\sigma). \tag{C.13}$$

Here, Φ is the cost function for the residual, while Ψ is the stabilizing cost-function.

In the L-curve method, one plots, usually in log-log scale, Φ versus Ψ for different values of the parameter λ. Plotted on this scale the curve typically describes an 'L' shape. In the bend of the 'L', a small perturbation of λ results in a balanced change of Φ and Ψ. This value can thus be considered as representing the 'optimum' trade-off between the best fitting solution and the most reasonable estimate for the impedance function.

Using this type of additive constraint, we need to replace the gradient in the scheme described in the previous section, in the following way:

$$g_N = -\frac{\sum_J \mathcal{K}_J^* r_{J,N} + \lambda \sigma_{N-1}}{\sum_J ||d_J^1||^2}, \tag{C.14}$$

while the step size α needs to be replaced by:

$$\alpha_N = \frac{\sum_J \langle r_{J,N-1}, \mathcal{K}_J \gamma_N \rangle}{\sum_J ||\mathcal{K}_J \gamma_N||^2 + \lambda ||\gamma_N||^2}. \tag{C.15}$$

Apart from these adjustments, the conjugate-gradient scheme remains the same.

D

Computational aspects

To set up the conjugate-gradient scheme we first write our scattering equation (Equation (2.27)) in operator form. We meet the operator defined in this way several times: in the direct calculation of the scattered field and in the inversion, and once in the form of the adjoint in the inversion. Because calculation of the action of those operators represent the main computational effort in our scheme, we want to do it efficiently. This is most easily done with the use of the convolution theorem.

In each of these spatial convolutions, the Green's function occurs. To avoid computing the spatial Fourier Transform of the Green's function (Eq. 2.22), we derive its representation in the wavenumber-frequency domain in the second section of this appendix.

D.1 Operators

In operator form, our near-receiver scattering equation can be written as (Equation (2.27) and (2.31)):

$$\left\{d^{1,op}, v^{1,op}\right\} = \mathcal{K}_J^{d,v}\sigma, \tag{D.1}$$

where $\mathcal{K}^{d,v}$ is the operator defined through:

$$\left\{\mathcal{K}^{d,v}\sigma\right\}(\mathbf{x}_L, 0) = \int_\Sigma u^G(\mathbf{x}_L - \mathbf{x}'_L, z^{(0)})\sigma(\mathbf{x}'_L, z^{(0)})\left\{d^{meas}, v^{meas}\right\}(\mathbf{x}'_L, 0)\mathrm{d}A \tag{D.2}$$

For the gradient in the conjugate-gradient scheme we need an expression for the adjoint operator as defined through Equation (C.9). Explicitly, we found for the adjoint operator (Equation C.10):

$$\{\mathcal{K}^* r\}(\mathbf{x}'_L, z^{(0)}) = \bar{d}^{meas}(\mathbf{x}'_L, 0)\int_\Sigma \bar{u}^G(\mathbf{x}'_L - \mathbf{x}_L, z^{(0)})r(\mathbf{x}_L, 0)\mathrm{d}^2\mathbf{x}_L, \tag{D.3}$$

where the $*$ denotes the adjoint, the overbar denotes complex conjugate and r is the residual as defined in Appendix C, Equation (C.1). In both operators we recognize a spatial convolution, as defined in Appendix A, Eq. (A.7). If we define the quantity w, through:

$$w^{d,v}(\mathbf{x}'_L, z^{(0)}) = \sigma(\mathbf{x}'_L, z^{(0)})\left\{d^{meas}, v^{meas}\right\}(\mathbf{x}'_L, 0), \tag{D.4}$$

then we can write Equation (D.2) as

$$\left\{\mathcal{K}^{d,v}\sigma\right\}(\mathbf{x}_L, 0) = \int_\Sigma u^G(\mathbf{x}_L - \mathbf{x}'_L, z^{(0)})w^{d,v}(\mathbf{x}'_L, z^{(0)})\mathrm{d}A \tag{D.5}$$

Consequently, we can use the spatial convolution theorem Eq. (A.8) to efficiently calculate these equations.

On account of this theorem, we can write:

$$\left\{\mathcal{K}^{d,v}\sigma\right\}(\mathbf{k}_L, 0) = u^G(\mathbf{k}_L, z^{(0)})w^{d,v}(\mathbf{k}_L, z^{(0)}). \tag{D.6}$$

The result in the space-frequency domain is now obtained by applying the two-dimensional inverse Fourier transformation to the result of Equation (D.6):

$$\left\{\mathcal{K}^{d,v}\sigma\right\}(\mathbf{x}_L, 0) = \mathcal{F}_L^{-1}\left\{u^G(\mathbf{k}_L, z^{(0)})w^{d,v}(\mathbf{k}_L, z^{(0)})\right\}, \tag{D.7}$$

where $\mathcal{F}_L^{-1}\{f(\mathbf{k}_L)\}$ is shorthand notation for the inverse Fourier transform defined by Eq. (A.4).

In the next section, we derive an explicit expression for the Green's function Eq. (2.22) in the wavenumber-frequency domain. Using this expression, we can express the calculation of the scattered field as:

$$\left\{d^{1,op}, v^{1,op}\right\}(\mathbf{x}_L, 0, \omega) = \mathcal{F}_L^{-1}\left\{u^G(\mathbf{k}_L, z^{(0)}, \omega)\mathcal{F}_L\left\{\sigma(\mathbf{x}_L, z^{(0)}, \omega)\left\{d^{meas}, v^{meas}\right\}(\mathbf{x}_L, 0, \omega)\right\}\right\}. \tag{D.8}$$

Here $\mathcal{F}_L\{f(\mathbf{x}_L)\}$ denotes the forward Fourier transform defined in Eq. (A.3).

In the same way, we can express the calculation of Equation (D.3) as:

$$\{\mathcal{K}^* r\}(\mathbf{x}'_L, z^{(0)}, \omega) = \bar{d}^{meas}(\mathbf{x}_L, 0, \omega)\mathcal{F}_L^{-1}\left\{\bar{u}^G(\mathbf{k}_L, \omega)\mathcal{F}_L\{r(\mathbf{x}_L, 0, \omega)\}\right\}. \tag{D.9}$$

In the numerical implementation these expressions are discretized and we use the Fast Fourier Transform to compute the discretized Fourier Transform (see e.g. Brigham, 1988).

D.2 Green's Function in the Wavenumber-Frequency Domain.

The Green's function of our problem is defined as the solution to (Equation (2.21)):

$$\left[\partial_k\partial_k + \frac{\omega^2}{c_S^2}\right] u^G(\mathbf{x}_L - \mathbf{x}'_L, \zeta, \zeta') = -\frac{c_S}{c_P}\delta(\mathbf{x}_L - \mathbf{x}'_L, \zeta - \zeta') \tag{D.10}$$

This equation is complemented with the boundary condition of a traction free surface at $z = 0$ (Equation 2.6): $n_j\tau_{ij} = 0$. The relevant component can be found using the generalized Hooke's law (Equation (2.15)):

$$\tau_{33} = (\lambda + 2\mu)\partial_3 u_3, \tag{D.11}$$

and the boundary condition can be written as:

$$\lim_{z\downarrow 0} \partial_3 u_3 = 0. \tag{D.12}$$

In addition, the displacement satisfies the radiation condition, to allow only outgoing waves at infinity.

This problem can be solved by the method of images (e.g. Morse and Feshbach, 1953, p. 848). However, to efficiently calculate the spatial convolutions as described in the previous section, we choose to express this Green's function in the wavenumber-frequency domain.

To solve for u^G we transform Equation (D.10) to the spatial-wavenumber domain using Equation (A.3):

$$\left(\partial_3\partial_3 + k_3^2\right) u^G(\mathbf{k}_L, \zeta, \zeta') = -\frac{c_S}{c_P}\delta(\zeta - \zeta')\exp(\mathrm{i}k_\alpha x'_\alpha). \tag{D.13}$$

Here the vertical wavenumber $k_3^2 = \frac{\omega^2}{c_S^2} - k_\alpha k_\alpha$ and $\mathbf{k}_L = (k_x, k_y)$.

The δ-distribution is accounted for by a jump condition at the source depth:

$$\lim_{\zeta\uparrow\zeta'}\partial_3 u_3 - \lim_{\zeta\downarrow\zeta'}\partial_3 u_3 = -\exp\left(\mathrm{i}k_\alpha x'_\alpha\right). \tag{D.14}$$

At the source depth, we also have a continuity condition for the field u_3:

$$\lim_{\zeta\uparrow\zeta'} u_3 - \lim_{\zeta\downarrow\zeta'} u_3 = 0. \tag{D.15}$$

Now we use the trial solutions:

$$\phi(\zeta, \zeta') = A\exp\left(\mathrm{i}k_3(\zeta - \zeta')\right) + B\exp\left(-\mathrm{i}k_3(\zeta - \zeta')\right), \qquad \zeta < \zeta', \tag{D.16}$$

and

$$\psi(\zeta, \zeta') = C\exp\left(\mathrm{i}k_3(\zeta - \zeta')\right) + D\exp\left(-\mathrm{i}k_3(\zeta - \zeta')\right), \qquad \zeta > \zeta'. \tag{D.17}$$

Solving for A, B, C and D and rearranging yields the Green's function:

$$u^G(\mathbf{k}_L, \zeta, \zeta') = \frac{c_S}{2\mathrm{i}k_3 c_P}\left(\exp\left(-\mathrm{i}k_3|\zeta - \zeta'|\right) + \exp\left(-\mathrm{i}k_3|\zeta + \zeta'|\right)\right)\exp\left(\mathrm{i}k_\alpha x'_\alpha\right), \tag{D.18}$$

where $\mathbf{Re}\ k_3 > 0$ and $\mathbf{Im}\ k_3 < 0$, on account of the radiation condition (Bleistein et al., 2001, p. 31) and our Fourier transformation conventions. In order not to complicate the main text, we will use z instead of ζ to denote the scaled depth from Equation (2.22) on.

E

Filtering

In the first step of our method as described in Section 2.3, we select a reference event from a shot record. However, the inversion scheme requires scattered data as input. To this aim, we separate the scattered field from this reference wave field in the second step. This separation is done with the use of a suitable filter.

Because the scattered field interferes with the incoming wave itself, this requires careful processing. In this appendix we describe two ways of wave-field separation, each for a different situation. However, there exist many other methods to achieve similar results and for yet other situations.

E.1 Wavenumber-Frequency Domain Filtering

We transform the recorded data to the spatial-wavenumber frequency domain using the Fourier transformations defined in Appendix A, Eqs. (A.1) and (A.3), yielding

$$d(\mathbf{k}_L, 0, \omega) = \int_{-\infty}^{\infty}\int_{-\infty}^{\infty}\int_{-\infty}^{\infty} w(\mathbf{x}_L) d(\mathbf{x}_L, 0, t) \exp[\mathrm{i}(k_\alpha x_\alpha - \omega t)] \mathrm{d}^2\mathbf{x}_L \mathrm{d}t, \tag{E.1}$$

where $w(\mathbf{x}_L)$ is a window function with tapered edges, to suppress edge effects.

In the wavenumber frequency domain we select the plane event, with a filter function: let $f(\mathbf{k}_L, \omega)$ be the filter function and d^0 the filter output. The output can be obtained by taking the inverse transform of the product of the filter function and the data:

$$d^0(\mathbf{x}_L, 0, t) = \int_{-\infty}^{\infty}\int_{-\infty}^{\infty}\int_{-\infty}^{\infty} v(\mathbf{k}_L) f(\mathbf{k}_L, \omega) d(\mathbf{k}_L, 0, \omega) \exp[-\mathrm{i}(k_\alpha x_\alpha - \omega t)] \mathrm{d}^2\mathbf{k}_L \mathrm{d}\omega, \tag{E.2}$$

where $v(\mathbf{k}_L)$ is another window function to suppress edge effects. The filter function $f(\mathbf{k}_L, \omega)$ can be compared to the one-pass 3D wavenumber-frequency domain filters described by Rowbotham and Goulty (1990) or Stewart and Schieck (1989). The filter function passes a small area around the expected wavenumbers (k_x, k_y) at a given frequency for a plane wave.

Now the scattered field is obtained by subtracting this output from the total field in the space-time domain in the following way:

$$d(\underline{\mathbf{x}}_L, t) - \beta d^0(\underline{\mathbf{x}}_L, t) = d^1(\underline{\mathbf{x}}_L, t). \tag{E.3}$$

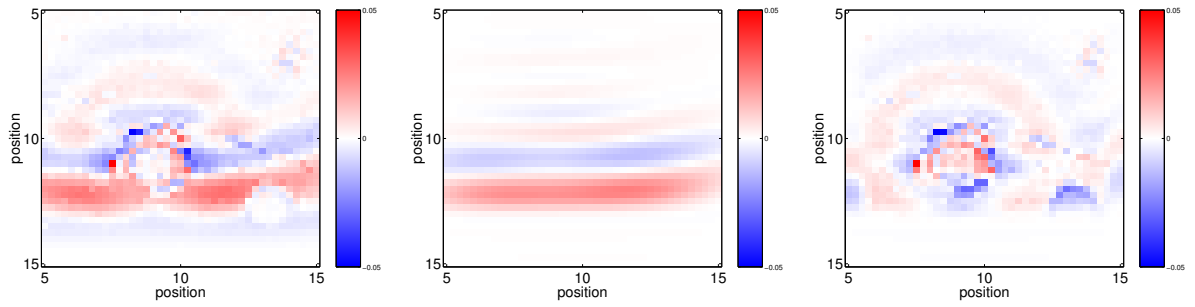

(a) (b) (c)

Figure E.1: *Wave-field separation in the space-time domain. In the displays, time is constant. (a) Time slice of a event passing through a cavity in the surface of an aluminum block. Note the scattering slightly to the left and down from the center of the picture. (b) Time slice (same time) of the estimated incident field from the filter described above. (c) Time slice of the scattered field obtained as the difference between (a) and (b). The factor β in Equation (E.3) is $\beta = 1.12$. The Figures have been displayed in the same scale.*

The factor β is included here to account for energy loss due to the various window functions. This factor should be chosen such that the incident field is optimally removed from the event, as is shown in a time slice in Figure E.1(a)-E.1(c). This figure illustrates wave-field separation in the space time domain. In the left panel, the total field is depicted, while in the middle panel we show the estimated incident field using the procedure described above. Since we used a very narrow filter in the wavenumber domain, we can still observe edge effects in this display. In the right panel, the difference between the total field and the estimated incident field is shown. In this case, $\beta = 1.12$ gave the best result. This figure confirms that we have removed most of the coherent energy and we have thus separated the scattered energy.

E.2 Alpha-Trimmed Mean Filtering

The wavenumber-frequency domain filter is relatively easy to implement and fast, but it is limited to cases where it is known that the embedding is laterally homogeneous. Moreover, it is most practical if the incident wave is (nearly) a plane wave.

If the shallow subsurface varies slowly with respect to the dominant wavelength, we want to retain that variation, because our method is primarily aimed at correcting for rapid variations due to local heterogeneity or rapid changes in topography. Thus, we want to smooth the event, without destroying the slow trend. In principle, we could use a mean filter for this purpose. However, it is well known that the mean filter is not robust. For example, the mean depends

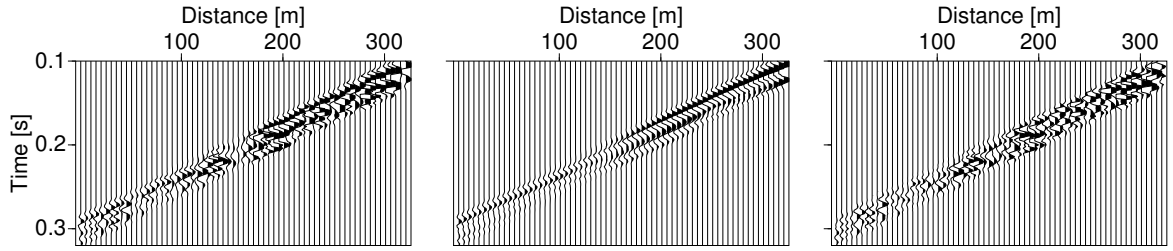

Figure E.2: *(a) A reference event with considerable long spatial wavelength and rapid variations. (b) Estimate of the incident wave field. This estimate is obtained using the α-TM filter. The long spatial wavelength variation has been preserved in the incident field. (c) Estimated near-surface scattered energy. This is the wave field attributed to the presence of local heterogeneity. From this figure we conclude that we have chosen the parameters correctly. The diffraction hyperbola around 130 m has been left unaffected while most of the aligned direct wave has been removed.*

on 'outliers', smearing them in the output. Because seismic data often contain anomalous or zero traces, these will be taken into account in the mean. A filter that is robust in the presence of outliers is the median filter. However, this filter is known to preserve edges (sharp changes) in the data, while it is usually these changes that we want to smooth. In post-stack data these changes can indicate faults or other geological features and one may want to preserve these steps, but in our application we attribute any sharp changes to scattering.

For this reason, we use the α-trimmed mean (α-TM) filter (Bednar and Watt, 1984). The α-TM combines properties from the mean and median filters. Given a set of time samples $\{x_i\}_{i=1}^{N}$, the α-TM is defined by (for N=odd):

$$\chi = \frac{1}{N - 2\alpha N} \sum_{i=\alpha N+1}^{N-\alpha N} x_{(i)}, \tag{E.4}$$

where χ is the output sample and $x_{(i)}$ are the samples from the sorted set $\left\{x_{(i)}\right\}_{i=1}^{N}$.

Thus, the output of the α-TM filter is obtained by taking the mean of the data within a certain window of length N ordered in ascending order and after dropping a number of points on each end of the ordered array. The fraction of the data that is dropped is relative to the window and is controlled by α, with $0 \leq \alpha \leq .5$. If $\alpha = 0$, the α-TM is the mean filter, while if $\alpha = .5$ it is a median filter. In this way, the window length and the parameter α offer a handle on the spatial wavelength of the variations allowed in the estimate of the incident wave field.

The main reason to use this filter is because we want a robust way to smooth the event. In practice, we take α small so that the filter most resembles the mean filter, but it is not sensitive to outliers. The window length determines the smoothness of the event. Figure E.2 shows the

result of filtering an event with both long and short spatial wavelength variations. To obtain this result we have first applied linear move-out to the event.

In case of surface topography we use the α-TM filter as well, but after aligning the first arrival times of the traces (first breaks). In this way, we preserve the topography trend in the incident wave field while scattering due to topography is isolated (see Section 4.2.3).

Samenvatting

‘Afbeelden en Verwijderen van Verstrooide Seismische Golven Dichtbij de Ontvangers’

Xander Campman

Vanwege de verwachte sterk stijgende vraag naar olie in de komende decennia, investeren olie maatschappijen om nieuwe oliereserves te vinden en produceren. In de meeste gevallen maken ze gebruik van seismische exploratie methoden om olie op te sporen. Het belangrijkste doel van deze methoden is om een gedetailleerd beeld van de diepe ondrgrond te krijgen. Om aan de vraag voor nieuwe reserves te kunnen blijven voldoen, zoeken olie maatschappijen in steeds complexere gebieden. Een mogelijke consequentie daarvan is slechtere kwaliteit van de data, veroorzaakt door de vaak sterk heterogene ondiepe ondegrond.

Seismische golven die door lagen diep in de ondergrond zijn gereflecteerd, kunnen worden verstoord als ze door de ondiepe ondergrond lopen. Als de heterogeniteit van de ondiepe ondergrond snel varieert dan veroorzaken deze snelle variaties verstrooide oppervlakte golven als naar boven lopende golven erop invallen. Die oppervlakte golven veroorzaken op hun beurt interferentie met de reflecties uit de diepe ondergrond. Tot nu toe worden variaties in de opkomende golffronten met behulp van ‘surface-consistent near-surface’ correctie methoden gecorrigeerd. Deze methoden zijn evenwel gebaseerd op een relatief simpel model van de ondergrond dat sterke limiteringen heeft. In dit proefscrhift hebben we een methode ontwikkeld om oppervlakte golven die dicht bij het oppervlakte van de Aarde verstrooid zijn te voorspellen en vervolgens van de data af te trekken zodat de continuiteit van de reflecties verbetert. Onze methode is gebaseerd op een integraal representatie van het verstrooide veld in de buurt van de ontvangers. De methode is dus gebaseerd op golftheorie en houdt rekening met conversies van opkomende golven naar oppervlakte golven.

Het principe van de methode berust erop dat we als we de distributie van heterogeniteiten in de ondiepe ondergrond en de snelheid van de oppervlakte golf in de ondiepe ondergrond kennen, we deze golven kunnen voorspellen en vervolgens van de data kunnen aftrekken. Voordat we de oppervlakte golven kunnen voorspellen hebben we echter een schatting van de verdeling van verstrooiers nodig. Dit inversie probleem lossen we op door de verdeling van verstrooiers iteratief aan te passen totdat ons voorspelde veld op een bepaalde manier goed ‘lijkt’ op het gemeten veld. Om de verstooiingsfunctie te schatten gebruiken we smalle tijd-‘windows’ om een onhafhankelijke schatting te krijgen. Dit is een overeenkomst met ‘statics’ methoden, maar onze aanpak verschilt van ‘statics’ methoden omdat wij in plaats van een enkel-kanaals correctie, een meer-kanaals filter schatten dat zowel variaties in aankomsttijden in de golffronten als fase en amplitude verstoringen corrigeert.

Met gebruik van de impedantie functie die we hebben geschat van een bepaalde reflectie, voorspellen we het verstrooide veld op de complete data set. De ‘target’ reflecties kunnen

een andere hoek van inval hebben dan de referentie reflectie. Als de verstrooiers zich minder diep bevinden dan ongeveer één Rayleigh golflengte, dan kan deze hoek oplopen tot ongeveer 30 graden. Als de verstrooiers zich dieper bevinden, dan is de hoek beperkt tot ongeveer 10 graden. Met behulp van een standaard maat voor de continuiteit van een meer-kanaals signaal, laten we zien dat onze methode de continuiteit van opkomende reflecties sterk verbetert. We hebben onze methode verder getest door hem succesvol toe te passen op data verkregen van metingen aan twee laboratorium modellen. Deze tests kunnen gezien worden als een tussenstap voordat we het algorithme toepassen op veld data. In het bijzonder blijkt dat de inversie van het verstrooide veld fysisch zinnige afbeeldingen van de verstrooier aan het oppervlak van een aluminium blok oplevert.

Met behulp van twee velddata voorbeelden laten we zien dat ons algorithme werkt ondanks de aanwezigheid van ruis. We verkrijgen goede resultaten voor data die opgenomen zijn in een gebied met een sterk heterogene ondiepe ondergrond en een gebied met topografische verschillen. We laten verder zien dat we een meer-kanaals filter verkrijgen dat consistent is met data van verschillende schoten. In onze formulering wordt de ondiepe ondergrond gekarakteriseerd door middel van de snelheid van de Rayleigh golf. Een gevoeligheidstest voor deze parameter leverde op dat de methode niet erg gevoelig is voor de Rayleigh-golfsnelheid. In de velddata kiezen we de fundamentele Rayleigh-golfsnelheid die we uit de data schatten. Voor onze methode is dus geen gedetailleerde informatie van de ondiepe ondergrond nodig.

Summary

Imaging and Suppressing Near-Receiver Scattered Seismic Waves

Xander Campman

Because of the expected steep rise in oil demand in the next decades, oil companies make investments to explore and produce new reserves. In most cases one uses seismic exploration methods to prospect for oil. The main aim of seismic exploration is to obtain detailed images of the subsurface. To meet the demand for future reserves, oil companies explore in areas with progressively complex near-surface regions. One of the consequences of exploration in such areas is poorer data quality, compromising the quality of final images.

Body waves that have been reflected by deep layers can be distorted when they travel through the near subsurface. When the near-surface region varies rapidly, upcoming body waves excite scattered surface waves, which interfere with the reflections of interest. Up to now, surface-consistent near-surface correction methods correct for rapid variations in arrival times of a reflector, but these techniques are based on a model that assigns the same uniform time shift to each trace from a distinct surface location, assuming vertical ray paths through the overburden. These single-channel methods impose strong restriction on the near-surface model. In this thesis we have developed a multichannel method to predict and suppress near-receiver scattered waves, thereby restoring the continuity of upcoming reflections. The method is based on an integral representation for the scattered field in the vicinity of the receiver. This model is based on wave theory and takes into account body-to-surface wave scattering at the near-surface anomalies.

The main idea of our method is that with knowledge of the near-surface scattering distribution and the propagation characteristics of the near-surface region, we can predict and subsequently subtract the scattered noise. Before we can predict the scattered wave field using our scattered noise model, we need an estimate of the distribution of scatterers that excites this (secondary) wave field. This is an inverse problem, which we solve by iteratively updating a near-surface scattering function that 'best' fits the data using our scattered noise model. To derive the near-surface scattering function from the data, we use short time windows to obtain an independent estimate of the scattering distribution. This is similar to the approach taken in residual statics estimation, where one places a time window around one or a few strong reflectors to derive the time shifts that are subsequently applied to the entire data set. Our approach differs from statics, because in our formulation, single-channel time shifts or filters are replaced by a multichannel filter that takes into account both the time shift in the wavefront and additional phase and amplitude anomalies incurred by near-receiver scattering.

Using the impedance function derived from an independent event, we predict the scattered field on the entire record. Target events can have different angles of incidence than the reference

event. We use synthetic data to test the limitations of our method with respect to the incident angle of reflection events and the mean scattering depth. For differences in the angle of incidence of the reference event and the target event up to about 30 degrees, our method works well for a mean scattering depth that is less than a Rayleigh wavelength. When the scattering takes place deeper, the difference in angle of incidence should be smaller than about 10 degrees. Using a measure for trace-to-trace continuity of multichannel records, we found that application of our method greatly increases the continuity of events that had been scattered by near-receiver heterogeneities. We have further validated our method with data from two laboratory models. These tests can be seen as an intermediate step towards the implementation of our algorithm for field data. Our algorithm performed well on the laboratory data. In particular, we have found that the inversion step gives physically meaningful images of the near-surface region of the laboratory model.

In two field data examples we show that our method is robust in the presence of noise and we obtain good results in the presence of a near-surface layer containing boulders and another one with surface topography. We show that we obtain a multichannel filter that is consistent with data from a few shots. This filter represents the impedance experienced by upcoming reflection events when traveling trough the subsurface. In our formulation, the near-surface is characterized by the fundamental Rayleigh-wave velocity. From a sensitivity test we have found that our method is not very sensitive to this velocity. In the field data, we choose the fundamental Rayleigh-wave velocity, which we estimate from the data. Thus, the method does not require detailed information about the near-subsurface.

Dankwoord

In eerste instantie dank ik mijn promotor, Prof Aad Hermans, voor z'n betrokkenheid bij dit onderzoek en de tijd die hij heeft genomen voor discussies, bijvoorbeeld over die ene formule die dit proefschrift rijk is.

Mijn meeste dank gaat evenwel uit naar Gérard Herman die als co-promotor het meest bij dit werk betrokken is geweest. Door zijn laagdrempeligheid (dat is vriendelijk bedoeld) stond de deur altijd open voor discussies over zowel dit onderzoek als over minder wetenschappelijke onderwerpen. Zijn reislust deelt Gérard met z'n studenten zodat we veel kans hebben gehad om op pad te gaan met ons werk. Dat heeft in zeer sterke mate bijgedragen aan het plezier dat ik heb gehad tijdens m'n onderzoek.

Ik dank alle leden van de STW commissie (Guy Drijkoningen, Jan Brouwer, Colin Perkins en Everhard Muyzert) voor hun interesse en opbouwende kritiek gedurende de loop van dit onderzoek. In het bijzonder wil ik Everhard bedanken voor de moeite die hij gedaan heeft om de data die we in Paragraaf 4.1 gebruikt hebben beschikbaarbaar te maken. Hiervoor en voor de toestemming om de resultaten hiervan te publiceren zijn we ook Schlumberger Cambridge Research/WesternGeco erg erkentelijk. Ook wil ik Colin en z'n collega Guido Baeten speciaal bedanken omdat ze de tijd hebben genomen om delen van dit proefschrift te lezen en hun commentaar met mij te bespreken.

Om meer inzicht te krijgen in het 'near-field scattering' probleem, hebben we in het begin van dit onderzoek data gesimuleerd met een elastisch Finite Difference programma van Shell in Rijswijk. We danken Shell voor het beschikbaar stellen van dit progamma en de computertijd en voor toestemming om de resultaten ervan te gebruiken. In het bijzonder dank ik Wim Mulder, voor zijn uitleg van de code en voor het op gezette tijden delen van z'n kamer.

Ik dank Dries Gisolf, Eric Verschuur en Gerrit Blacquière van het Delphi consortium voor hun betrokkenheid bij dit onderzoek en voor de kans die ze mij hebben gegeven om ons werk in hun consortium bijeenkomsten te presenteren. Dit heeft er o.m. toe geleid dat we in contact kwamen met Saudi Aramco, dat ook velddata beschikbaar hebben gesteld. Voor de moeite die ze gedaan hebben om die data hier te krijgen wil ik met name Mohammed Al-Faraj, Emad Al-Janoubi, Kamal Al-Yahya en Mustafa Al-Ali bedanken. We would like to thank Saudi Aramco for making their data available and giving permission to publish the results. Ik dank Remco Romijn (Delphi), voor zijn hulp en goede suggesties tijdens het processen van de velddata.

Many thanks to everyone in the Physical Acoustics Lab, the Center for Wave Phenomena and the Center for Rock Abuse at Colorado School of Mines. In particular I thank John Scales for inviting me to his Lab and for his enthousiastic help with collecting the data and for discussing the possibilities and our models with me. Het succes van deze samenwerking is verder in het geheel te danken aan het enthousiasme van Kasper van Wijk, waarvoor mijn grote dank. Tegelijkertijd wil ik Kasper en Mila (en Charlie en Golden) bedanken voor hun gastvrijheid. Finally, I thank Roel Snieder and Ken Larner of the Center for Wave Phenomena for their support during this collaboration and for giving me the opportunity to present the results of our

collaborative work in the Annual Review Meeting of the ‘Consortium for Imaging in Complex Media’.

Of course, I thank all my former and present colleagues at the department for Applied Analysis for the nice atmosphere at and outside University. I consider myself extremely fortunate for having had the change to work in such a diverse group. In particular, I thank Dwi — makasih ya; she has contributed to this thesis and my well-being in many (mysterious) ways.

Graag dank ik ook alle huidige en oud-collega’s in de Seismiek groep bij Natuurkunde voor de aangename verstrooiing in Delft en tijdens congressen. Maar, afgezien daarvan, hebben met name Kees, Paul en Mustafa met discussies bijgedragen aan dit onderzoek.

Verder wil ik nog Jan-Willem bedanken voor de ‘artist’s impressions’ die hij gemaakt heeft voor sommige presentatie’s, Matthijs voor het brainstormen met de stellingen en Iwan omdat ik zodoende heel ‘ITP’ heb gehad. Ik dank Mulder voor de biertjes op onze ‘square mile’ in Den Haag.

Uiteraard ben ik Joep en Sander zeer dankbaar voor hun bereidheid om als paranimfen op te treden.

Maar, uiteindelijk heb ik eigenlijk alles te danken aan Pappa en Mamma, Maarten, Pauline, Sophie en Maurits, Arnoud en Mim en Dwi.

X.C.,
Den Haag,
Januarie 2005

Levensbericht

Xander werd geboren op 21 April 1971, te Eindhoven. In 1983 ging hij in Weert naar het Bisschoppelijk College waar hij, na enige tijd het Atheneum gevolgd te hebben, in 1990 zijn HAVO diploma haalde. Vervolgens startte hij de studie 'Boortechnologie' aan de Hogeschool voor Petroleum en Gastechnologie in Den Helder, waar hij zijn propedeuse behaalde.

In 1992 begon hij de studie 'Mijnbouwkunde en Petroleumwinning' aan de TU Delft. Hier studeerde hij in 2000 af in de vakgroep Geofysica. Tijdens een stage bij Schlumberger-Doll Research in Ridgefield, CT (US), werd hij gegrepen door het Grondradar onderzoek wat leidde tot een afstudeeropdracht met die radar als onderwerp. Met Dr. Evert Slob en prof. Jacob Fokkema werkte hij aan '3D GPR data imaging'. Tijdens zijn studie heeft hij verder o.a. veel (Grondradar) veldwerk gedaan, o.m. voor TNO, GeoDelft en in opdracht van het Nederlands Forensisch Instituut. Gedurende zijn afstuderen gaf hij als inval leerkracht een half jaar lang, acht uur per week, wiskundeles aan brugklassers en 4 VWO'ers op de middelbare school Spieringshoek in Schiedam.

In 2000 begon hij aan de faculteit Toegepaste Wiskunde met Dr. Gérard Herman en prof. Aad Hermans aan zijn onderzoek op het gebied van de verstrooiing en het afbeelden van seismische (oppervlakte) golven dichtbij het oppervlak van de Aarde. Tijdens dit onderzoek heeft hij onder andere verschillende experimenten uitgevoerd in het Physical Acoustics Laboratory aan de Colorado School of Mines in Golden, Co (US), om de in dit proefschrift uitgewerkte theorie te staven.

Vanaf Maart 2005 is Xander als Post-doctoral fellow werkzaam in het Earth Resources Laboratory aan het Massachusetts Institute of Technology, Cambridge, MA (US).